Decoupled Overlapping Grids for Modelling Transient Behaviour of Oil Wells

Nneoma Ogbonna

Submitted for the degree of
Doctor of Philosophy

Heriot-Watt University
School of Mathematical and Computing Sciences
Department of Mathematics

August 2010

Abstract

This research presents a new method, the decoupled overlapping grids method, for the numerical modelling of transient pressure and rate properties of oil wells. The method is implemented in two stages: a global stage solved in the entire domain with a point or line source well approximation, and a local (post-process) stage solved in the near-well region with the well modelled explicitly and boundary data interpolated from the global stage results. We have carried out simulation studies in two- and three- dimensions to investigate the accuracy of the method.

For homogeneous case studies in 2D, we have demonstrated the convergence rate of the maximum error in the quantities of interest of the global and local stage computations by numerical and theoretical means. We also proposed a guideline for the selection of the relative mesh sizes of the local and global simulations based on error trends. Comparison to other methods in the literature showed better performance of the decoupled overlapping grids method in all cases.

We carried out further investigations for heterogeneous case studies in 2D and partially-penetrating wells in 3D which show that the error trends observed for the 2D homogeneous case deteriorate only slightly, and that a high level of accuracy is achieved. Overall the results in this thesis demonstrate the potential of the method of decoupled overlapping grids to accurately model transient wellbore properties for arbitrary well configurations and reservoir heterogeneity, and the gain in computational efficiency achieved from the method.

For Kaycee, Blues, Zeros.

Acknowledgements

I would like to express the deepest appreciation to my supervisor Professor Dugald Duncan for his guidance, encouragement and untiring support throughout my studies. I would also like to thank Dr Bernd Schroers, Dr Lyonell Boulton, Dr Lubomir Banas, and many others at the Department of Mathematics, Heriot-Watt University, who were always helpful when I showed up with the odd math question.

Finally I am indebted to my family and friends for their love and encouragement.

Table of Contents

Nomenclature

The base quantities for the units are: F = force, L = length, M = mass, T = time

Greek Letters

δ	Dirac delta function	$1/L^3$
η	diffusivity coefficient	L^2/T
μ	fluid viscosity	FT/L^2
ϕ	porosity	-

Roman Letters

c_t	total compressibility	L^2/F
H	domain height (2D simulations)	L
k	absolute permeability	L^2
p	pressure drawdown	F/L^2
q	production/injection rate	L^3/T
q_l	production/injection rate per unit well length	L^2/T

Subscripts

ana	analytic solution
bm	benchmark computed in Comsol
dg	solution from decoupled overlapping grids
fw	finite radius well
ls	line source
num	numerical solution
ps	point source

Chapter 1

Introduction

1.1 Background and motivation

This research investigates a new method, the decoupled overlapping grids method, for application to the problem of modelling the transient wellbore pressure of oil wells. The important characteristic of this problem is that dynamic information is desired at or near features which are of a significantly smaller spatial scale compared to the computational domain. We will consider this problem within the framework of well test analysis of oil and gas reservoirs, but note here that similar problems arise in groundwater flow.

The ultimate goal of reservoir simulation is to forecast well flow-rates and/or bottom-hole pressures accurately, and to estimate the pressure and saturation distributions [45]. This involves the numerical solution of a set of coupled equations for multi-phase, multi-component flow in a heterogeneous porous medium. The properties of the porous medium and the dynamic properties of the reservoir fluid can be estimated by the well testing technique.

Well test analysis is a reservoir assessment technique usually applied to reservoirs whose geology and geometry have been largely determined by other means (e.g. seismic surveys) and refines that information [40]. The process involves measuring the pressure response of a reservoir to changing production or injection rates. Since this response is more or less characteristic of the reservoir, it can be used to estimate the properties of the reservoir. By specifying the measured flow rate history as an input to a mathematical model, it is inferred that the reservoir properties predicted by the mathematical model are the same as those

of the physical reservoir if the pressure output of the model matches the measured pressure response. This parameter fitting process is typical of inverse problems and several model evaluations are required to obtain best-fit estimates.

The design and interpretation of a well test is dependent on its objectives. These objectives fall into three categories [61]: reservoir evaluation, management and description. The aim of well testing in reservoir evaluation is to determine whether the reservoir is viable for production and if so decide the best way to produce it. To this end the properties of interest include the initial pressure of the reservoir, its conductivity (permeability-thickness product), and its boundaries. In reservoir management the aim of well testing is to monitor overall reservoir performance and well condition so as to adjust forecasts of future production. Here knowledge of changes in average reservoir pressure is required. The goal of well testing in reservoir description is to characterise geological features of the reservoir that affect pressure transient behaviour to a measurable extent. In general the objectives of a well test can be summarized as follows [19]:

- To evaluate well condition and reservoir characterisation.
- To obtain reservoir parameters for reservoir description.
- To determine whether all the drilled length of the oil well is also a producing zone.
- To estimate the drilling and completion damage to an oil well, based on which a decision about well stimulation can be made.

Well tests can be carried out with a single well (single-well test) or multiple wells (multi-well tests) [96]. Single-well tests are carried out on exploration or production wells with different objectives in mind. An exploration well is typically completed in a formation whose properties are unknown prior to testing. Consequently a major objective of the well test is to determine what type of fluid the well will produce and at what rate. On the other hand a production well is a permanent completion in a formation whose properties are known within certain limits. Hence the main objective of the well test is to determine reservoir transmissibility, flowing well efficiency, and the static pressure within the well drainage area. For multi-well tests, rate measurements are made at a producing well and pressure measurements are made at surrounding shut-in observation wells. Multi-well tests are carried out to determine directional permeability or

heterogeneity trends. Further classification of well tests into build-up, drawdown, injection, fallout, interference and pulse tests is described in the literature. For more information on well test analysis standard texts can be consulted, for example [15, 19, 42, 61, 88, 96].

As stated previously well test analysis involves matching measured well rate and pressure data to predicted well rate and pressure variation from a mathematical model. Usually measured pressure data and its derivative are matched to analytical or numerical models. The pressure derivative has a set of characteristic slopes that are indicative of different flow regimes like radial flow or the effects of boundaries. The presence of these flow regimes is used to determine reservoir parameters such as permeability or reservoir size [8]. The difficulty in well modelling arises from the difference in scale between the size of the reservoir (hundreds of metres) compared to the well diameter (approximately 10 cm). Pressure gradients are largest in the region closest to the wellbore, which is typically smaller than the spatial size of grid blocks used in the numerical simulation. The steep pressure gradients near the well can be accurately captured by using local grid refinement to resolve the wellbore. However as several model evaluations are required in well test analysis for the parameter fitting process, local grid refinement increases computational cost significantly, especially for 3D field-scale models with a large number of wells. On the other hand, established well testing techniques rely heavily on analytic solutions for specialised reservoir properties and geometry. These analytic solutions are characterised by simplifying assumptions about the reservoir and therefore cannot account for the complexity of realistic reservoirs.

Overlapping grids offer an attractive alternative to local grid refinement and analytic solutions for well testing applications. With overlapping grids, one can independently fit a local mesh to the wellbore and superimpose this on a much coarser mesh generated on the entire computational domain. This offers accurate solutions in the wellbore vicinity, and local properties such as wellbore radius or local mesh size can be changed without the need to regenerate the the mesh for the entire domain.

There has been much work on the use of overlapping grids for solving steady and time-dependent problems in complex geometric configurations (see for instance [26, 27, 30, 40, 59, 60, 74, 81]). Overlapping grids offer the advantage of using grids best fitted to each sub-domain. The component grids overlap where

they meet, and grid functions defined on each sub-domain are matched by interpolation at the overlapping boundaries. The ability to use component structured grids even for very complex geometries permits accurate and efficient solution algorithms. Overlapping grid techniques were applied by Duncan and Qiu [40] to solve the pressure equation within the framework of well test analysis. They proved stability and convergence for a one-dimensional problem solved on overlapping grids, and demonstrated that convergence in two-dimensions appears to behave in a similar manner as the one-dimensional problem.

The method of decoupled overlapping grids studied in this work differs from the traditional composite overlapping grid methods described above. For those methods, the equations are solved simultaneously on a grid system consisting of distinct component meshes that overlap in some regions, with information in the overlapping regions merged via interpolation. In this work the problem is decoupled by solving in two stages on separate meshes which overlap (see schematic representation in Figure 1.1). In the first stage the problem is solved in the entire reservoir on a coarse grid, with the feature of interest, in this case a well, approximated by a simpler quantity, such as a point source in two dimensions or a line source in three dimensions. The first stage can be solved using standard reservoir simulators as this is the typical approximation used in these simulators. The second stage is a post-process stage. Here the problem is solved in a smaller region surrounding the wellbore. The boundary data for this stage is interpolated from the solution obtained in the first stage. The mesh used in the second stage can be adapted to the well geometry to improve the accuracy of the computed wellbore pressure.

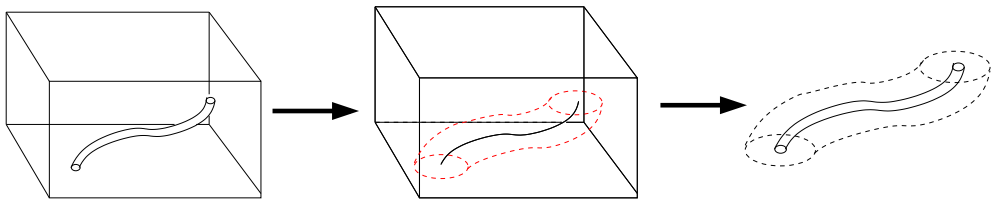

Figure 1.1: Schematic representation of decoupled overlapping grids method. L-R: Original problem. $\rightarrow$ First (global) stage; solution measured along dotted lines by interpolation. $\rightarrow$ Second (post-process/local) stage; measured data from previous stage is the boundary condition for local stage computation.

A key feature of the decoupled overlapping grids method is that the boundary condition of the post-process stage is obtained from a simulation where the well is represented by an approximate quantity (such as a line or point source). This is done based on the fact that in general the error due to this approximation decreases as distance from the well increases. Therefore by measuring the solution at a sufficient distance from the wellbore, the error in the boundary condition of the post-process stage can be kept within acceptable bounds. This modelling error is discussed in Chapter 3.

Post-processing reservoir simulation results to compute wellbore pressure is accepted practice in reservoir simulation, and is typically implemented through a well index. The seminal work by Peaceman [82, 83] introduced the widely accepted well index for computing steady-state well pressure from coarse grid simulation results. However the Peaceman well index was originally developed for fully penetrating vertical wells which are isolated, that is the wells are not close to the domain boundary or any other well, and centred in a wellblock on rectangular finite difference grids. As a result much work has been done in extending this concept to other well configurations such as slanted wells [1, 20, 21] and horizontal wells [11, 50], other grid configurations such as unstructured grids [24, 80, 105], and to compute transient wellbore pressure [9, 14]. For each of these problems an analytic solution is required to compute a well index. This presents a drawback for the well index method since analytic solutions can only be computed for simplified well and reservoir properties. In contrast the method in this thesis is much more robust. Complex reservoir features can be incorporated into the computations in a fast and efficient manner by solving the first stage in already existing reservoir simulators developed for this purpose, while locally varying well properties which are of a smaller scale than can be captured by these reservoir simulators are incorporated into the post-process stage. The method is applicable irrespective of the well location and geometry, and the mesh for the post-process stage can be adapted to the well shape for accurate and efficient computation of solutions. The method yields accurate wellbore pressure from the initial transient state through to steady-state, as the work in this thesis will show. Furthermore the method can be implemented as an add-on to already existing reservoir simulators to improve results in the near-well region.

1.2 Thesis overview

The objective of this thesis is to investigate a new method for computing transient wellbore pressure and rate for application to well test analysis. We have done this by carrying out a detailed study of the numerical and modelling errors in the method in a two-dimensional homogeneous domain, providing theoretical support for observed error trends. We have also deduced a guideline for the choice of the relative mesh sizes of the global and local stages based on error trends. Furthermore we have demonstrated the accuracy of the method for two-dimensional heterogeneous and three-dimensional case studies. Therefore this work provides fundamental insight into the accuracy and computational efficiency of the decoupled overlapping grids method for computing transient wellbore pressure and demonstrates its potential to model different types of well configurations and reservoir heterogeneity.

In Chapter 2 a detailed review of well modelling techniques in the petroleum engineering literature is presented. Models for computing both steady- and unsteady-state well pressures are discussed. This review highlights the main ideas on well modelling in the literature. We also briefly discuss the equations for single-phase flow of a slightly compressible fluid, which is the flow model implemented in this thesis.

In Chapter 3 we investigate the performance of the decoupled overlapping grids method applied to modelling a fully-penetrating vertical well in a homogeneous medium. We deduce convergence trends of the errors in the method numerically, and prove these theoretically. We also show a relationship between these errors and the relative mesh sizes of the first and second stage simulations, and based on this propose a guideline for choosing the second stage mesh size from the first stage mesh size. A comparison of the method to other methods in the literature for calculating wellbore pressure is carried out, showing in all cases better performance of the decoupled overlapping grids method.

In Chapter 4 we apply the method to compute the wellbore pressure of fully-penetrating vertical wells in heterogeneous domains. The numerical results show a high level of accuracy in the computed wellbore pressure from initial transient to steady-state, and these results are obtained for significantly less computational effort when compared to a benchmark solution. The numerical results also verify

the validity of the guideline proposed in Chapter 3 for choosing the second stage mesh size.

In Chapter 5 an application of the method to compute the average pressure of a strip/crack producing at a uniform rate is presented. This problem can be seen as a simplified model of a fractured vertical well. Numerical results show a high level of accuracy relative to benchmark solutions, achieved for significantly less computational effort.

In Chapter 6 we apply the method to compute initial-transient to steady-state pressure of partially penetrating horizontal wells. Numerical results are validated by comparison with semi-analytic solutions. An application to slanted wells is presented.

Chapter 7 contains recommendations for future studies.

Chapter 2

Literature Review

In this chapter a review of the mathematical modelling of wells in petroleum engineering literature is presented. There is a considerable amount of literature on well modelling, hence a selected sample is reviewed here to demonstrate the main ideas. The models can be grouped under the following broad categories:

- Steady- and unsteady-state well models.
- Analytic, semi-analytic and purely numerical well models.
- Vertical, horizontal and non-conventional well models.

This review is presented under the grouping of steady- and unsteady-state well models. We start the discussion by presenting the equations for single-phase flow in porous media. These equations are the subject of investigation in the majority of publications on well modelling.

2.1 Equations for single-phase flow in porous media

The equations solved in numerical reservoir simulation model multi-phase flow and transport in a heterogeneous porous medium. The equation that governs flow is of interest in well test analysis, and it is derived from conservation of mass, Darcy's law, and equations of state. Below the equation for single-phase flow is presented.

Mass conservation is described by the continuity equation:

$$\frac{\partial(\phi\rho)}{\partial t} = -\nabla \cdot (\rho \mathbf{u}) + q_m, \tag{2.1}$$

where ϕ is the porosity of the medium, ρ is the density of the fluid per unit volume, $\mathbf{u}$ is the superficial velocity[1], and q_m is the mass source term[2] which accounts for external sources or sinks. Here the density ρ and mass source term q_m are given at reservoir conditions[3]. (2.1) can also be written in terms of the formation volume factor [25]:

$$\rho = \frac{\rho_s}{B}, \tag{2.2}$$

$$\frac{\partial}{\partial t}\left(\frac{\phi}{B}\right) = -\nabla \cdot \left(\frac{\mathbf{u}}{B}\right) + \frac{q_m}{\rho_s}. \tag{2.3}$$

The formation volume factor B is defined as the ratio of volume of a fluid measured at reservoir conditions to the volume of the same fluid measured at standard conditions. ρ_s represents the fluid density at standard conditions[4].

Laminar flow through porous media is governed by Darcy's law, which gives a relationship between fluid velocity and pressure head gradient:

$$\mathbf{u} = -\frac{\mathbf{k}}{\mu}(\nabla p - \rho g H \hat{\mathbf{e}_z}), \tag{2.4}$$

where $\mathbf{k}$ is the absolute permeability tensor of the porous medium, μ is the fluid viscosity, p is pressure, g is the magnitude of gravitational acceleration and H is the depth ($\hat{\mathbf{e}_z}$ is the unit vector in the vertical downward direction). Substituting (2.4) in (2.1) yields

$$\frac{\partial(\phi\rho)}{\partial t} = \nabla \cdot \left(\frac{\rho \mathbf{k}}{\mu}(\nabla p - \rho g H \hat{\mathbf{e}_z})\right) + q_m. \tag{2.5}$$

[1] volumetric flow rate divided by cross-sectional area.
[2] mass of fluid produced/injected per unit time.
[3] temperature and pressure in the reservoir.
[4] standard reference temperature and pressure at the surface.

The equation of state is written in terms of fluid compressibility:

$$c_F = -\frac{1}{V}\frac{\partial V}{\partial p}\bigg|_T = \frac{1}{\rho}\frac{\partial \rho}{\partial p}\bigg|_T, \tag{2.6}$$

and describes the fractional change in the volume of reservoir fluid resulting from a unit pressure change at fixed temperature T. Here V represents the volume occupied by the fluid at reservoir conditions. In addition, rock compressibility is defined as the fractional change in bulk volume of the reservoir per unit pressure change:

$$c_R = \frac{1}{\phi}\frac{\partial \phi}{\partial p}\bigg|_T. \tag{2.7}$$

Under conditions of slightly compressible fluid and rock (that is, the compressibility assumed constant over certain range of pressures) substituting (2.6) and (2.7) into (2.5) gives

$$\phi \rho c_t \frac{\partial p}{\partial t} = \nabla \cdot \left(\frac{\rho \mathbf{k}}{\mu}(\nabla p - \rho g H \hat{\mathbf{e}_z}) \right) + q_m, \tag{2.8}$$

where $c_t = c_F + c_R$ is the total compressibility. This parabolic pressure equation appears in most well modelling studies in the literature.

A similar set of equations can be written for multi-phase flow, where the saturation and relative permeability of each phase must be taken into consideration.

2.2 Steady-state well modelling

Reservoir simulators are typically used to compute long term well productivity under pseudo-steady state conditions. Hence many well models targeted at reservoir simulators focus on steady-state behaviour. Pseudo-steady state behaviour is observed after the pressure disturbance created by a producing (or injecting) well has been felt at the boundaries of the reservoir. At this point the pressure throughout the reservoir changes at the same constant rate.

In this section steady-state well models on rectangular grids and flexible grids, and near-well flow models for steady-state flow, are discussed.

2.2.1 Rectangular finite difference grids

Cartesian grids are often used in reservoir simulation together with finite difference or finite volume discretisation methods. A well index is typically used on these grids to approximate the wellbore pressure from the pressure of the grid block containing the well. The conventional well index model implicitly assumes that the well coincides with the computation node, and so must be modified for other well configurations such as off-centre vertical wells and slanted wells. The conventional well index, and modelling techniques for off-centre and slanted wells, are discussed below.

Conventional well index

The well index relates well pressure and flow rate to reservoir grid block quantities. Grid blocks used in reservoir simulation are typically several orders of magnitude larger than the well diameter. As a result wells are seldom modelled explicitly; instead the well contribution is introduced as a source or sink term for the host grid block. However due to steep pressure gradients in the well vicinity, the wellbore pressure differs significantly from the pressure of the grid block it intersects (well block), and the relationship between these two quantities is expressed using a well index, defined as follows for single-phase flow:

$$q_{w,i} = \frac{\mathrm{WI}_i}{\mu_i}(p_i - p_{w,i}). \tag{2.9}$$

Here $q_{w,i}$ and $p_{w,i}$ are the well flow rate and wellbore pressure in well block i respectively, p_i and μ_i are the local well block pressure and fluid viscosity, and WI_i is the well index.

One of the earliest models for the well index is by van Poollen et al. [101], where the numerically computed well block pressure on a finite difference grid is equated to the average pressure in a circle of area equal to the well block. However the well index model proposed by Peaceman [82, 83] is the widely accepted industry standard. Here, under steady-state conditions, the well block pressure calculated using the finite difference discretisation method is assumed to be equal to the steady-state flowing pressure measured at an equivalent radius r_{eq} related to grid dimensions. For square grid blocks with the computation nodes located at the centre of each grid block, Peaceman [82] showed that $r_{\mathrm{eq}} \approx 0.2\Delta x$ using three

methods:

1. Numerically solving the steady-state pressure equation in a repeated five-spot pattern and extrapolating the plot of $p_i - p_0$ against radius r to $p_i - p_0 = 0$. Here p_i = pressure in grid block i, p_0 = well block pressure, and $r = \sqrt{(x_i - x_0)^2 + (y_i - y_0)^2}$.

2. Combining the finite difference discretisation for the well block and symmetry assumption for the adjacent blocks with the assumption that the pressure in these adjacent blocks exactly satisfy the solution for steady-state radial flow to analytically derive the equivalent radius.

3. Comparing the analytic solution by Muskat [72] for the pressure drop between production and injection wells in a repeated five-spot problem with the numerical solution on a finite difference grid.

So from the analytic solution for pressure in the well block at steady-state (under homogeneous conditions):

$$p_0 = p_w + \frac{q\mu}{2\pi kH} \ln \frac{r_{\text{eq}}}{r_w}, \tag{2.10}$$

the well index takes the form:

$$\text{WI} = \frac{2\pi kh}{\ln \dfrac{r_{\text{eq}}}{r_w}}, \tag{2.11}$$

where h is the grid block thickness and r_w is the well radius.

Peaceman [83] also extended the definition of the equivalent radius to non-square grid blocks and anisotropic permeability:

$$r_{\text{eq}} = 0.28 \frac{\left[\left(\frac{k_y}{k_x} \right)^{\frac{1}{2}} \Delta x^2 + \left(\frac{k_x}{k_y} \right)^{\frac{1}{2}} \Delta y^2 \right]^{\frac{1}{2}}}{\left(\frac{k_y}{k_x} \right)^{\frac{1}{4}} + \left(\frac{k_x}{k_y} \right)^{\frac{1}{4}}}, \tag{2.12}$$

where the well index now takes the form:

$$\mathrm{WI} = \frac{2\pi H\sqrt{k_x k_y}}{\ln \dfrac{r_{\mathrm{eq}}}{r_w}}. \tag{2.13}$$

In (2.12) and (2.13) k_x and k_y are the permeability components in the x and y directions. The well index and equivalent radius definitions given above are appropriate for a homogeneous reservoir with an isolated vertical well fully penetrating and centred in the well block. A well was assumed to be isolated if it was at least 5 grid blocks away from the boundary and 10 grid blocks away from any other well block. Furthermore the grid was assumed to be uniform in x and y.

Peaceman [84] classifies methods for computing the equivalent radius under the analytical and the numerical approach. In the analytical approach nodes surrounding the well block are assumed to satisfy the exact solution for steady-state radial flow:

$$p - p_w = \frac{q\mu}{2\pi\rho k H} \ln \frac{r}{r_w}, \tag{2.14}$$

and the pressure at these nodes are substituted into the finite difference equation for the well block to determine the equivalent radius. Peaceman warned against using the analytical approach having shown that the radial flow assumption in blocks adjacent to the well block is only valid within the aspect ratio $0.5 < \Delta y/\Delta x < 2$ for finite difference discretisation. In the numerical approach, a numerical solution is obtained for a problem with known analytic solution, and these two solutions are compared to compute the equivalent well radius.

Off-centre wells

The conventional well index discussed above was derived within the framework of the cell-centred finite difference method which implicitly assumes that the well is at the centre of the well block, and so does not correctly account for off-centre wells. Abou-Kassem and Aziz [2] developed analytic equivalent radius formulae for centred and non-centred wells within the aspect ratio $0.5 < \Delta y/\Delta x < 2$ using the analytic approach. However Peaceman [84] argued that the analytic approach for off-centre wells gave erroneous results. He proposed equivalent radius formulae for off-centre and multiple wells within an isolated well block based on the

numerical approach using the analytic solution by Muskat [72] for multiple wells in a closed reservoir. He concluded that the equivalent well block radius was independent of the location of the well within the well block. The drawback of this model is that the block pressures are assumed to be insensitive to the well position. Su [97] accounted for the effect for off-centre wells on grid block pressures by resolving well production to the four neighbouring blocks. In this formulation there is no need for a well index. He showed that for an isolated well this method gave similar results for wellbore pressure but better predicted the well block pressure when compared to the conventional well index. Ding et al. [37] on the other hand implemented modified transmissibility factors that take into consideration the angle formed by the well block faces with the off-centre well. This method has the advantage of easy application to conventional reservoir simulators.

Examples of the equivalent radius concept adapted to horizontal wells can be be seen in the work of Babu and co-workers [11, 12] and Goode and Kuchuk [50]. Babu and Odeh [11] derived an analytic wellbore pressure relation for a partially penetrating horizontal well in a box-shaped reservoir at pseudo-steady state, based on assumptions of uniform flux along the well length and the well positioned parallel to a box face. A simplified formula was given for the equivalent radius in the case of wells at the centre of the drainage area. Babu et al. [12] also derived equivalent radius formulae valid for horizontal and vertical wells at any location, for simulations on uniform grids in a rectangular homogeneous reservoir. The equations were derived by combining an exact closed-form analytic solution for discrete finite difference equations in the domain (which relates well block pressure to average pressure in drainage volume) with analytic formulae relating wellbore pressure with average reservoir pressure. Goode and Kuchuk [50] proposed an analytic wellbore pressure relation defined for a horizontal well anywhere in a drainage volume and of any length. An equivalent radius formula was proposed under the simplifying assumption that the well is sufficiently short (compared with the dimensions of the drainage volume) and is placed within the reservoir such that radial flow will develop before the influence of the lateral boundaries.

Slanted wells

Lee and Milliken [67] addressed well index computations for an inclined well in a layered finite difference grid using slender body theory and method of images. Using slender body theory the well was approximated by a distribution of point sources with density described by a function which depends on a slenderness ratio (ratio of well radius to its length). The steady-state potential in the vicinity of the well was then calculated by integrating this function along the wellbore surface. The method of images was used to account for layering of the domain. The analytic solution from slender body theory is compared to a numerical solution on a finite difference grid to determine the well index. A numerical correlation was applied to estimate the equivalent radius for large aspect ratios. For a two-dimensional isolated well, the authors reported good agreement of their method when compared with results using the conventional well index. In three-dimensions the analytical pressure calculated using slender body theory is used directly in a seven-point discretisation scheme.

Chen et al. [20, 21] studied partially and fully penetrating slanted wells in an infinite slab and a parallelepiped. They modelled slanted wells by applying a pseudo-skin factor. Skin factors are actually used to account for changes in the properties of the porous medium close to the wellbore, for instance due to damage during drilling or well stimulation. It is a dimensionless number and is determined by comparing actual conditions with ideal conditions. Various authors have adapted their use to model other situations. In the work by Chen et al. [20, 21] a pseudo-skin factor was applied to base solutions for vertically fully-penetrating wells to model the effect of well deviation angle and partial penetration. The pseudo-skin factors were then used in a simulator for prediction studies. The base solutions were analytic line source uniform flux and uniform pressure solutions. A similar method had also been used by Besson [13], who studied the performance of horizontal and slanted wells through the definition of a geometric pseudo-skin factor calculated by comparing horizontal and slanted well solutions from a semi-analytical simulator to analytic solutions for a vertical well in a homogeneous infinite reservoir.

Aavatsmark and Klausen [1] defined a semi-numerical technique for computing the well index of slanted wells. An analytic solution was first obtained by solving the steady-state pressure equation with a linear infinite well in an in-

finite reservoir. The numerical solution was then computed in a local domain surrounding the well using the analytic solution as the Dirichlet boundary data. Following this the well index in each grid block i that the well penetrates was calculated from (2.9) where the well block pressure is from numerical solution and the wellbore pressure and flow rate are from the analytic solution.

Jasti et al. [64] applied analytic solutions for arbitrary well configurations in three-dimensions to determine well index factors. The analytic solution was obtained by integrating the Green's function solution along the surface of the wellbore. The well pressure and flow rate in (2.9) were computed from this analytic solution. For uniform grids, the well block pressure was calculated from a closed form analytic solution of the discretised finite difference equations. For non-uniform grids, the well block pressure was calculated from numerical simulation. Their investigations showed that the method had a significant impact on simulator accuracy for three-dimensional flow cases and highly deviated wells.

The models in [1, 20, 21, 64, 67] are variations of the idea of computing the well index for complex well configurations by combining numerical simulations with known analytic solutions for the same problem or a similar problem. In [1, 20, 21] the well index is calculated directly without first computing an equivalent radius.

2.2.2 Flexible grids

Flexible grids such as triangular grids, Voronoi grids, and hybrid grids, are increasingly used in reservoir simulation. They offer the ability to model complex geological features such as wells more accurately, especially for multi-phase fluid flow. However as the grid size decreases rapidly in the near-well region, some approximation may be required to connect well pressure to the surrounding grid blocks.

Palagi and Aziz [80] studied the treatment of wells in Voronoi grids. They developed an exact well index model by comparing numerical and analytic solutions for the model problem of steady-state single-phase flow from a group of wells producing at constant rates in a closed rectangular reservoir. They also proposed a simplified model by assuming that the blocks adjacent to the well block satisfy the steady-state radial flow equation, and substituting this analytic pressure into the discretisation equations. This falls under Peaceman's analytic approach. The simplified model suffers from the limitation that it can only be

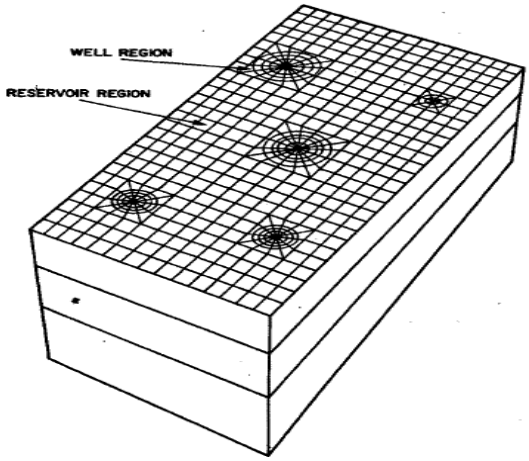

Figure 2.1: Pedrosa and Aziz [85] hybrid grid.

applied within a specific aspect ratio and only to isolated wells. On the other hand their exact well index is limited to the flow configuration (position and rate of neighbouring wells) for which it is calculated. They suggested adapting the exact model to other flow configurations by using a numerical skin factor.

Hybrid grids that combine a radial grid in the well vicinity with a different global grid, have been investigated for example by Pedrosa and Aziz [85] and Wolfsteiner and Durlofsky [105]. Pedrosa and Aziz [85] used a rectangular mesh in the reservoir region (see Figure 2.1). Special treatment was needed in the discretisation of the boundary blocks between the cylindrical and rectangular meshes. The time-dependent solutions were obtained in two stages at each time-step. Firstly the numerical solution was calculated on a rectangular grid in the entire domain using Peaceman's well index to relate well block and wellbore pressures. Then the solution was calculated on the radial grid in the well region using the solution from the first stage as boundary condition. The model was used to study two-phase flow in three dimensions. Wolfsteiner and Durlofsky [105] developed a hole-well model analogous to the conventional well index for use with multi-block grids. Multi-block grids are globally unstructured and locally structured (see Figure 2.2(a)). The local radial grid was constructed up to a concentric hole surrounding the well to avoid the excessively small grid sizes required to resolve the well boundary (see Figure 2.2(b)). Assuming steady-state radial flow, the hole-well model relates the wellbore pressure p_w to the pressure p_h at the hole boundary and the pressure p_b in the blocks surrounding the hole using

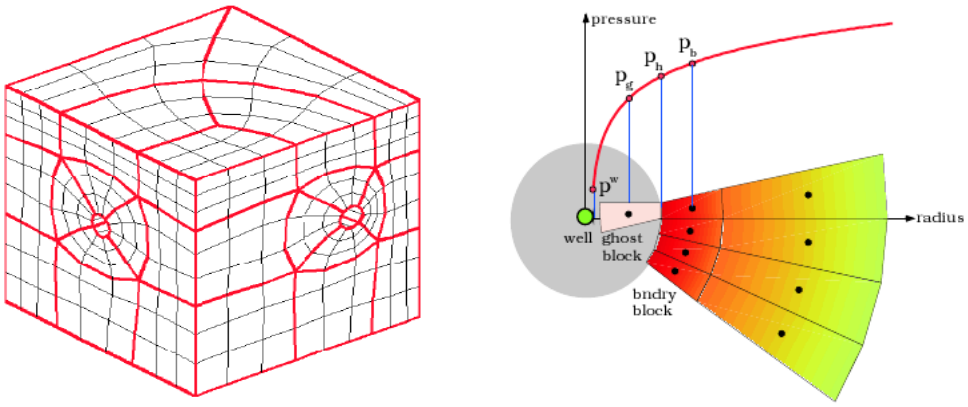

(a) Multi-block grid. **(b)** Hole well model.

Figure 2.2: Wolfsteiner and Durlofsky [105] hybrid grid

the steady-state radial flow solution in (2.14). For cases of near-well heterogeneity a local upscaling technique was applied to obtain the coarse scale transmissibility.

Chen and Zhang [24] considered well models for finite element grids. They derived specific equivalent radius formulae based on the grid mesh properties using Peaceman's analytic approach, that is, node points surrounding the wellbore satisfy the analytic radial flow equation. These formulae were derived for standard, control volume, and mixed finite element methods.

Wolfsteiner et al. [107] described a model for computing the well index of non-conventional wells (arbitrary direction and/or multiple branches) on arbitrary grids. This was done by matching the analytic reference solution for single-phase slightly compressible fluid flow calculated by integrating Green's functions along the line source well to numerical solutions for the same problem at steady-state flow. The well index for well block i was calculated from the relation in (2.9), where q_i and $p_{w,i}$ are the well flow rate and wellbore pressure from the analytic solution, and p_i is well block pressure from the numerical solution.

Ding and Jeannin [35] applied control-volume schemes to model vertical wells on triangular and Voronoi grids. They applied a change to polar-type coordinates in order to transform near-well singular flow into linear flow, thereby also transforming the original unstructured mesh to a curved mesh. The multi-point and two-point numerical schemes were then used to obtain the numerical solutions. The multi-point scheme is more accurate whereas the approximate two-point scheme is easier to implement in reservoir simulators. There was no need for a

well index in this model as the well was implemented as an internal boundary. Ding et al. [37] also applied modified transmissibility factors to improve near-well flow on flexible grids. This is discussed in more detail below.

2.2.3 Near-well flow modelling

Palagi and Aziz [80] remarked on the discrepancy between grid block pressures in the well vicinity calculated numerically on Cartesian grids and from analytic solutions due to the use of geometric grid connection factors derived from linear flow even in areas of predominantly radial flow. This problem was addressed in detail by Ding et al. [36, 37] who proposed a well model to improve flux calculation in the well vicinity using appropriate transmissibility factors. The transmissibility appears in the discretised equation and relates the flux across grid blocks to the pressure difference. It depends on permeability and grid geometry. Ding et al. [36, 37] used a logarithmic distance to compute the transmissibility factors near the well instead of the linear distance used in the rest of the reservoir (see Figure 2.3). They defined a transmissibility modification region where these new factors were applied. The conventional well index was still used to relate well block and wellbore pressure. This model was generalised to three dimensions [38], and here the near-well flux and well pressure were calculated from an analytic steady-state solution obtained using the boundary integral method. These quantities were then used to compute the transmissibility and numerical well index respectively. The method of images was applied for wells near reservoir boundaries. Ding and Jeannin [34] proposed another method for near-well flow modelling where a change of coordinates was applied to the discretised domain. This transformed Cartesian grids to curved grids, and the near-well singularity to a linear variation. Two-point and multi-point discretisation schemes were applied, and a numerical well index was used to relate well block and wellbore pressures. This model was also extended to flexible grids [35], where for example a triangular mesh defined on the original domain becomes a curved mesh in the transformed domain. Therefore there is the added complexity of discretisation on curved grids.

Several authors have also addressed near-well permeability heterogeneity through upscaling techniques. Durlofsky [41] characterised the reservoir with a single global effective permeability and defined an effective skin surrounding each well to capture local heterogeneity. The simple form of this model makes it easy

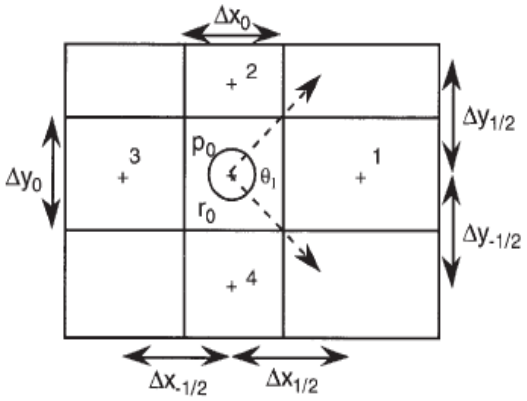

Original x-transmissibilities: $T_x = kh\dfrac{\Delta y_0}{\Delta x_{\pm\frac{1}{2}}}$

Modified x-transmissibilities: $T_x = kh\dfrac{\Delta y_0}{L_{eq,x}}$

where $L_{eq,x} = \Delta y_0 \dfrac{\ln\left(\dfrac{\Delta x_{\pm\frac{1}{2}}}{r_0}\right)}{\theta_{[1,3]}}$.

Figure 2.3: Transmissibility modification [36, 37].

to use in conjunction with existing analytic or numerical flow solutions. Chen and Wu [22] proposed a flow-based upscaling technique and an approximate well model based on arithmetic averaging for computing an upscaled well index that captured the effects of fine-scale heterogeneity in near-well regions. Ding [32] calculated equivalent transmissibilities and numerical well index of coarse well blocks using fine grid simulation results in the vicinity of the well. These methods allow detailed geostatistical data on fine-scale models to be incorporated into coarse scale models while respecting the singular nature of the flow pattern in the well vicinity. Multi-scale finite element [23] and multi-scale finite volume [108] methods have also been applied to well modelling in heterogeneous reservoirs. Here special basis functions were introduced to locally resolve well singularities. Peaceman-type relations were used in the fine-scale model to link wellbore and well block pressures.

2.3 Unsteady-state well modelling

Mathematical models that can accurately reproduce dynamic early-time pressure behaviour are important in well test analysis. Ideally the model should include both local wellbore and global reservoir flow effects. However the difference in the spatial scale of a wellbore compared to the reservoir domain makes this a difficult problem. The use of very fine grids to model wells is undesirable within the framework of well test analysis due to computational cost, especially for field scale reservoir models with several wells, as many iterations may be required for

the parameter fitting process. Other approximations that avoid the use of fine grids have been proposed in the literature such as the use of a transient well index, analytic models developed for simplified reservoir properties, and the coupling of analytic solutions for near-wellbore effects to full scale reservoir models. These approaches to unsteady-state well modelling are reviewed below.

2.3.1 Analytic and semi-analytic models

Classical techniques such as integrating instantaneous point source solutions in time and space, Green's functions, and integral transforms have been much applied to modelling transient well behaviour. When these methods are applied to more complex wells such as partially penetrating wells or multilateral wells in three dimensions, the solution is in the form of an integral which must be evaluated numerically. Solutions obtained in this manner are often referred to as semi-analytic in the literature. Early development on modelling partially penetrating (horizontal and vertical) wells concentrated on analytic and semi-analytic well models.

Gringarten et al. [52, 53, 55] were some of the first to apply instantaneous Green's functions and Newman's product method to model line source wells. Newman's product means that for certain types of initial and boundary conditions, the solution of a 3D diffusion equation is equal to the product of the solutions of three 1D diffusion problems [52]. They derived a collection of instantaneous source functions for different simple configurations from corresponding Green's functions in an infinite reservoir. Newman's product was used to combine one-dimensional solutions to yield solutions in higher dimensions, and the method of images was used to compensate for boundaries. A similar method was applied by Carslaw and Jaeger [18] for heat conduction problems.

There are several other examples of the application of Green's function methods and instantaneous point source solutions in the development of analytic solutions for unsteady-state well modelling. Ouyang and Aziz [75] applied this method to model multilateral wells of arbitrary configurations within a reservoir. Approximating a well as a line source/sink, the pressure along the well was obtained by integrating the instantaneous point source solution along the well path. The influence of wall friction, acceleration and gravity on wellbore flow was also accounted for. Wolfsteiner et al. [106] and Valvante et al. [100] combined this

model with the model by Durlofsky [41] for near-well heterogeneity in their study of the productivity of horizontal and multilateral wells in heterogeneous reservoirs. Azar-Nejad et al. [10] used these solutions in their development of discrete flux element methods for horizontal well modelling. Economides et al. [44] used instantaneous point source solutions to formulate generalised solutions for wells of arbitrary configurations, which were then applied to derive shape factors and calculate well performance. Penmatcha and Aziz [86] used these solutions in their study of infinite-conductivity and finite-conductivity horizontal wells. Ogunsanya et al. [73] applied these solutions in their study of transient pressure behaviour of horizontal wells, where the well was modelled as a solid bar in three-dimensions instead of a line source. Other examples can be found in [29, 78, 87].

In addition to Green's function methods, integral transform methods have been employed in analytic well modelling. Goode and Thambynayagam [51] developed solutions for horizontal wells in anisotropic three-dimensional reservoirs by application of Laplace and Fourier transforms. Closed reservoir boundaries and uniform flux along the wellbore were assumed. The analytic solution was initially obtained with the well modelled by a thin rectangular strip, and then expressed in terms of an effective wellbore radius related to the length of the strip. Using this model the authors identified four distinct flow regimes for the horizontal well, giving approximate formulae for the pressure drop-down and flow time periods for each regime. Ozkan and Raghavan [76, 77] also applied Laplace transform method to obtain analytic pressure distributions for a wide variety of well configurations (for instance partially penetrating vertical wells, horizontal wells and fractured wells) in homogeneous and naturally fractured reservoirs. Point source solutions were derived in the Laplace domain, and a library of solutions in the Laplace domain was generated from the point source solution by integration and the method of images. Computational aspects of these solutions were discussed, and numerical Laplace inversion techniques are needed to obtain solutions in the time domain. Bourgeois and Couillens [16] proposed Laplace transform solutions for well productivity in terms of rate-normalised pressure drop, cumulative flow-rate, and dynamic productivity index kernel functions.

Fokker and Verga [47] modelled wells in two- and three-dimensional reservoirs by combining fundamental solutions for wells in an infinite reservoir with auxiliary sources outside the reservoir (see Figure 2.4). The positions and strengths of

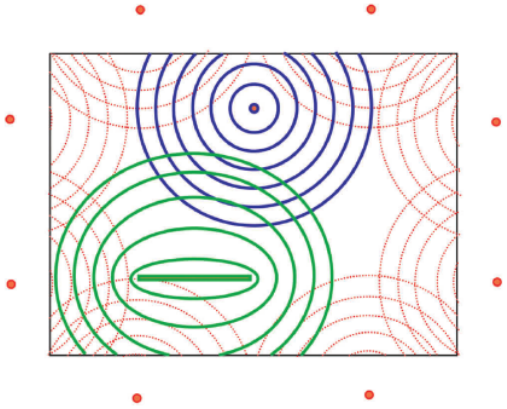

Figure 2.4: Schematic of model by Fokker and Verga [47]

these auxiliary sources were adjusted to approximate the boundary conditions of the reservoir. The common conditions on the external boundary of a reservoir are the no-flow condition (for example when bounded by an impermeable rock) and the constant pressure condition (for example when bounded by an aquifer). Solutions were computed in Laplace space and transformed to the time domain with the Stehfest algorithm. A least-squares method was used to optimise the free parameters in the solutions and near-well heterogeneity was accounted for using the model by Durlofsky [41]. The method was validated against solutions from numerical simulations and well test interpretation software.

2.3.2 Transient well index models

The conventional well index derived by Peaceman through the evaluation of an appropriate equivalent radius (see (2.12)–(2.13)) is only valid for steady-state flow. Transient well index models extend this idea to modelling early transient pressure behaviour at the wellbore. The analytic solution for a line source well producing at a constant rate q in an infinite homogeneous reservoir appears in the discussions below for the transient well index. This solution is the exponential integral function:

$$p(r,t) = \frac{q\mu}{2\pi kH}\left[-\frac{1}{2}\mathrm{Ei}\left(-\frac{\phi c_t \mu r^2}{4kt}\right)\right]. \tag{2.15}$$

Peaceman [82] proposed a time-dependent equivalent radius derived from the asymptotic expansion of the exponential integral function as the argument tends to zero. This corresponds to large dimensionless time (when time is scaled by the radius at which pressure is measured), hence this approximation is valid only at pseudo-steady state. The equivalent radius he proposed is:

$$r_{\text{eq}} = \Delta x \left[4t_D \exp(-\gamma - 4\pi p_{Db})\right]^{\frac{1}{2}}, \tag{2.16}$$

where

$$t_D = \frac{kt}{\phi c_t \mu \Delta x^2}, \qquad p_{Db} = \frac{kH}{q\mu}(p_i - p_b),$$

$\gamma = 0.5772$ is Euler's constant, p_i is the initial reservoir pressure and p_b is the well block pressure.

Blanc et al. [14] replaced the steady-state logarithmic solution in (2.11) with the time-dependent exponential integral solution to obtain a transient well index:

$$\text{WI} = \frac{4\pi kH}{\text{Ei}\left(-\frac{r_{\text{eq}}^2}{4kt}\right) - \text{Ei}\left(-\frac{r_w^2}{4kt}\right)}. \tag{2.17}$$

For greater accuracy they proposed the calculation of r_{eq} from the time-dependent exponential integral solution. They also proposed corrected transmissibility and accumulation terms to account for early time well block storage effects. They concluded that the transient well index improved early time pressure results while correcting the transmissibility and accumulation terms were less effective for early time results compared to the transient well index but more effective for late time results. (2.17) was applied by Al-Mohannadi et al. [7] to study grid and time-step requirements for horizontal wells. They concluded that using the transient well index with coarse grid blocks gave a better match between numerical and analytic results for early times, but had an adverse effect on the accuracy of numerical results when used with fine grids. Aguilar et al. [3] also applied (2.17) to investigate early time pressure transient characteristics of single and dual lateral wells, and reported a good match with analytic results.

Archer and Yildiz [9] defined the transient well index as in (2.9) but both well block and wellbore pressures were calculated from the analytic exponential integral function. The well block pressure was computed by taking the average of the exponential integral solution over the well block and simulation time-step.

This method does not require an equivalent radius to determine the well index. Comparison of simulation results from the transient well index and conventional well index method to analytic solutions showed a better performance from the transient well index.

2.3.3 Coupling models

We define coupling models as models that attempt to achieve near-well accuracy in a full scale reservoir model by combining an analytic well model with a global numerical reservoir model. This method has been widely applied to model horizontal and non-conventional wells. Some examples are discussed below.

Kurtoglu et al. [66] presented a model that couples an analytic solution related to the boundary element method in the near-well region with finite difference simulation in the rest of the reservoir. Their analytic method differs from standard boundary element methods in its use of the Green's function for a bounded domain instead of free space Green's functions. A near-well flow convergence region was defined around the wellbore (which is modelled as an internal boundary) and the pressure in this region was written as an integral along its external boundaries and the wellbore (see Figure 2.5). The coupling with the finite difference simulation was achieved by computing the flux on the boundary of the near-well region from coarse grid finite difference simulation and then using this data for analytic computations in the near-well convergence region.

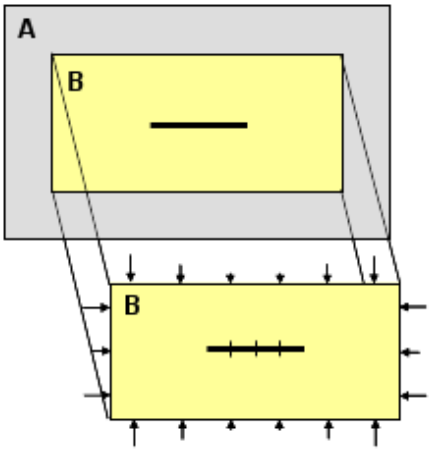

Figure 2.5: Schematic of model by Kurtoglu et al. [66]. B represents the near-well flow convergence region.

In the works of Archer and Horne [8], González-Requena and Guevara-Jordan [49] and Hales [57], an analytic solution for the near-well singularity was subtracted from the model for the flow problem. The resulting set of equations, which was solved numerically, has no singularity within the domain; rather it has a modified boundary condition to compensate for the effect. Hales [57] studied a two-dimensional problem where the analytic singular solution was the line source exponential integral solution and finite difference methods were applied to solve the modified reservoir equations. Archer and Horne [8] defined the singular solution by the exponential integral function and solved the resulting reservoir equations using Green's element method. In both cases better transient stage results were reported when compared to modelling with a conventional well index. González-Requena and Guevara-Jordan [49] obtained the analytic solution of a line source of arbitrary geometry using free space Green's functions, and the modified reservoir equations were solved by the finite element method.

2.3.4 Numerical models

Local grid refinement has been applied to unsteady-state well modelling [31, 48, 56, 69, 102, 103] despite the need for very fine grids at the well region. In these models the well is represented as an internal boundary, and the interactions between the wellbore and the reservoir are modelled explicitly. Göktas and Ertekin [48] approximated the well geometry by fine rectangular grids, whereas in [31, 56, 102] the hybrid grids by Pedrosa and Aziz [85], which combine cylindrical grids in the near-well region with rectangular grids in the rest of the reservoir, were used.

Krogstad and Durlofsky [65] developed a mixed multi-scale finite element model for reservoir flow that incorporated a drift/flux model for flow within the wellbore. The well path was fully resolved on the fine-scale using flexible grids which are close to radial around the well and rectangular away from the well. Fine-scale effects were captured through basis functions determined from numerical solutions on the underlying fine-scale geological grid.

Ding [33], Ding et al. [39] and Farina et al. [46] applied the boundary integral formulation to well modelling. The Galerkin method was applied to discretise the integral equations in [33, 39] while collocation method was applied in [46]. Non-linear wellbore flow was accounted for in [33, 46]. While the boundary

integral method is suitable for homogeneous domains, it is much more difficult to determine appropriate density functions for heterogeneous domains.

2.4 Summary

Several techniques for modelling well productivity have been reviewed in this chapter. For steady-state flow, the well index is the most widely applied model and is easily implemented in existing numerical simulators. Although originally developed for isolated, fully-penetrating vertical wells centred in uniform rectangular finite difference grids, this model has been extended to other configurations such as off-centre wells, partially-penetrating wells, horizontal and slanted wells, and flexible grids.

Analytic, semi-analytic and numerical models that capture well productivity during unsteady-state flow have also been reviewed. Analytic and semi-analytic methods are accurate for homogeneous reservoirs, but may be unable to deal with complex reservoir heterogeneity. Numerical models on the other hand have the capacity to handle complex well configurations and reservoir heterogeneity, but are limited by the need for excessively small grids in the well vicinity when coupled to a full scale reservoir grid. The method presented in this thesis is capable of providing high accuracy in the well vicinity by decoupling the fine-scale simulation in the well region from the global reservoir simulation. In this way both global and local effects are handled efficiently.

The method of decoupled overlapping grids bears some similarity to the works of Pedrosa and Aziz [85], Aavatsmark and Klausen [1] and Kurtoglu et al. [66]. In the hybrid grid model by Pedrosa and Aziz [85], the actual implementation was carried out by solving first on rectangular grids in the entire domain with the well implemented as a point source and then solving in the well region using pressure and saturation from the global solution for the boundary of the well regions. However in their implementation this process was carried out at each time-step, whereas in this work the simulation in the global domain is completed for the entire simulation time period before commencing local near-wellbore simulations. Also in [85] the production rates in the first step are allocated according to the transmissibilities on the basis of the well region solution from the previous time-step. Hence the global and local solutions are inter-dependent. In this work the

local solutions depend on the global solutions but not vice versa.

The similarity of the method studied in this thesis to the work by Aavatsmark and Klausen [1] lies in the fact that a global solution is calculated and data from that solution used as the Dirichlet boundary condition for a local solution. However in [1], the global solution is an analytic solution for steady-state flow in an infinite reservoir, and the local solution sought is a well index. In this work the global solution is calculated numerically in the reservoir domain, and the local solution is the time-dependent pressure profile in the near-well region.

In the work by Kurtoglu et al. [66], the flux distribution at the boundary of a near-well region is calculated from finite difference simulation in the reservoir domain, and the near-well solution is calculated by semi-analytic methods. In this work, solution in the near-well region is handled numerically which is more versatile compared to semi-analytic methods.

Chapter 3

Vertical Well in a Homogeneous Domain

3.1 Introduction

In this chapter the method of decoupled overlapping grids is applied to model the transient pressure of fully-penetrating vertical wells. The method is implemented in two stages (see Figure 3.1): the first stage solved in the entire domain and the second stage solved in a local near-well domain. The well is modelled as a point source or sink in the first stage, and at the end of the simulation the time-dependent solution is recorded at the external boundary of the local near-well domain. This recorded data is the Dirichlet boundary data for the second stage where the well in modelled as an internal boundary.

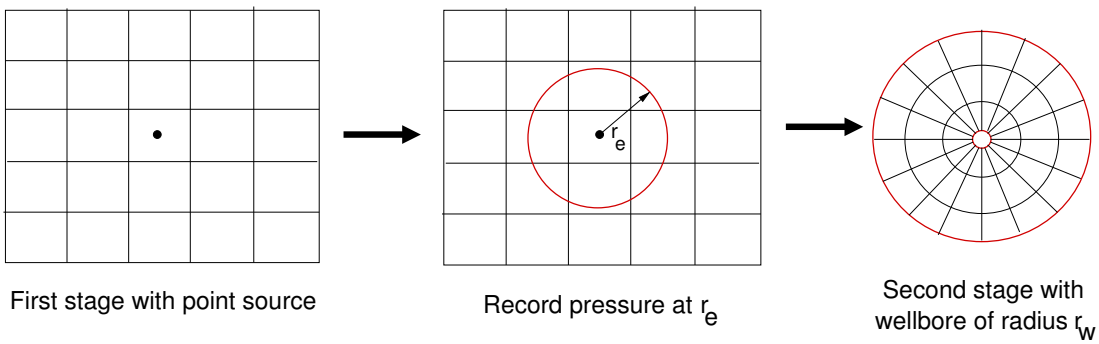

Figure 3.1: Schematic representation.

The quantity of interest in the calculations is the spatially averaged wellbore pressure. Wells are assumed to be of circular cross section and so this is simply an average in the angle variable in standard 2D polar coordinates with origin at the well centre. When the reservoir is isotropic and homogeneous and the second stage domain is the annular region as shown in Figure 3.1, then the angular averaging can be applied to the whole second stage model to give an equivalent one-dimensional model problem in the radial variable only. The second stage outer Dirichlet boundary condition is the average of the first stage solution round the outer boundary circle. When this is valid, it clearly reduces the cost and complexity of solving the second stage problem considerably and we use it wherever possible in this work.

The total error in computing the quantity of interest by the method outlined above is from two sources:

1. *Modelling error*: from approximating the external boundary data in the second stage from the solution generated by a point source well.

2. *Numerical error*: from the numerical methods that are implemented.

The modelling error and numerical error are investigated in this chapter by considering a two-dimensional homogeneous model. The modelling error is demonstrated by comparing exact analytic solutions for the point source and finite radius well problems in finite and infinite domains. The numerical error is investigated by comparing numerical solutions for the first and second stage computations to analytic solutions. A theoretical error analysis is carried out to prove the validity of observed trends in the numerical solutions. Finally a comparison of results obtained from the method to results on locally refined meshes, where the well is modelled as an internal boundary, is discussed.

3.2 Model equations

The equations of interest, which model the flow of a slightly-compressible fluid, were stated in (2.8). Ignoring gravity effects and density change, the global (first stage) equations are:

$$\phi c_t \frac{\partial p_{\text{ps}}}{\partial t}(\mathbf{x}, t) = \nabla \cdot \left(\frac{\mathbf{k}}{\mu} \nabla p_{\text{ps}}(\mathbf{x}, t) \right) + q(t)\delta(\mathbf{x} - \mathbf{x}_0), \quad \text{in } \Omega \times (0, T], \tag{3.1a}$$

$$\mathbf{n} \cdot \left(\frac{\mathbf{k}}{\mu} \nabla p_{\text{ps}}(\mathbf{x}, t) \right) = 0, \quad \text{in } \partial\Omega \times (0, T], \tag{3.1b}$$

$$p_{\text{ps}}(\mathbf{x}, 0) = 0, \quad \text{in } \Omega. \tag{3.1c}$$

Here Ω is the entire computational domain, p_{ps} represents the pressure drawdown $p_0 - p(\mathbf{x}, t)$ where p_0 is a constant initial pressure, $q(t)$ is the volumetric source strength, $\mathbf{x}_0$ is the point source location, and $\mathbf{n}$ is the normal pointing out of $\partial\Omega$.

The local (second stage) equations in the near-well region are:

$$\phi c_t \frac{\partial p_{\text{fw}}}{\partial t}(\mathbf{x}, t) = \nabla \cdot \left(\frac{\mathbf{k}}{\mu} \nabla p_{\text{fw}}(\mathbf{x}, t) \right), \quad \text{in } \Gamma \times (0, T], \tag{3.2a}$$

$$\mathbf{n} \cdot \left(\frac{\mathbf{k}}{\mu} \nabla p_{\text{fw}}(\mathbf{x}, t) \right) = -\frac{q(t)}{2\pi r_w H}, \quad \text{in } \partial\Gamma_w \times (0, T], \tag{3.2b}$$

$$p_{\text{fw}}(\mathbf{x}, t) = p_{\text{ps}}(\mathbf{x}, t), \quad \text{in } \partial\Gamma_o \times (0, T], \tag{3.2c}$$

$$p_{\text{fw}}(\mathbf{x}, 0) = 0, \quad \text{in } \Gamma. \tag{3.2d}$$

Here Γ is the post-process domain, $\partial\Gamma_w$ and $\partial\Gamma_o$ are the internal (well) and external domain boundaries respectively, p_{fw} is the pressure drawdown $p_0 - p(\mathbf{x}, t)$, $\mathbf{n}$ is the normal pointing out of the well, and $q(t)$ is the well flow rate, H is the height of the domain, and r_w is the well radius.

As noted in Section 3.1, the quantity we want to compute is the spatial average of the pressure round the wellbore. If the post-process domain has the right shape, and the reservoir is isotopic and homogeneous, this allows a reduction of the second stage problem to an equivalent problem in only one space dimension.

3.3 Analytic solutions

In this section modelling error is investigated by comparing analytic solutions for a point source well and a finite radius well. The domain is assumed to be homogeneous and isotropic. For a homogeneous anisotropic domain, a linear transformation of the coordinates

$$x' = \frac{x}{\sqrt{k_x}}, \quad y' = \frac{y}{\sqrt{k_y}}, \tag{3.3}$$

reduces the equations to an isotropic form.

3.3.1 Infinite domain

A vertical well completed in the entire thickness of an infinite, homogeneous, isotropic domain, and producing at a constant rate, will induce radially symmetric flow described by the diffusion equation:

$$\frac{1}{\eta}\frac{\partial p}{\partial t} = \frac{\partial^2 p}{\partial r^2} + \frac{1}{r}\frac{\partial p}{\partial r}, \tag{3.4a}$$

$$p(r, 0) = 0, \tag{3.4b}$$

$$p(r \to \infty, t) = 0, \tag{3.4c}$$

together with an additional condition for the well source term. Here $\eta = k/(\phi c_t \mu)$ is the diffusivity coefficient. Analytic solutions for a point source and finite radius well are given below. Note that p_{ps} and p_{fw} below are pressure drawdowns.

Point source well

Here the additional condition is

$$\lim_{r \to 0} \left(r \frac{\partial p_{\text{ps}}}{\partial r} \right) = -Q, \tag{3.5}$$

where $Q = q\mu/(2\pi kH)$, H is the height of the domain. The solution to (3.4) with (3.5) is the well known exponential integral function (see derivation in Appendix

A.1):

$$p_{\mathrm{ps}}(r,t) = -\frac{Q}{2}\mathrm{Ei}\left(-\frac{r^2}{4\eta t}\right). \tag{3.6}$$

Finite radius well

Here the additional condition is

$$r\frac{\partial p_{\mathrm{fw}}}{\partial r}\bigg|_{r=r_w} = -Q. \tag{3.7}$$

A closed form solution for (3.4) with (3.7) can be found [96]:

$$p_{\mathrm{fw}} = QP(r_D, t_D), \tag{3.8}$$

$$P(r_D, t_D) = \frac{2}{\pi}\int_0^\infty \left(1 - e^{-a^2 t_D}\right)\frac{[J_1(a)Y_0(ar_D) - Y_1(a)J_0(ar_D)]}{a^2[J_1^2(a) + Y_1^2(a)]}\,da, \tag{3.9}$$

where $r_D = r/r_w$, $t_D = \eta t/r_w^2$, a is the variable of integration, $J_0(x), J_1(x)$ are Bessel functions of the first kind and $Y_0(x), Y_1(x)$ are Bessel functions of the second kind. (3.9) is not numerically tractable due to the high oscillatory nature of the numerator in the integrand for large values of a. Alternatively a solution can be obtained by use of Laplace transform methods (see derivation in Appendix A.2):

$$\hat{p}_{\mathrm{fw}}(r,s) = \frac{Q\sqrt{\eta}K_0\left(r\sqrt{s/\eta}\right)}{r_w(\sqrt{s})^3 K_1(r_w\sqrt{s/\eta})}, \tag{3.10}$$

where $\hat{p}_{\mathrm{fw}}(r,s)$ is the solution in Laplace space, s is the Laplace transform variable, and K_0, K_1 are modified Bessel functions of the second kind. The inversion of (3.10) to the real time domain is carried out numerically using the Iseger algorithm [63].

Iseger algorithm

Although the Stehfest algorithm [95] is commonly used for numerical Laplace inversion in petroleum engineering, it suffers from some limitations such as inability to handle singularities and discontinuities [6], and inability to handle functions with an oscillatory response (such as sine and wave functions) and e^t type functions [58]. The Iseger algorithm [63] is more robust: it is able to compute the inverse Laplace transforms of functions with discontinuities and singularities, even if the points of discontinuity and singularity are not known a priori, and can also deal with locally non-smooth and unbounded functions. The algorithm is a Fourier series method, and utilises the well-known Poisson summation formula to relate an infinite sum of Laplace transform values to the z-transform of the function values. The infinite sum is approximated with a finite sum using a Gaussian quadrature rule, and the function values are calculated using the FFT algorithm. The results from this algorithm were shown by Iseger [63] to be near machine precision.

The algorithm used in this section to compute function values of $f(l), l = 0, 1, \ldots, M-1$ from its Laplace transform $\hat{f}(s)$, is stated in Table 3.1. The values at $f(l\Delta)$ can be obtained be applying the algorithm to the scaled Laplace transform

$$\mathcal{L}[f(l\Delta)] = \frac{1}{\Delta}\hat{f}\left(\frac{s}{\Delta}\right). \tag{3.11}$$

Here $\Delta = t/(M-1)$, where t is the period for the inversions, and M is the number of points at which the Laplace transform is computed. In Table 3.1, n represents the number of quadrature nodes used in the algorithm and so controls the accuracy. $n = 16$ is recommended in [63] to give machine precision accuracy for all smooth functions. Simulation results for the numerical inversion of (3.10) using $n = 16$ and 32 did not show significant difference, hence $n = 16$ is used here in all computations. The quadrature nodes λ_j and weights β_j are given in [63] for $n = 16, 32, 48$.

Input $\hat{f}, \Delta, M$ where M is a power of 2

Output $f(l\Delta)$, $l = 0, 1, \ldots, M-1$.

Parameters $M_2 = 8M, a = \dfrac{44}{M_2}, n = 16$

Steps 1. For $k = 0, 1, \ldots, M_2$ and $j = 1, 2, \ldots, n/2$, compute

$$\hat{f}_{jk} = \mathbf{Re}\left[\hat{f}\left(\frac{a + i\lambda_j + \dfrac{2\pi i k}{M_2}}{\Delta}\right)\right]$$

$$\hat{f}_k = \frac{2}{\Delta}\sum_{j=1}^{n/2}\beta_j \hat{f}_{jk}\ ; \quad \hat{f}_0 = \frac{1}{\Delta}\sum_{j=1}^{n/2}\beta_j(\hat{f}_{j0} + \hat{f}_{jM_2})$$

2. For $l = 0, 1, \ldots, M_2 - 1$, compute

$$f_l = \frac{1}{M_2}\sum_{k=0}^{M_2-1}\hat{f}_k \cos\left(\frac{2\pi l k}{M_2}\right)$$

using the inverse FFT algorithm.

3. Set $f(l\Delta) = e^{al} f_l$ for $l = 0, 1, \ldots, M-1$

Table 3.1: Iseger algorithm

Comparison of analytic point source well and finite radius well solutions

Figure 3.2 shows the absolute error in dimensionless pressure drawdown plotted against dimensionless time. The dimensionless pressure drawdown is given by

$$\frac{p(r,0) - p(r,t)}{-Q}, \quad \text{where } Q = \frac{q\mu}{2\pi k H}, \tag{3.12}$$

and $p(r,0) = 0$. The dimensionless time is $t_D = \eta t / r^2$.

The time domain is divided into subintervals within which the numerical inversion of (3.10) is performed. M is kept constant for each subinterval, and since the Iseger algorithm computes function values for $t = 0 \ldots (M-1)\Delta$, larger values of Δ are required for larger subintervals. This introduces some additional error for late times as shown in Figure 3.2(a). By also computing the point source

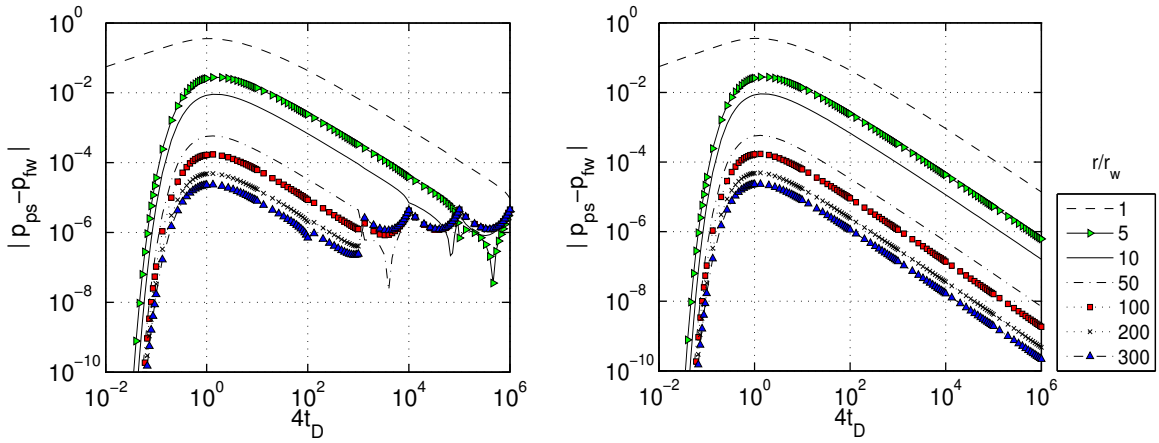

(a) p_{ps} from (3.6) **(b)** p_{ps} from inverting (3.13)

Figure 3.2: Absolute error in dimensionless pressure drawdown versus dimensionless time in an infinite domain.

solution p_{ps} from its Laplace transform

$$\hat{p}_{\text{ps}}(r,s) = \frac{Q}{s} K_0(r\sqrt{s/\eta}) \tag{3.13}$$

using the Iseger algorithm, the error introduced by the algorithm for large Δ cancels out in $|p_{\text{ps}} - p_{\text{fw}}|$ to give expected results shown in Figure 3.2(b).

The nature of the modelling error is seen in Figure 3.2(b). The absolute errors $|p_{\text{ps}} - p_{\text{fw}}|$ for all $r_D = r/r_w$ rise to a peak value at early time, and then decrease with time. Also the peak error decreases as r_D increases. According to [96], the ratio r_D ceases to be influential for large dimensionless time, and from $4t_D > 200$ the point source solution approximates the finite well solution with an error not exceeding 1%. This can be seen in Figure 3.2(b).

3.3.2 Finite domain

The finite domain equations are given in (3.14) and (3.15) below.

Point source well

$$\phi c_t \frac{\partial p_{\text{ps}}}{\partial t}(\mathbf{x}, t) = \frac{k}{\mu}\nabla^2 p_{\text{ps}}(\mathbf{x}, t) + q\delta(\mathbf{x} - \mathbf{x}_0), \qquad \text{in } \Omega \times (0, T], \tag{3.14a}$$

$$\mathbf{n} \cdot \frac{k}{\mu}\nabla p_{\text{ps}}(\mathbf{x}, t) = 0, \qquad \text{in } \partial\Omega_o, \tag{3.14b}$$

$$p_{\text{ps}}(\mathbf{x}, 0) = 0, \qquad \text{in } \Omega. \tag{3.14c}$$

Finite radius well

$$\phi c_t \frac{\partial p_{\text{fw}}}{\partial t}(\mathbf{x}, t) = \frac{k}{\mu}\nabla^2 p_{\text{fw}}(\mathbf{x}, t), \qquad \text{in } \Omega \times (0, T], \tag{3.15a}$$

$$\mathbf{n} \cdot \frac{k}{\mu}\nabla p_{\text{fw}}(\mathbf{x}, t) = 0, \qquad \text{in } \partial\Omega_o \times (0, T], \tag{3.15b}$$

$$\mathbf{n} \cdot \nabla p_{\text{fw}}(\mathbf{x}, t) = -Q, \qquad \text{in } \partial\Omega_w \times (0, T], \tag{3.15c}$$

$$p_{\text{fw}}(\mathbf{x}, 0) = 0, \qquad \text{in } \Omega. \tag{3.15d}$$

Here Ω is a rectangle of dimensions $x_e \times y_e$ with no-flow Neumann boundary conditions prescribed at the outer domain boundary $\partial\Omega_o$, $\partial\Omega_w$ is the surface of the wellbore, and $\mathbf{n}$ is the normal vector pointing out of the domain. The parameters $(q, k, \mu, H, c_t, \phi)$ are set to 1.

The results in this section are obtained by the method of images using the infinite domain analytic solutions derived in the previous section. This problem satisfies the conditions outlined in Section 3.1 for the reduction of the second stage, near-well calculation to a problem in one (radial) space dimension only. Using the centre of the well as the origin, the quantities of interest are the pressure values averaged around circles of radius r. The contribution of each image i to the average pressure at radius r is computed by first evaluating its contribution

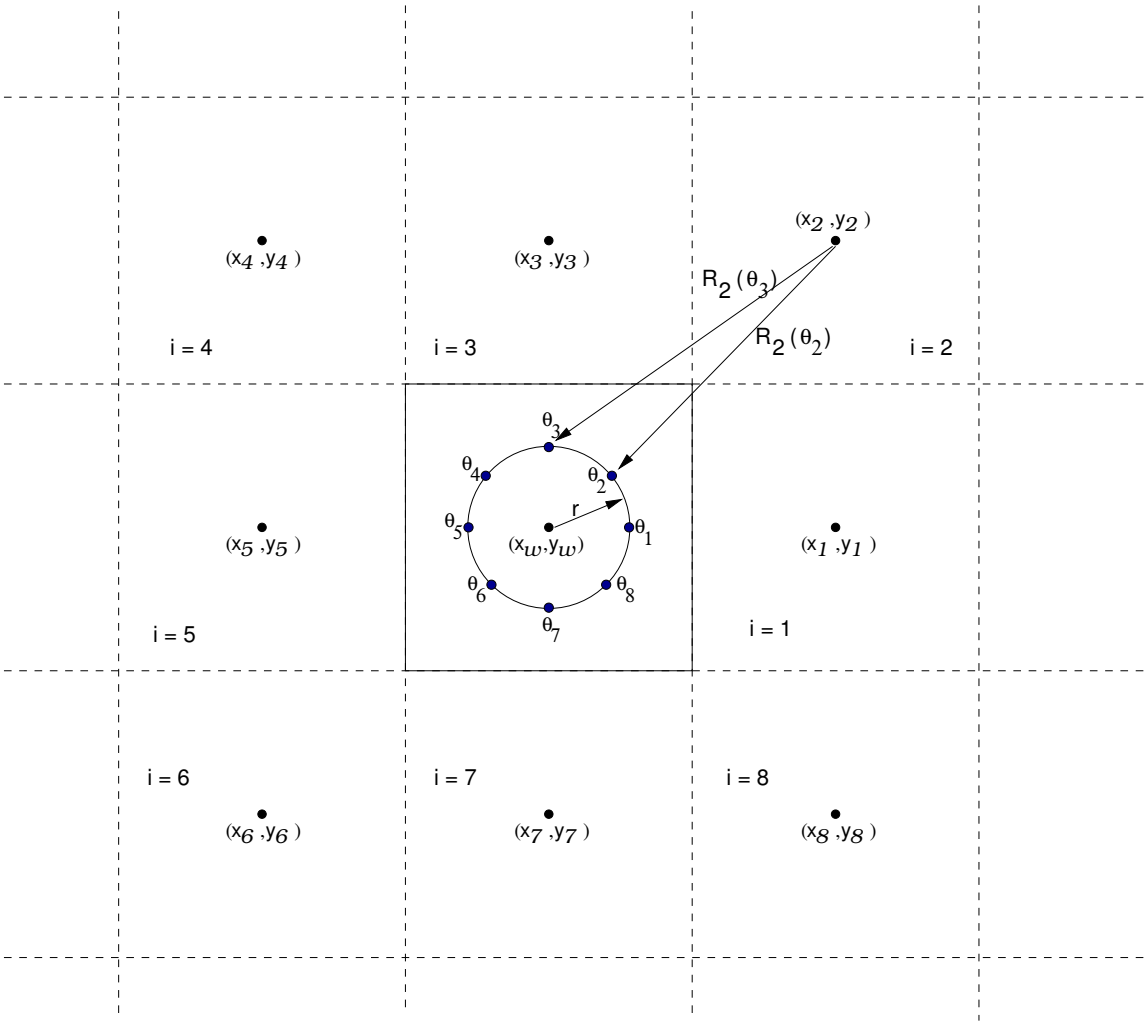

Figure 3.3: Construction of $p_\alpha(r,t)$ in (3.16). Each point $\theta_k, k = 1,\ldots,8$ on the circle makes an angle θ_k with the x–axis.

at discrete points θ_k on the circle and then taking the average in θ:

$$p_\alpha(r,t) = \sum_i \overline{p}_\alpha(R_i,t), \quad \alpha = \text{ps or fw}, \tag{3.16}$$

$$R_i(\theta_k) = \sqrt{(x_w + r\cos\theta_k - x_i)^2 + (y_w + r\sin\theta_k - y_i)^2}, \tag{3.17}$$

where $\overline{p}$ represents the average pressure in θ, and (x_w, y_w) is the location of the centre of the well (see Figure 3.3). For a rectangle of dimensions $x_e \times y_e$, with n

the image counter in the x-direction and m the image counter in the y-direction,

$$x_i = 2nx_e \pm x_w, \quad y_i = 2my_e \pm y_w. \tag{3.18}$$

In the simulations carried out in this section, $n, m = -N_{\text{img}} \ldots N_{\text{img}}$, and the series is truncated at $R_i \leq N_{\text{img}}$.

The method of images solution in (3.16)–(3.18) converges rapidly for short time and slowly for long time. An equivalent form can be derived for the point source problem, either from Poisson's summation formula [18, chap. 10] or from solving the point source equations in (3.14) by Fourier decomposition, to give:

$$\begin{aligned} p_{\text{ps}}(x,y,t) = \frac{4}{x_e y_e}\Bigg\{ & \frac{t}{4} + \frac{1}{2}\sum_{n=1}^{\infty} \frac{x_e^2}{n^2\pi^2}\left[1-\exp\left(-\frac{n^2\pi^2}{x_e^2}t\right)\right]\cos\frac{n\pi x_w}{x_e}\cos\frac{n\pi x}{x_e} + \\ & \frac{1}{2}\sum_{k=1}^{\infty} \frac{y_e^2}{k^2\pi^2}\left[1-\exp\left(-\frac{k^2\pi^2}{y_e^2}t\right)\right]\cos\frac{k\pi y_w}{y_e}\cos\frac{k\pi y}{y_e} + \\ & \sum_{n=1}^{\infty}\sum_{k=1}^{\infty} \frac{x_e^2 y_e^2}{\pi^2(n^2y_e^2+k^2x_e^2)}\left[1-\exp\left(-\left[\frac{n^2\pi^2}{x_e^2}+\frac{k^2\pi^2}{y_e^2}\right]t\right)\right]\cos\frac{n\pi x_w}{x_e}\cos\frac{k\pi y_w}{y_e}\cos\frac{n\pi x}{x_e}\cos\frac{k\pi y}{y_e}\Bigg\}, \end{aligned} \tag{3.19}$$

for a rectangle of dimensions $x_e \times y_e$, with parameters $(q, k, \mu, h, c_t, \phi)$ set to 1 and (x_w, y_w) the point source location. This Fourier series form complements the method of images form, converging slowly for short time and rapidly for long time. The average pressure at radius r is found by integrating (3.19):

$$p_{\text{ps}}(r,t) = \frac{1}{2\pi}\int_0^{2\pi} p_{\text{ps}}(x_w + r\cos\theta, y_w + r\sin\theta, t)\, d\theta \tag{3.20}$$

to get (see Appendix A.3)

$$p_{\mathrm{ps}}(r,t) = \frac{4}{x_e y_e}\left\{\frac{t}{4} + \frac{1}{2}\sum_{n=1}^{\infty}\frac{x_e^2}{n^2\pi^2}\left[1-\exp\left(-\frac{n^2\pi^2}{x_e^2}t\right)\right]\cos^2\frac{n\pi x_w}{x_e}J_0(n\pi r/x_e) + \right.$$
$$\frac{1}{2}\sum_{m=1}^{\infty}\frac{y_e^2}{m^2\pi^2}\left[1-\exp\left(-\frac{m^2\pi^2}{y_e^2}t\right)\right]\cos^2\frac{m\pi y_w}{y_e}J_0(m\pi r/y_e) +$$
$$\left.\sum_{n=1}^{\infty}\sum_{m=1}^{\infty}\frac{x_e^2y_e^2}{\pi^2(n^2y_e^2+m^2x_e^2)}\left[1-\exp\left(-\left[\frac{n^2\pi^2}{x_e^2}+\frac{m^2\pi^2}{y_e^2}\right]t\right)\right]\cos^2\frac{n\pi x_w}{x_e}\cos^2\frac{m\pi y_w}{y_e}J_0\left(\pi r\sqrt{\frac{n^2}{x_e^2}+\frac{m^2}{y_e^2}}\right)\right\}. \tag{3.21}$$

J_0 is the Bessel function of the first kind.

To reduce computation time for the analytic point source solution, the method of images is used at early time and the Fourier series solution is used at late time. The difference in the two solutions for some r is plotted in Figure 3.4. Here $x_e = 1, y_e = 1, (x_w.y_w) = (0.5, 0.5)$, and $r_w = 0.001$. Based on this a switch between the two methods is made at $4t_D = 100$, for $N_{\mathrm{img}} = 32$ and $N_{\mathrm{Fourier}} = 500$ terms. For the finite radius well solution, $N_{\mathrm{img}} = 128$ was found to give accurate solutions in the desired time interval $4t_D \in [10^{-2}, 10^4]$.

We note that an analytic upper bound on the error in the point source image solution truncated at $R_i \leq N_{\mathrm{img}}$ can be derived. For an image sum truncated at radius R_i from the point source, the contribution E of the remainder of the images satisfies:

$$E \leq 2\pi Q\int_{R_i'}^{\infty} -\frac{1}{2}\mathrm{Ei}\left(-\frac{r^2}{4\eta t}\right) r\,dr\;; \quad R_i' < R_i \tag{3.22}$$
$$= 2\pi Q\left[-\frac{r^2}{4}\mathrm{Ei}\left(-\frac{r^2}{4\eta t}\right) - \eta t\exp\left(-\frac{r^2}{4\eta t}\right)\right]_{R_i'}^{\infty} \tag{3.23}$$
$$= 2\pi Q\left[\eta t\exp\left(-\frac{R_i'^2}{4\eta t}\right) - \frac{R_i'^2}{4}\left\{-\mathrm{Ei}\left(-\frac{R_i'^2}{4\eta t}\right)\right\}\right]. \tag{3.24}$$

The analytic error bound (3.24) is plotted in Figure 3.4 for $R_i' = 30$.

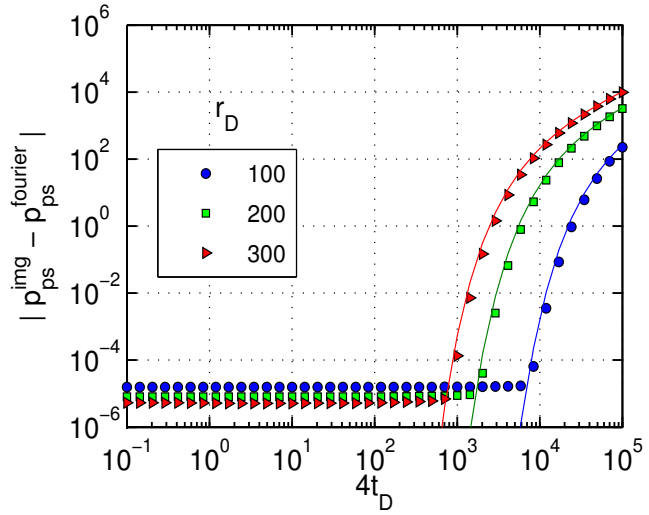

Figure 3.4: *Markers*: difference in dimensionless pressure for point source problem computed by method of images (32 images) and Fourier series (500 terms). *Lines*: analytic error bound E from (3.24) at corresponding r_D for $R_i = 30$. $r_D = r/r_w$.

The modelling error in both infinite and finite domains is plotted in Figure 3.5(a). It shows that both errors are the same initially, but boundary effects cause the errors in a finite domain to settle to a near-constant value at later time. Figure 3.5(b) clearly shows the image contribution (and hence the boundary effects) to the infinite domain solution leading to a flattening of the error values for late time.

Figure 3.6 shows the absolute error in dimensionless pressure drawdown computed for two well radii: 0.001 and 0.01. It demonstrates that the errors initially depend only on the ratio $r_D = r/r_w$. However since given the same r_D the measurement radius r is larger for larger r_w, the effects of the boundary are felt at an earlier time for larger r_w. Therefore as shown in Figure 3.6 the error for $r_w = 0.01$ gets to steady-state at an earlier time compared to that for $r_w = 0.001$.

We conclude that for radial measurements taken at a sufficient distance from the domain boundary, the maximum modelling error occurs during an initial transient phase, and is determined by the difference in the point source and finite radius well solutions in an infinite domain. This initial transient phase is absent for measurements made close to the domain boundary, and in this case the maximum modelling error is determined by the pseudo-steady state error. We draw attention to the fact that these results have been presented in terms of

a dimensionless time scaled by the measurement radius, so results for the larger (dimensionless) radii represent measurements taken at a later time compared to results for smaller radii.

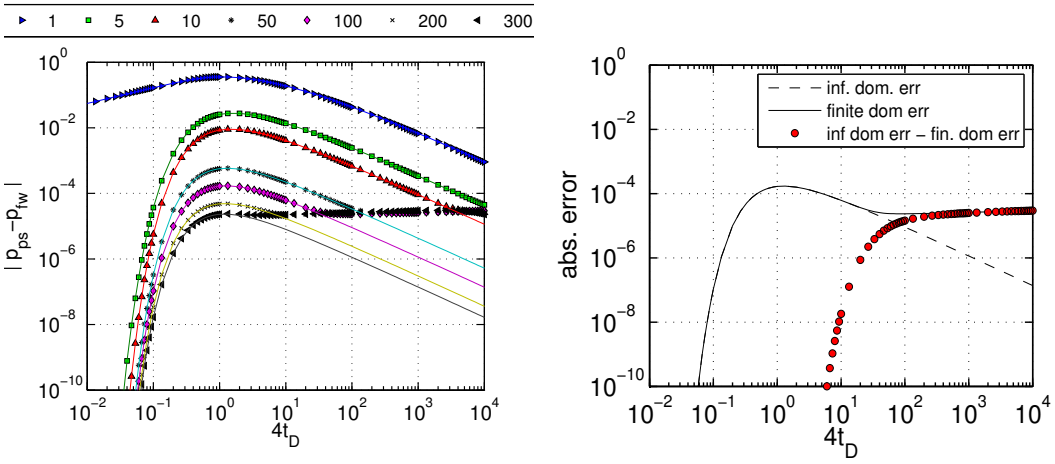

(a) Absolute error. *Markers*: Finite domain. *Lines*: Infinite domain. Legend: r_D

(b) Absolute error contributions at $r_D = 100$.

Figure 3.5: Absolute error in dimensionless pressure drawdown against dimensionless time in a finite domain. $r_w = 0.001$.

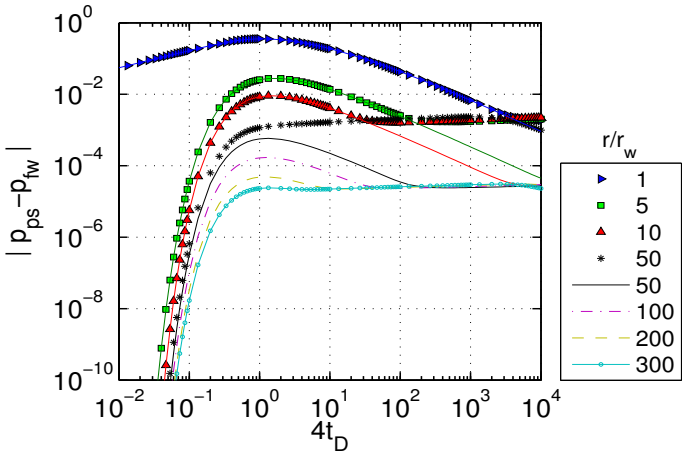

Figure 3.6: Absolute error in dimensionless pressure drawdown for $r_w = 0.001, 0.01$. *Markers*: $r/r_w = 1, 5, 10, 50$; $r_w = 0.01$. *Lines*: $r/r_w = 1, 5, 10, 50, 100, 200, 300$; $r_w = 0.001$.

It is interesting to note the relationship between the maximum error in dimensionless absolute pressure $\max(|p_{\text{ps}} - p_{\text{fw}}|)$, and the dimensionless radius r_D, shown in Figure 3.7. A closed-form expression for this relationship is derived in Appendix A.4:

$$\max(|p_{\text{ps}} - p_{\text{fw}}|) \approx \frac{Q \exp(-1)(1 + 2\ln(r_D) - 2\gamma)}{2r_D^2} \quad \text{as} \quad r_D \to \infty. \tag{3.25}$$

This estimate is also plotted in Figure 3.7.

It is seen in Figure 3.7 that the estimate (3.25) gives excellent predictions of the error over much of the range of r_D. However, the estimate is not valid as r_D gets smaller, and the results deviate from the prediction when r_D is big enough that measurement points are on or close to the outer boundary of the original, physical domain, for example the outliers at $r_D = 300$ for $r_w = 0.001$, and at $r_D = 50$ for $r_w = 0.01$.

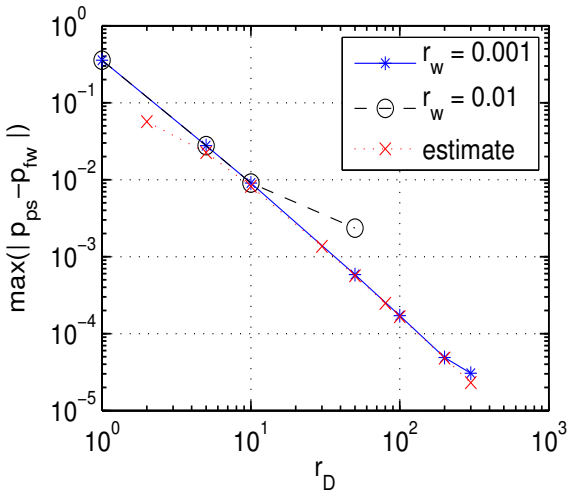

Figure 3.7: Maximum error in Figure 3.6, and estimate from (3.25), plotted against dimensionless radius.

3.4 Numerical solutions

In this section numerical error is investigated by comparing numerical solutions to the analytic solutions derived in the previous section. The equations for the global and local problems that are solved with a point source well and a finite radius well were stated in (3.1) and (3.2) respectively. They are stated again below:

Global equations (point source well)

$$\phi c_t \frac{\partial p_{\text{ps}}}{\partial t}(\mathbf{x}, t) = \frac{k}{\mu}\nabla^2 p_{\text{ps}}(\mathbf{x}, t) + q\delta(\mathbf{x} - \mathbf{x}_0), \qquad \text{in } \Omega \times (0, T], \tag{3.26a}$$

$$\mathbf{n} \cdot \frac{k}{\mu}\nabla p_{\text{ps}}(\mathbf{x}, t) = 0, \qquad \text{in } \partial\Omega_o, \tag{3.26b}$$

$$p_{\text{ps}}(\mathbf{x}, 0) = 0, \qquad \text{in } \Omega. \tag{3.26c}$$

Local equations (finite radius well)

$$\phi c_t \frac{\partial p_{\text{fw}}}{\partial t}(\mathbf{x}, t) = \frac{k}{\mu}\nabla^2 p_{\text{fw}}(\mathbf{x}, t), \qquad \text{in } \Gamma \times (0, T], \tag{3.27a}$$

$$p_{\text{fw}}(\mathbf{x}, t) = p_{\text{ps}}(\mathbf{x}, t), \qquad \text{in } \partial\Gamma_o \times (0, T], \tag{3.27b}$$

$$\mathbf{n} \cdot \nabla p_{\text{fw}}(\mathbf{x}, t) = -\frac{q\mu}{2\pi r_w k H}, \qquad \text{in } \partial\Gamma_w \times (0, T], \tag{3.27c}$$

$$p_{\text{fw}}(\mathbf{x}, 0) = 0, \qquad \text{in } \Gamma. \tag{3.27d}$$

Here Ω is the global domain with external boundary represented by $\partial\Omega_o$, and Γ is the local post-process domain with internal (well) and external boundaries represented by $\partial\Gamma_w$ and $\partial\Gamma_o$ respectively. The parameters $(q, k, \mu, H, c_t, \phi)$ are the same as in Section 3.3.2. Other simulation parameters are listed in Table 3.2.

Parameter	Value
x_e, y_e	1,1
(x_w, y_w)	(0.5,0.5)
r_w	10^{-3}
r_e	0.1, 0.2, 0.3

Table 3.2: Simulation parameters. (x_w, y_w) = well location, r_w = well radius, r_e = radius of post-process domain.

3.4.1 Error in first stage (point source well solution)

The global equations are semi-discretised on a finite element mesh generated in Matlab [70]. Time integration is performed using ode15s, a Matlab variable order initial-value ODE stiff solver. The equations are stiff because there is a rapid dynamic change of the solution near the wellbore compared to the rest of the reservoir which introduces different time scales for the problem. The location of the point source is not constrained to a vertex, rather the vertices of the triangle enclosing the point source are assigned weights depending its location. The solution at radius r_e is obtained by interpolating the global solution from the background grid to N_θ points on r_e and then taking the average. We start by discussing the contributions to the numerical error in the average measurements taken at r_e before presenting the error convergence results for this section.

The contributions to the numerical error in the average pressure at r_e come from the finite element approximation, and interpolation from the finite element mesh to N_θ points on r_e. We investigate the contributions from these two sources of error by comparing the absolute error in the average pressure at r_e interpolated from the finite element solution to that interpolated from the analytic solution, where both solutions are evaluated at the same vertices for the interpolation. Triangle-based linear interpolation is used in both cases. The different mesh refinements considered are shown in Figure 3.8 and Figure 3.10 for $r_e = 0.1$ and 0.2 respectively. Case 1 is the base case. Case 2 is obtained by regular refinement of Case 1 (that is, each triangle in Case 1 is divided into four triangles of the same shape resulting in a mesh size that is half of the original). Case 3 is obtained by locally refining Case 1 at the point source location, and Case 4 is obtained by locally refining Case 1 at the radius r_e. The corresponding absolute errors in the average pressure at r_e interpolated from the mesh configurations in Figure

3.8 and Figure 3.10 are shown in Figure 3.9 and Figure 3.11 respectively. Here the absolute errors are with respect to the analytic solutions at r_e calculated in Section 3.3.2.

The error in the finite element approximation and linear interpolation both contribute to the final error in the average pressure interpolated from the finite element solution. On the other hand only the error in the linear interpolation contributes to the final error in the average pressure interpolated from the analytic solution. However Figure 3.9 and Figure 3.11 show that only in Case 4 is the error in the average pressure interpolated from the analytic solution less than or equal to that interpolated from the finite element solution for all simulation time. For Case 1 and Case 2 in Figure 3.9, and Case 1 to Case 3 in Figure 3.11, there appears to be some cancellation of the error contributions from the finite element approximation and the linear interpolation, resulting in a lower error in the average pressure at r_e interpolated from the finite element solution compared to the error in the average pressure at r_e interpolated from the analytic solution.

Figure 3.9 and Figure 3.11 also show that refining the base case (Case 1) locally at the point source (Case 3) and at radius r_e (Case 4) leads to an increase in the error at steady-state for the average pressure at r_e interpolated from the finite element solution, while refining uniformly in the entire domain (Case 2) results in a lower error profile for the entire simulation time (initial transient to steady-state). This suggests that mesh refinement for the global problem should be carried out in the entire domain rather than locally.

It should be kept in mind that the most likely practical use for the decoupled overlapping grid method is as a post-processing step using data derived from a standard reservoir simulator. In that case there is likely to be little control over the mesh refinement. However if detailed mesh control is available, future work should also include an investigation of goal adaptive refinement [5, Chap. 8] to evaluate the pressure at radius r_e from the point source.

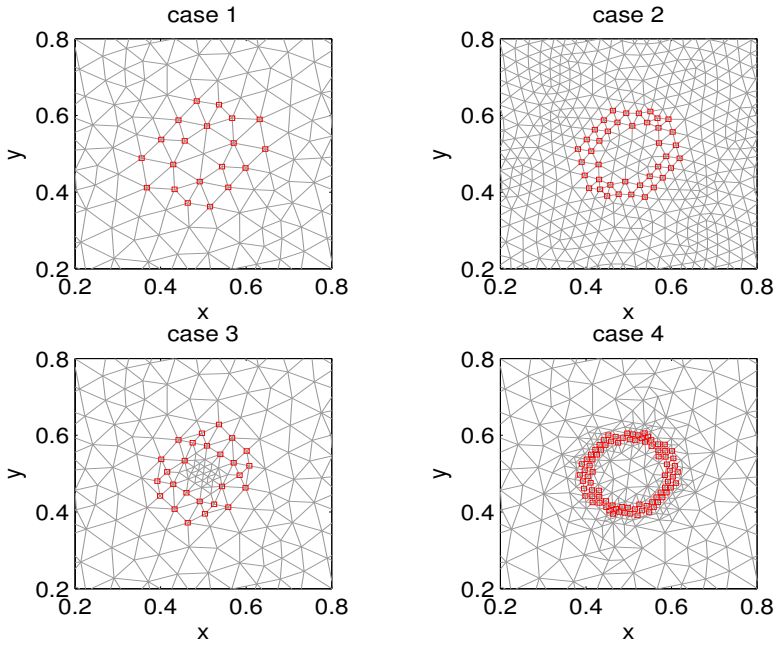

Figure 3.8: Different refinements of the global mesh showing vertices used in the interpolation to radius $r_e = 0.1$.

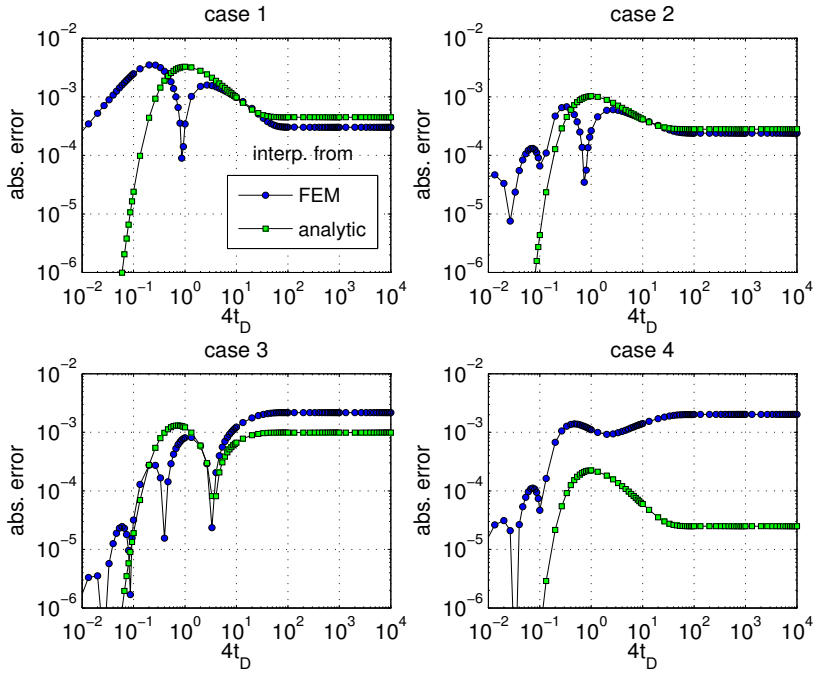

Figure 3.9: Absolute error in the average pressure at $r_e = 0.1$, interpolated linearly from finite element approximation and analytic solution at the vertices shown in Figure 3.8.

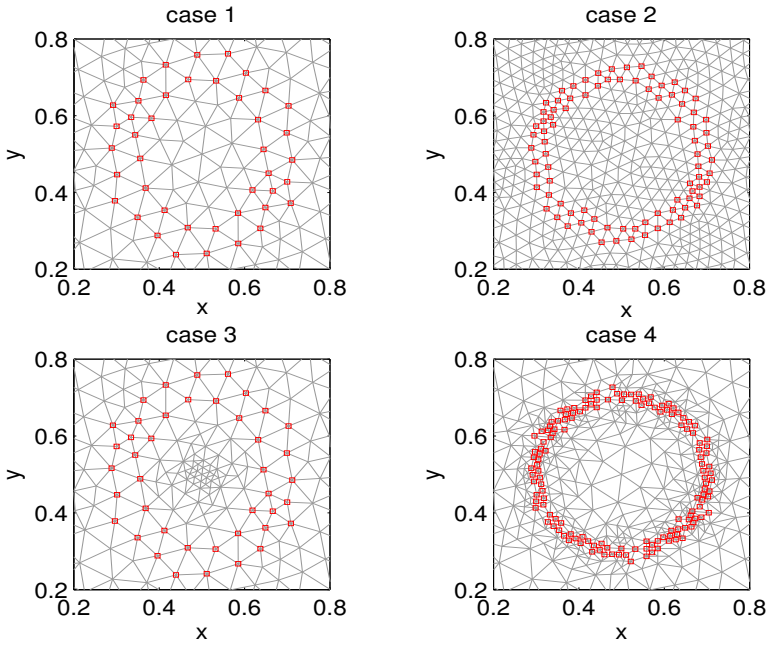

Figure 3.10: Different refinements of the global mesh showing vertices used in the interpolation to radius $r_e = 0.2$.

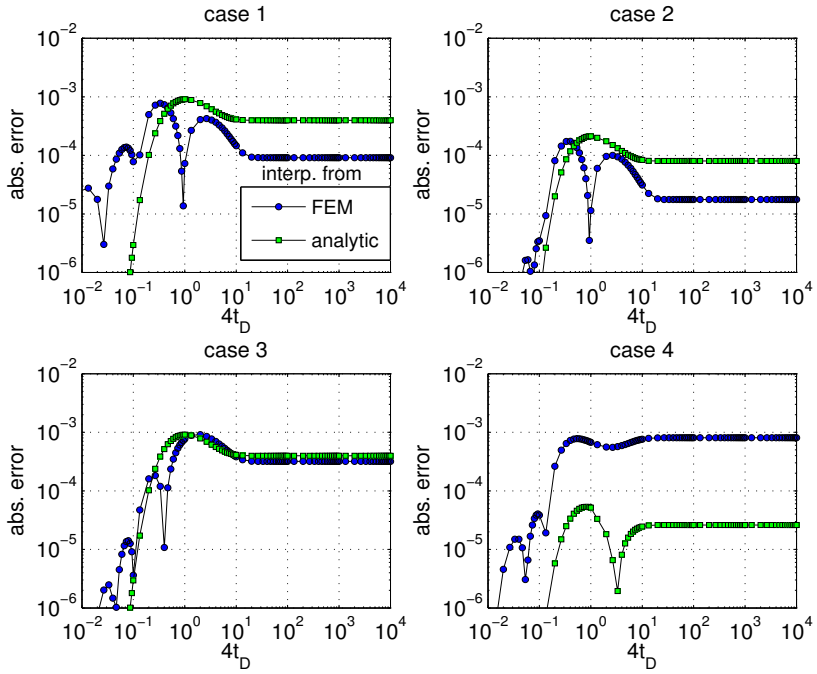

Figure 3.11: Absolute error in the average pressure at $r_e = 0.2$, interpolated linearly from finite element approximation and analytic solution at the vertices shown in Figure 3.10.

Figure 3.12 shows a comparison of the absolute error in the average pressure at r_e interpolated from the finite element solution by triangle-based linear and cubic interpolation. It is seen that the maximum absolute error for the result from cubic interpolation is higher than that from linear interpolation for all the plots. This is because triangle-based cubic interpolation assumes an extra smoothness of the underlying global solution (which is not the case here since the underlying global solution is calculated on a finite element mesh using piecewise linear Lagrange elements). The triangle-based linear interpolation is more accurate since linear interpolation is carried out on a piecewise-linear function. Therefore linear interpolation will be used in the rest of this work to compute the external boundary data of the local problem from the global problem.

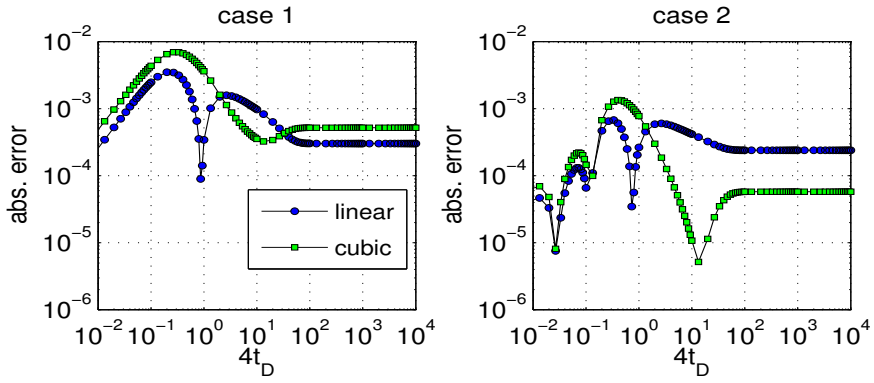

(a) $r_e = 0.1$, mesh for Case 1 and Case 2 shown in Figure 3.8.

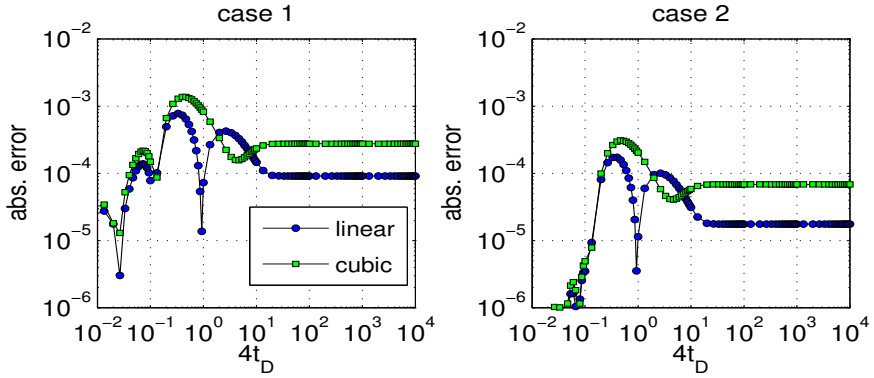

(b) $r_e = 0.2$, mesh for Case 1 and Case 2 shown in Figure 3.10.

Figure 3.12: Comparison of linear and cubic interpolation of the finite element solution from the global mesh to r_e.

Figure 3.13 shows the absolute maximum error in average dimensionless pressure at fixed radii $r_D = r_e/r_w$ taken over the dimensionless time interval $4t_D \in [10^{-2}, 10^4]$, plotted against the degrees of freedom (d.o.f) of the different levels of refinement. Each refinement level is obtained by regular mesh refinement of the previous level. $p_{\text{ps,ana}}$ and $p_{\text{fw,ana}}$ denote the analytic solutions for a point source and a finite radius well respectively, which were computed in Section 3.3.2. p_{ps} is the numerical solution of (3.26). The solid lines represent the maximum numerical error in the average dimensionless pressure at r_e given by $\max(|p_{\text{ps}}(r_e,t) - p_{\text{ps,ana}}(r_e,t)|)$, while the broken lines represent the maximum of the sum of the numerical and modelling error given by $\max(|p_{\text{ps}}(r_e,t) - p_{\text{fw,ana}}(r_e,t)|)$. It is seen that the modelling error at these r_e is noticeable only for significantly fine mesh sizes.

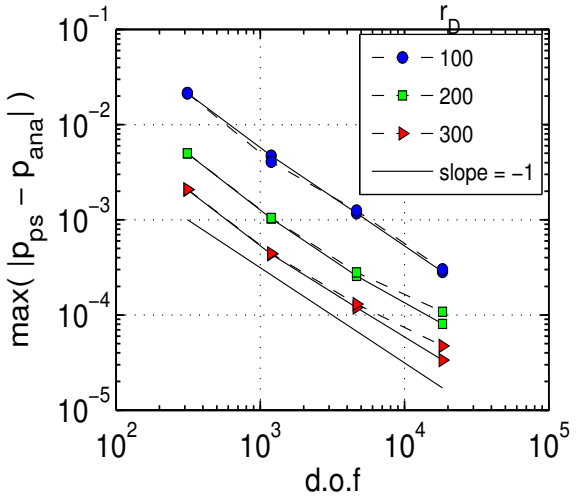

Figure 3.13: Maximum absolute error in average dimensionless pressure at r_D, measured over time interval $4t_D \in [10^{-2}, 10^4]$. *Solid lines*: $\max(|p_{\text{ps}}(r_e,t) - p_{\text{ps,ana}}(r_e,t)|)$. *Broken lines*: $\max(|p_{\text{ps}}(r_e,t) - p_{\text{fw,ana}}(r_e,t)|)$.

Also shown in Figure 3.13 is a line of slope -1, which by comparison to the absolute maximum error plots indicates an $\mathcal{O}(h^2)$ convergence, where h denotes the mesh size. This convergence rate will be proved theoretically in Section 3.5.

Figure 3.14 shows the time profile of the absolute error measured at the different r_e. It is seen that the maximum error occurs during an initial transient phase before the error settles to a steady-state value, similar to the absolute error in the analytic solutions plotted in Figure 3.5.

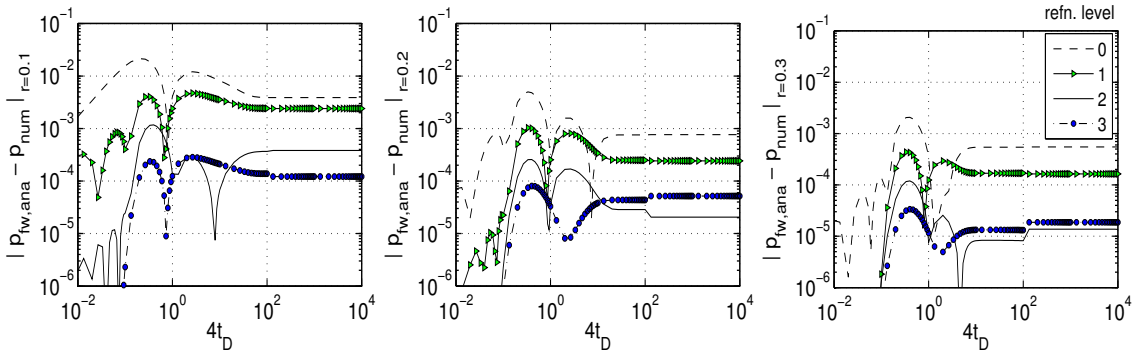

Figure 3.14: Absolute error in dimensionless boundary pressure. From left to right: $r_e = 0.1, 0.2, 0.3$.

We note that for late times ($4t_D > 10^5$), there is a loss in the accuracy of the finite element solution to the point source well problem. This is due to a lack in mass conservation as a result of rounding errors in Matlab. However it can easily be rectified for this case study. A detailed discussion is presented in Appendix A.5.

3.4.2 Error in second stage (finite radius well solution)

The local solution is computed in a radial domain using data measured from the previous section as the external boundary data. This problem satisfies the conditions stated in Section 3.1 which allow the finite radius well equations in (3.27) to be solved independently of θ. The coordinate transformation

$$r \to \ln r \stackrel{\text{def}}{=} R$$

is applied to the equations to get a refined grid near the wellbore. This transform converts the near-well logarithmic behaviour to a linear variation. Hence we have

the following equations:

$$\frac{\partial p_{\mathrm{fw}}}{\partial t} = e^{-2R}\,\frac{\partial^2 p_{\mathrm{fw}}}{\partial R^2}, \qquad R_w < R < R_e,\ t > 0, \tag{3.28a}$$

$$\frac{\partial p_{\mathrm{fw}}}{\partial R} = -Q, \qquad R = R_w,\ t > 0, \tag{3.28b}$$

$$p_{\mathrm{fw}}(R_e, t) = p_{\mathrm{ps}}(R_e, t), \qquad R = R_e,\ t > 0, \tag{3.28c}$$

$$p_{\mathrm{fw}}(R, 0) = 0, \qquad R_w < R < R_e, \tag{3.28d}$$

where $p_{\mathrm{ps}}(R_e, t)$ is the average pressure at radius R_e measured from the global solution. Space discretisation is performed using the vertex-centred finite volume method and time integration of the semi-discrete equations is by carried out using the ode15s routine in Matlab.

Figure 3.15 shows the absolute error in average dimensionless wellbore pressure for different refinements of the local mesh. The refinement level of the underlying FEM mesh on which the external boundary data is measured increases in each row from left to right, as indicated by N_t (number of triangles) in the plots. In each graph the maximum radial grid size $\Delta r_{\max}$ is refined by a factor of 4 from the initial value $\Delta r_{\max} = h$, where h is the average triangle size of the underlying FEM mesh calculated from

$$h = \sqrt{\frac{\text{domain area}}{\text{number of triangles}} \times \frac{4}{\sqrt{3}}}. \tag{3.29}$$

With $\Delta r_{\max}$ specified, the number of radial grid points N_r used for the simulation is calculated from

$$N_r = \text{ceil}\left[\frac{\ln(r_e/r_w)}{\ln(r_e/[r_e - \Delta r_{\max}])}\right]. \tag{3.30}$$

From Figure 3.15 we deduce that setting $\Delta r_{\max} = h$ results in maximum wellbore pressure and boundary pressure errors that are roughly within the same range. Also for $\Delta r_{\max} = h/4$ the maximum error in the wellbore pressure is less than the maximum error in the boundary pressure, while further refinement improves the accuracy of the wellbore simulation results only for very early time but does not lead to a noticeable reduction in the maximum error.

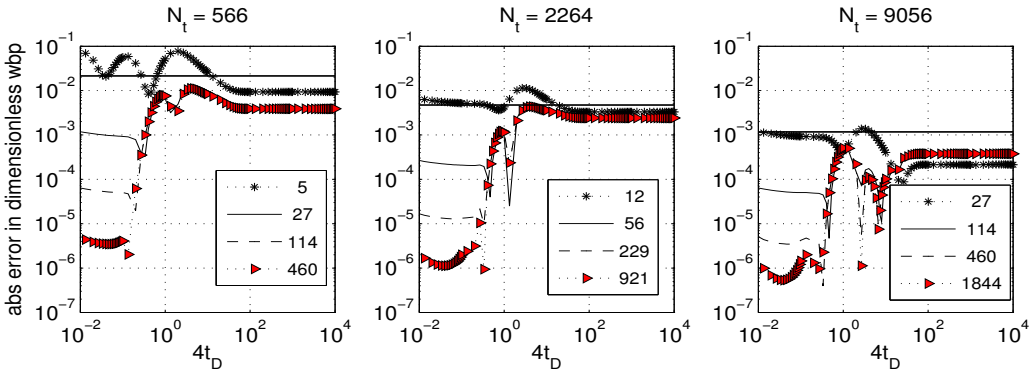

(a) $r_e = 0.1$

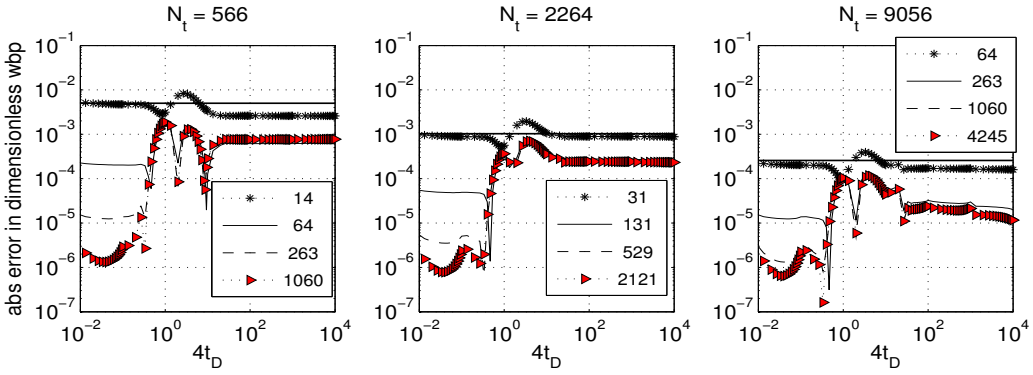

(b) $r_e = 0.2$

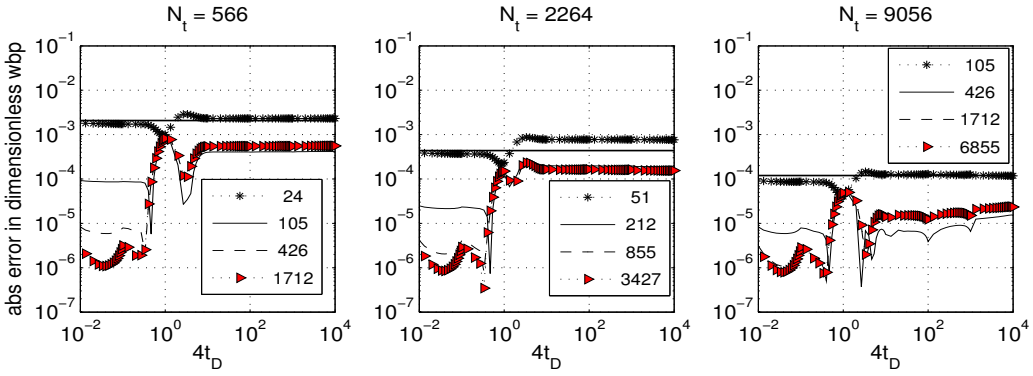

(c) $r_e = 0.3$

Figure 3.15: Absolute error in dimensionless wellbore pressure as radial grid is refined. The horizontal lines in each plot indicate the maximum error in the boundary data. N_t = number of triangles in underlying FEM mesh. Legend = N_r (number of radial grid points).

Figure 3.16 shows the absolute maximum error in dimensionless wellbore pressure plotted against number of radial grid points for $\Delta r_{\max} = h, h/2, h/4$. While there is a marked decrease in absolute error in refining from h to $h/2$, there is little gain in accuracy in refining further to $\Delta r_{\max} = h/4$. Comparison of the plots with the slope $= -2$ line indicates that the error has an $\mathcal{O}(h^2)$ convergence behaviour as the grid is refined. This will be proved theoretically in Section 3.5.

In Figure 3.17 the absolute maximum wellbore pressure error is plotted together with the absolute maximum boundary pressure error against the degrees of freedom (d.o.f) of the underlying FEM mesh. It can be seen that for $\Delta r_{\max}$ at least $h/2$, the error in the wellbore pressure is bounded above by the error in the boundary condition. Therefore as a guideline we propose that $\Delta r_{\max}$, the maximum radial grid spacing in the near-well simulation, should be set to $h/2$.

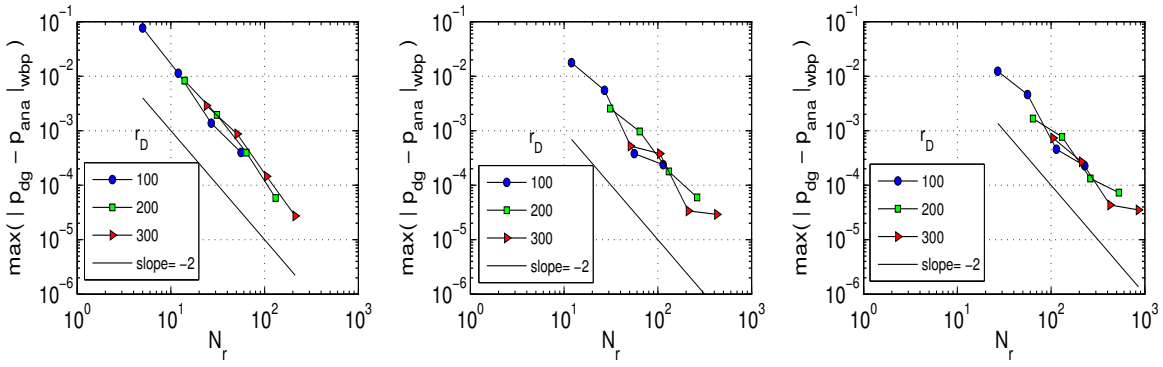

(a) $\Delta r_{\max} = h$ **(b)** $\Delta r_{\max} = \frac{h}{2}$ **(c)** $\Delta r_{\max} = \frac{h}{4}$

Figure 3.16: Absolute maximum error in dimensionless average wellbore pressure over time interval $4t_D \in [10^{-2}, 10^4]$.

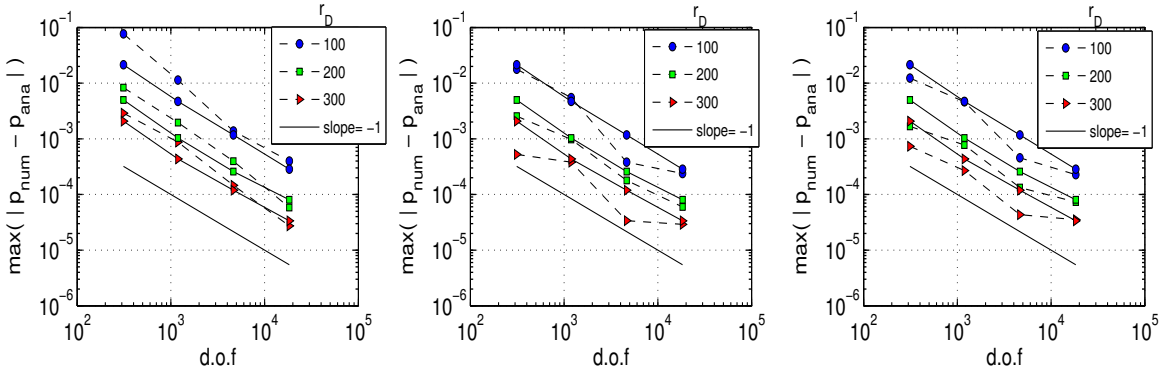

(a) $\Delta r_{\max} = h$ **(b)** $\Delta r_{\max} = \frac{h}{2}$ **(c)** $\Delta r_{\max} = \frac{h}{4}$

Figure 3.17: *Broken lines*: Maximum error in dimensionless wellbore pressure. *Solid lines*: Maximum error in dimensionless boundary pressure. The maximum error is measured over time interval $4t_D \in [10^{-2}, 10^4]$.

3.5 Theoretical error analysis

The numerical results in Figure 3.13 and Figure 3.16 indicate an $\mathcal{O}(h^2)$ convergence of the maximum absolute error in the average pressure measured at a fixed radius from the point source in the first stage simulations and at the wellbore in the second stage simulations respectively. In this section, theoretical error bounds for the maximum error in the first and second stage computations that support the observed convergence behaviour in the simulations are derived. In addition we show, by the strong maximum principle for parabolic problems, that the maximum error for the second stage computations occurs at the external boundary radius, and therefore the maximum error in average wellbore pressure is bounded above by the maximum error in average pressure at the external boundary radius.

3.5.1 Finite element error in first stage

The global solution in a homogeneous domain is obtained by solving the following equations:

$$\frac{\partial}{\partial t}p(\mathbf{x},t) - \nabla^2 p(\mathbf{x},t) = q\delta(\mathbf{x}-\mathbf{x}_0), \qquad \mathbf{x}\in\Omega,\ t>0, \tag{3.31a}$$

$$\nabla p(\mathbf{x},t)\cdot\mathbf{n} = 0, \qquad \mathbf{x}\in\partial\Omega,\ t>0, \tag{3.31b}$$

$$p(\mathbf{x},0) = 0, \qquad \mathbf{x}\in\Omega, \tag{3.31c}$$

where Ω is a bounded domain in $\mathbb{R}^2$. Let S_h^r denote a space of $\mathcal{C}^0$ piecewise polynomial functions of degree $r-1\geq 1$ on globally quasi-uniform partitions of Ω of mesh size h that fit the boundary exactly. The semi-discrete finite element approximation to (3.31) is:

Find $p_h(t) : \mathcal{C}^1(0,\infty) \to S_h^r$ which satisfies

$$(p_{h,t},\chi) + (\nabla p_h, \nabla\chi) = \chi(\mathbf{x}_0) \qquad \forall\chi\in S_h^r,\ t>0, \tag{3.32a}$$

$$\text{with } p_h(0) = 0 \quad \in S_h^r, \tag{3.32b}$$

where $(\cdot,\cdot)$ represents the $L_2(\Omega)$ inner product.

We wish to find error estimates $|(p-p_h)(\mathbf{x}^*,t^*)|$ at a fixed point away from

the point of singularity $\mathbf{x}_0$. Maximum norm error estimates for parabolic initial boundary value problems with Neumann boundary conditions have been studied by Schatz et al. [90] and Leykekhman [68]. However their results do not directly apply here, as will be explained subsequently. We will derive localised error estimates for (3.31) at a fixed distance from the point source by applying theorems by Schatz and Wahlbin [89] and Solo [93]. For a general reference see [99].

The studies by Schatz et al. [90] and Leykekhman [68] assume certain technical properties of the finite element space. Suffice it to say that S_h^r, the space of continuous piecewise polynomial functions defined earlier, satisfies these properties. The almost-best approximation in the maximum norm (that is, the best approximation in the maximum norm up to the constants C and $Cl_{h,r}$) was shown by Schatz et al. [90] to be:

$$\|p - p_h\|_{L_\infty(Q_T)} \leq C\|p_0 - p_{0h}\|_{L_\infty(\Omega)} + Cl_{h,r} \min_{\chi \in \mathcal{C}([0,T],S_h^r)} \|p - \chi\|_{L_\infty(Q_T)}, \quad (3.33)$$

where $Q_T = \Omega \times [0,T]$, $l_{h,r} = |\ln h|$ if $r = 2$, otherwise $l_{h,r} = 1$, p_0 is a non-zero initial condition, and $p_{0h} = P_h p_0$, the L_2 projection onto S_h^r, which is defined by $(P_h v, \chi) = (v, \chi), \forall \chi \in S_h^r$. Leykekhman [68] extended this result to the error at an arbitrary but fixed point $(\mathbf{x}^*, T), \mathbf{x}^* \in \Omega, T > 0$:

$$|(p - p_h)(\mathbf{x}^*, T)| \leq C(T) l_{h,s} \min_{\chi \in \mathcal{C}([0,T],S_h^r)} \|p - \chi\|_{L_\infty(Q_T),\sigma,s}, \quad (3.34)$$

given the initial data p_{0h}. In (3.34), $C(T)$ is a constant independent of p, p_h, h and $\mathbf{x}^*$, $l_{h,s} = 1$ if $s < r - 2$, $l_{h,s} = |\ln h|$ if $s = r - 2$ (where $0 \leq s \leq r - 2$, $r \geq 2$), and $\|\cdot\|_{L_\infty(Q_T),\sigma,s}$ is a weighted norm. For $r = 2$ (such as in (3.31)), this weighted norm is the same as $\|\cdot\|_{L_\infty(Q_T)}$.

The problem in applying (3.34) to obtain localised error estimates for (3.31) arises from the presence of a point source, symbolised by the delta function in (3.31a). From the approximation properties of the space S_h^r there exists a function $\chi \in S_h^r$ such that [17, p. 108]:

$$\|p - \chi\|_{L_\infty(\Omega)} \leq Ch^2 |p|_{W_\infty^2(\Omega)}. \quad (3.35)$$

$|\cdot|_{W^2_\infty(\Omega)}$ in (3.35) denotes the Sobolev space seminorm

$$|f|_{W^2_\infty(\Omega)} = \max_{|\alpha|=2} \|\partial^\alpha f\|_{L_\infty(\Omega)}, \tag{3.36}$$

where $\alpha = (\alpha_1, \alpha_2, \ldots, \alpha_n), \alpha_j \in \mathbb{N}$ is a multi-index, $|\alpha| = \alpha_1 + \alpha_2 + \cdots + \alpha_n$, and $\partial^\alpha f$ are all weak partial derivatives of f. Substituting (3.35) into (3.34) gives:

$$|(p - p_h)(\mathbf{x}^*, T)| \leq C(T)h^2 |\ln h| |p|_{W^2_\infty(Q_T)}. \tag{3.37}$$

However, $p \notin W^2_\infty(Q_T)$ from (3.31a), therefore (3.34) is not suitable for defining localised error bounds for (3.31).

To obtain localised error estimates for (3.31) at a fixed point away from the point of singularity, we rewrite p as the sum of a smooth function U and a Green's function $G^{\mathbf{x}_0}$, $p = U + G^{\mathbf{x}_0}$, where U and $G^{\mathbf{x}_0}$ satisfy the following equations:

$$\frac{\partial}{\partial t} U(\mathbf{x}, t) = \nabla^2 U(\mathbf{x}, t), \qquad \mathbf{x} \in \Omega, t > 0, \tag{3.38a}$$

$$\nabla U(\mathbf{x}, t) \cdot \mathbf{n} = 0, \qquad \mathbf{x} \in \partial\Omega, t > 0, \tag{3.38b}$$

$$U(\mathbf{x}, 0) = -G^{\mathbf{x}_0}(\mathbf{x}), \qquad \mathbf{x}, \mathbf{x}_0 \in \Omega, \tag{3.38c}$$

and

$$-\nabla^2 G^{\mathbf{x}_0}(\mathbf{x}) = q\delta(\mathbf{x} - \mathbf{x}_0), \qquad \mathbf{x}, \mathbf{x}_0 \in \Omega, \tag{3.39a}$$

$$\nabla G^{\mathbf{x}_0}(\mathbf{x}) \cdot \mathbf{n} = 0, \qquad \mathbf{x} \in \partial\Omega, \mathbf{x}_0 \in \Omega. \tag{3.39b}$$

The semi-discrete finite element approximation to p is $p_h(t) = U_h(t) + G_h^{\mathbf{x}_0}$ where

$$(U_{h,t}, \chi) + (\nabla U_h, \nabla \chi) = 0 \qquad \forall \chi \in S_h^r(\Omega), t > 0, \tag{3.40a}$$

$$U_h(0) = -G_h^{\mathbf{x}_0}, \tag{3.40b}$$

and

$$(\nabla G_h^{\mathbf{x}_0}, \nabla \chi) = \chi(\mathbf{x}_0) \qquad \forall \chi \in S_h^r(\Omega). \tag{3.41}$$

So

$$\begin{aligned} |(p-p_h)(\mathbf{x}^*,t^*)| &= |(U-U_h)(\mathbf{x}^*,t^*) + (G^{\mathbf{x}_0} - G_h^{\mathbf{x}_0})(\mathbf{x}^*)|, \\ &\leq |(U-U_h)(\mathbf{x}^*,t^*)| + |(G^{\mathbf{x}_0} - G_h^{\mathbf{x}_0})(\mathbf{x}^*)| \,. \end{aligned} \tag{3.42}$$

We consider $|(U-U_h)(\mathbf{x}^*,t^*)|$ and $|(G^{\mathbf{x}_0} - G_h^{\mathbf{x}_0})(\mathbf{x}^*)|$ independently by applying theorems by Solo [93] and Schatz and Wahlbin [89] respectively. These theorems are concisely stated below for completeness.

Localised interior estimate for parabolic problems [93]

Let Ω be a bounded domain in $\mathbb{R}^N$, $Q = \Omega \times [0,T]$, and $\partial Q = \partial\Omega \times [0,T]$. Given the problem

$$\frac{\partial u}{\partial t} - \nabla^2 u = 0 \qquad \text{in } Q, \tag{3.43a}$$

$$\mathbf{n} \cdot \nabla u = g \qquad \text{on } \partial Q, \tag{3.43b}$$

$$u(t=0) = u_0 \qquad \text{in } \Omega, \tag{3.43c}$$

where both g and u_0 in general have low regularity ($u_0 \in W_q^{-s}(\Omega), g \in W_q^{-k,-l}(\partial Q)$ for arbitrary s, k, l, and q), and its semi-discrete finite element approximation:

Find $u_h(t) \in \mathcal{C}^0([0,T], S_h^r)$ such that

$$(u_{h,t}, \chi)_\Omega + (\nabla u_h, \nabla\chi)_\Omega = \langle g, \chi\rangle_{\partial\Omega} \qquad \forall \chi \in S_h^r \text{ and a.e in } [0,T], \tag{3.44a}$$

$$u_h(0) = P_h u_0, \tag{3.44b}$$

where $P_h f$ is the L_2 projection onto S_h^r, and $\langle\cdot,\cdot\rangle$ denotes the pairing of a linear space with its dual, then the following theorem holds.

Theorem 3.1. *Assume S_h^r satisfies the required technical properties of the finite element space stated in [93] and that the triangulations fit the boundary exactly. Then for u and u_h defined above, if $x^* \in \Omega$, dist($x^*, \partial\Omega$)$> d$ and $t^* > d^2$ for $d > ch$, the following estimate holds for any l and $k = 0, 1$:*

$$|(u-u_h)(x^*,t^*)| \leq C_{l,d} h^{r-k} \big(\|u_0\|_{W_1^{-k}(\Omega)} + \|g\|_{W_1^{-k-l}(\partial Q)} \big) \tag{3.45}$$

where $C_{l,d} = \log(1/d)d^{-N-r-2l}$.

Pointwise interior error estimates for the Green's function near the singularity [89]

Let Ω be a bounded domain in $\mathbb{R}^N$ with smooth boundary $\partial\Omega$, and A a bilinear form of type

$$A(u,v) = \int_\Omega \left(\sum_{i,j=1}^{N} a_{ij}(x) \frac{\partial u}{\partial x_i} \frac{\partial v}{\partial x_j} + \sum_{i=1}^{N} b_i(x) \frac{\partial u}{\partial x_i} v + d(x)uv \right) dx, \tag{3.46}$$

where A is coercive over H^1, that is, there exists a constant $c > 0$ such that

$$c\|u\|^2_{H^1(\Omega)} \leq A(u,u) \qquad \forall u \in H^1(\Omega). \tag{3.47}$$

Let $S_h(\Omega)$ be a one-parameter family of subspaces of $W^1_\infty(\Omega)$ that satisfy

$$\inf_{\chi \in S_h(\Omega)} \|u - \chi\|_{H^1(\Omega)} \leq Ch^{l-1}\|u\|_{H^l(\Omega)} \qquad \text{for } 1 \leq l \leq r. \tag{3.48}$$

Furthermore assume that S_h satisfies the required technical properties of the finite element space as stated in [89].

Let $x_0 \in \Omega$, and $G^{x_0}(x), G^{x_0}_h(x)$ be the Green's function and approximate Green's function respectively which satisfy:

$$A(G^{x_0}, u) = u(x_0) \qquad \forall u \in W^1_\infty(\Omega), \tag{3.49}$$

$$\text{and} \qquad A(G^{x_0}_h, \chi) = \chi(x_0) \qquad \forall \chi \in S_h(\Omega). \tag{3.50}$$

Then the following theorem holds.

Theorem 3.2. *Given the assumptions above, let $\Omega_1 \subset\subset \Omega_2 \subset\subset \Omega$. There there exist constants C and C_2 so that if h is sufficiently small, then for $x_0 \in \Omega_1$ and $x \in \Omega_2$*

$$\text{If } |x-x_0| \geq C_2 h, \quad |(G^{x_0} - G_h^{x_0})(x)| \leq \frac{Ch^r}{|x-x_0|^{N+r-2}} \left(\ln \frac{|x-x_0|}{h} \right)^{\alpha} \tag{3.51}$$

$$\text{If } 0 \leq |x-x_0| \leq C_2 h, \quad |(G^{x_0} - G_h^{x_0})(x)| \leq C \begin{cases} \ln \frac{1}{|x-x_0|} + 1 & \text{for } N = 2 \\ \ln \frac{1}{|x-x_0|^{N-2}} & \text{for } N \geq 2 \end{cases} \tag{3.52}$$

where r is the optimal order of h, and $\alpha = 1$ for $r = 2$, $\alpha = 0$ for $r \geq 3$.

We note here that S_h^r, the space of continuous piecewise polynomial functions in (3.32), satisfies the necessary properties required by Theorem 3.1 and Theorem 3.2. ($\Omega_1 \subset\subset \Omega$ means that the closure of Ω_1 is in the interior of Ω.)

Applying Theorem 3.1 for $l = 0, k = 0, r = 2, N = 2$, the following error estimate is obtained for U (see (3.38)):

$$|(U - U_h)(\mathbf{x}^*, t^*)| \leq \log(1/d) d^{-4} h^2 \|G^{\mathbf{x}_0}(\mathbf{x})\|_{L_1(\Omega)} \tag{3.53}$$

$$\leq C_1 \log(1/d) d^{-4} h^2 \tag{3.54}$$

since the L_1 norm of $G^{\mathbf{x}_0}(\mathbf{x})$ is bounded.

Applying Theorem 3.2 for $N = 2, r = 2$, the following error estimate is obtained for $G^{\mathbf{x}_0}$ (see (3.39)):

$$|(G^{\mathbf{x}_0} - G_h^{\mathbf{x}_0})(\mathbf{x}^*)| \leq C_2 h^2 \left(\ln \frac{|\mathbf{x} - \mathbf{x}_0|}{h} \right) |\mathbf{x} - \mathbf{x}_0|^{-2} . \tag{3.55}$$

So from (3.42), (3.54) and (3.55),

$$|(p - p_h)(\mathbf{x}^*, t^*)| \leq h^2 \left[C_1 \log(1/d) d^{-4} + C_2 \left(\ln \frac{|\mathbf{x} - \mathbf{x}_0|}{h} \right) |\mathbf{x} - \mathbf{x}_0|^{-2} \right] \tag{3.56a}$$

$$\leq h^2 (C_U + C_{G^{\mathbf{x}_0}}) . \tag{3.56b}$$

(3.56) gives the pointwise error estimate for (3.31). It predicts $\mathcal{O}(h^2)$ behaviour subject to C_U and $C_{G^{\mathbf{x}_0}}$. The form of the constant $C_{G^{\mathbf{x}_0}}$ implies that the pointwise error is worse when measurements are made close to the point

source. The form of the constant C_U suggests that the pointwise error is worse for measurements taken close to the domain boundary. Since the pointwise error is $\mathcal{O}(h^2)$ at time t^*, the average error at a radius r_e away from the point source is also $\mathcal{O}(h^2)$ at t^*. Furthermore the maximum error of the average pressure at the radius r_e over the simulation time is also $\mathcal{O}(h^2)$. This supports the observed results in Section 3.4.1.

To further investigate (3.56), simulations were carried out in a square of side 1 with a point source at the centre of the square at (0.5,0.5). Measurements are taken at fixed points: $x - x_0 = 0.05, 0.1, 0.2, 0.4, 0.49$, and $y = 0.5, y = x$ ((x_0, y_0) is the point source location). In addition average measurements are taken at fixed radii $r = 0.1, 0.2, 0.4$ from the point source. The absolute maximum error in these measurements over the entire simulation time and at fixed times t^* is plotted in Figure 3.18. Firstly, it can be seen that for (3.31) C_U gives a particularly pessimistic error bound that is not observed in the numerical results for measurements taken close to the domain boundary. The error bound is pessimistic because Theorem 3.1 covers a more general problem with low regularity Neumann boundary data, whereas the global problem in this section has smooth Neumann boundary data. On the other hand the error is worse for measurements closer to the singularity as predicted by $C_{G^{x_0}}$. Secondly, the plots show that the maximum absolute error taken over the entire simulation time has a stronger $\mathcal{O}(h^2)$ behaviour compared to the error at the fixed point in time t^*. In Figure 3.18 (c)–(f) we see a sharp dip or rise in the maximum absolute error for some plots. This is most likely a numerical artefact where an unforeseen cancellation or pollution of the error occurs.

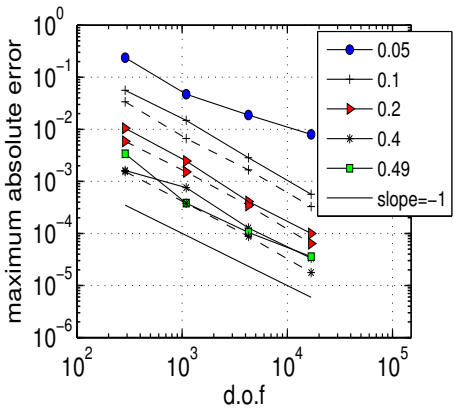

(a) Absolute maximum error over time interval $t \in [0.25 \times 10^{-6}, 25]$. $y = 0.5$.

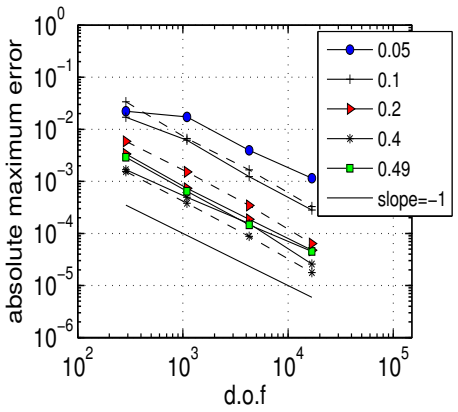

(b) Absolute maximum error over time interval $t \in [0.25 \times 10^{-6}, 25]$. $y = x$.

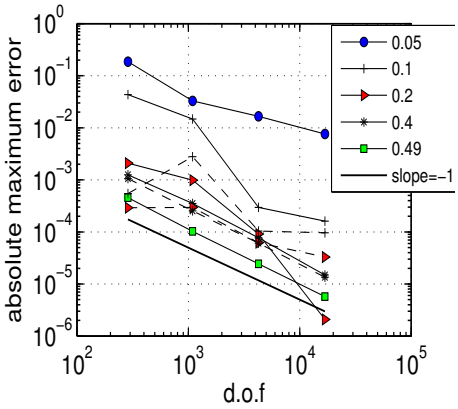

(c) Absolute maximum error at $t^* = 0.0103$. $y = 0.5$.

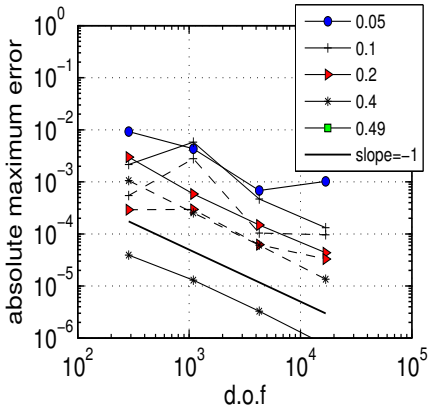

(d) Absolute maximum error at $t^* = 0.0103$. $y = x$.

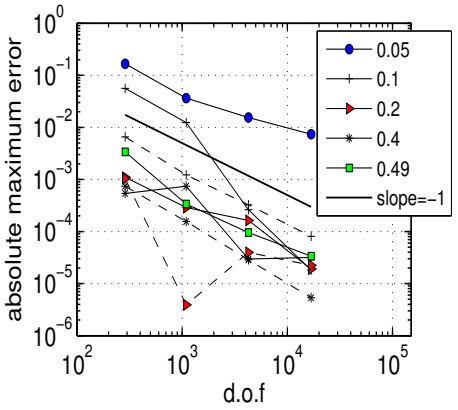

(e) Absolute maximum error at $t^* = 0.1231$. $y = 0.5$.

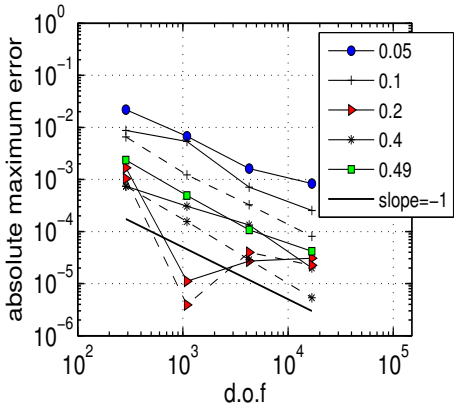

(f) Absolute maximum error at $t^* = 0.1231$. $y = x$.

Figure 3.18: Absolute maximum error at fixed points (solid lines) and fixed radii (broken lines). Legend represents fixed radius for broken lines or distance in the x-direction from the point source for solid lines.

3.5.2 Finite volume error in second stage

The solution in the local post-process domain is obtained by solving (3.28), which is stated again below:

$$\frac{\partial p}{\partial t} = e^{-2R}\,\frac{\partial^2 p}{\partial R^2}, \qquad R_w < R < R_e, t > 0, \tag{3.57a}$$

$$\frac{\partial p}{\partial R} = -Q, \qquad R = R_w, t > 0, \tag{3.57b}$$

$$p(R_e, t) = p_{\mathrm{ps}}(R_e, t) = p_e(t), \qquad R = R_e, t > 0, \tag{3.57c}$$

$$p(R, 0) = 0, \qquad R_w < R < R_e. \tag{3.57d}$$

Let p_h be the semi-discrete approximation to p on a grid Ω_h, and u the restriction of p to Ω_h. Then we have

$$\frac{dp_h}{dt} = Ap_h + f, \tag{3.58}$$

$$\frac{du}{dt} = Au + f + \sigma_h(t), \tag{3.59}$$

where $\sigma_h(t)$ is the local truncation error. The error in the spatial discretisation is $\varepsilon(t) = u(t) - p_h(t)$. We show below that the pointwise error at the wellbore has $\mathcal{O}(h^2)$ convergence for the vertex-centred finite volume method implemented in Section 3.4.2.

Expanding the semi-discrete approximation (3.58) for (3.57) using the vertex-centred finite volume method, we have, for uniform mesh size h,

$$e^{2R_1} p'_{h,1}(t) = \frac{2}{h^2}\Big(-p_{h,1}(t) + p_{h,2}(t)\Big) + \frac{2}{h}\big(-Q\big), \tag{3.60a}$$

$$e^{2R_k} p'_{h,k}(t) = \frac{1}{h^2}\Big(p_{h,k-1}(t) - 2p_{h,k}(t) + p_{h,k+1}(t)\Big), \quad 2 \le k \le m-2 \tag{3.60b}$$

$$e^{2R_{m-1}} p'_{h,m-1}(t) = \frac{1}{h^2}\Big(p_{h,m-2}(t) - 2p_{h,m-1}(t)\Big) + \frac{1}{h^2} p_e(t). \tag{3.60c}$$

The truncation error $\sigma_h(t)$ is $\mathcal{O}(h^2)$ at all points except at $k = 1$ where

$$\sigma_{h,1}(t) = \frac{1}{3} h u_{RRR}(R_w, t) + \mathcal{O}(h^2). \tag{3.61}$$

Despite this $\mathcal{O}(h^2)$ convergence of the spatial discretisation error $\varepsilon(t)$ at all points can be shown using the theorem by Hundsdorfer and Verwer [62, Theorem 5.2, p.85] on refined global error estimates. This theorem is stated below.

Theorem 3.3. *Consider the linear semi-discrete system*

$$w'(t) = Aw(t) + f(t) \tag{3.62}$$

where A is an $m \times m$ matrix and $f(t) \in \mathbb{R}^m$ represents a source term and boundary conditions in the PDE, and assume that the stability condition

$$\|e^{tA}\| \leq K e^{\alpha t} \qquad \text{for } 0 \leq t \leq T \tag{3.63}$$

holds on all grids Ω_h, where the constants $K \geq 1$ and $\alpha \in \mathbb{R}$ are both independent of h. Suppose that for $0 \leq t \leq T$ we can decompose the truncation error $\sigma_h(t)$ as

$$\sigma_h(t) = A\xi(t) + \eta(t) \qquad \text{with} \quad \|\xi(t)\|, \|\xi'(t)\|, \|\eta(t)\| \leq Ch^r \tag{3.64}$$

and suppose that $\|\varepsilon(0)\| \leq C_0 h^r$, where $C, C_0 > 0$ are constants, and $\varepsilon(t)$ is the spatial discretisation error. Then we have convergence of order r with the error bounds

$$\|\varepsilon(t)\| \leq \begin{cases} KC_0 e^{\alpha t} h^r + \left(1 + Ke^{\alpha t} + \frac{2K}{\alpha}(e^{\alpha t} - 1)\right) Ch^r & \text{if } \alpha \neq 0,\ 0 \leq t \leq T \\ KC_0 h^r + (1 + K + 2Kt)Ch^r & \text{if } \alpha = 0,\ 0 \leq t \leq T \end{cases} \tag{3.65}$$

where $\|\cdot\|$ is the discrete L_p–norm.

To apply Theorem 3.3, we need to show the stability condition (3.63) for the semi-discrete system (3.60), and that the truncation error for this system satisfies (3.64). To prove the stability condition in the infinity norm we apply the following theorem by Hundsdorfer and Verwer [62, Theorem 2.4, p.32].

Theorem 3.4. *Let $A \in \mathbb{C}^{m\times m}$ and $\alpha \in \mathbb{R}$. We have*

$$\mu(A) \leq \alpha \quad \Longleftrightarrow \quad \|e^{tA}\| \leq e^{t\alpha} \qquad \forall\, t \geq 0 \tag{3.66}$$

where $\mu(A)$ is the logarithmic matrix norm and $\|\cdot\|$ is the discrete L_p–norm.

The logarithmic matrix infinity norm of A is defined as [62]

$$\mu_\infty(A) = \max_i \left(\text{Re } a_{ii} + \sum_{j\neq i} |a_{ij}| \right). \tag{3.67}$$

So for (3.60) we have $\mu_\infty(A) = 0$ which implies, from Theorem 3.4, that $\|e^{tA}\| \leq 1$.

Next we need to write the truncation error in the form $\sigma_h = A\xi(t) + \eta(t)$ (see (3.64)). Ignoring $\eta(t)$ which represents the $\mathcal{O}(h^2)$ terms in the truncation error and putting $\sigma_h = A\xi(t)$ gives, from (3.60) and (3.61),

$$\xi_1 - \xi_2 = C_1 h^3 \tag{3.68a}$$

$$\xi_{k-1} - 2\xi_k + \xi_{k+1} = 0 \tag{3.68b}$$

$$\xi_{m-2} - 2\xi_{m-1} = 0 \tag{3.68c}$$

where $C_1 = u_{RRR}(R_w, t)/6$. Solving (3.68b) with the ansatz $\xi = ar^n$ gives $r = 1$ twice so that $\xi_n = a + bn$. Applying the boundary conditions (3.68a) and (3.68c) gives $\xi_k = C(m-k)h^3$; therefore $\xi_k \leq Cmh^3 = Ch^2$ (since $h = 1/m$). So $\|\xi(t)\|_\infty, \|\xi'(t)\|_\infty, \|\eta(t)\|_\infty \leq Ch^2$. Since $\varepsilon(0) = 0$, we set $C_0 = 2C$ so that Theorem 3.3 gives

$$\|\varepsilon(t)\|_\infty \leq 2(2+t)Ch^2. \tag{3.69}$$

Therefore

$$|\varepsilon_k(t)| \leq \|\varepsilon(t)\|_\infty \leq 2(2+t)Ch^2, \tag{3.70}$$

and the pointwise error has $\mathcal{O}(h^2)$ convergence at $R = R_w$ (that is, $k = 1$). Since the pointwise error is $\mathcal{O}(h^2)$ at R_w, the error in the average pressure at R_w is also $\mathcal{O}(h^2)$. Furthermore the maximum error in the average pressure at R_w over the simulation time is also $\mathcal{O}(h^2)$. This supports the observed results in Section 3.4.2.

3.5.3 Wellbore error bounded by external boundary error

Define the modelling error $\beta(r,t) = \upsilon(r,t) - p_{\text{fw}}(r,t)$, where $p_{\text{fw}}(r,t)$ is the solution to (3.28) (which has the external boundary condition taken from a point source well solution), and $\upsilon(r,t)$ is the solution to (3.28) with the external boundary condition due to a finite radius well. Then for $(k, \mu, h, c_t, \phi) = 1$ this error satisfies:

$$\frac{\partial \beta}{\partial t} = \frac{1}{r}\frac{\partial}{\partial r}\left(r\frac{\partial \beta}{\partial r}\right), \qquad r_w < r < r_e, \tag{3.71a}$$

$$\frac{\partial \beta}{\partial r}(r_w, t) = 0, \tag{3.71b}$$

$$\beta(r_e, t) = \beta_e(t), \tag{3.71c}$$

$$\beta(r, 0) = 0. \tag{3.71d}$$

According to the maximum principle, the maximum of the solution $\beta(r,t)$ can only occur at r_w, r_e or $t = 0$. However $\beta(r,0) = 0$, so the maximum cannot occur here. The strong maximum principle stated below is used to show that the maximum must occur at r_e.

Theorem 3.5. (Strong maximum principle for parabolic problems [94, p. 21]) *Let u be a non-constant solution of*

$$Lu - \frac{\partial u}{\partial t} = \sum_{i,j=1}^{N} a_{ij}(x,t)\frac{\partial^2 u}{\partial x_i \partial x_j} + \sum_{i=1}^{N} b_i(x,t)\frac{\partial u}{\partial x_i} - \frac{\partial u}{\partial t} \geq 0 \quad \text{in } \Omega \times (0,T)$$

where Ω is a finite domain in the n-dimensional Euclidean space E^N, $T < \infty$, and L a uniformly bounded elliptic operator with bounded coefficients a_{ij} and b_i. If u attains its maximum M at some point x_M of $\partial\Omega \times (0,T)$, where $\partial\Omega$ has the interior sphere property, any derivative in an outward direction v from Ω satisfies $\dfrac{\partial u}{\partial v} > 0$ at x_M.

The interior sphere property at a point x_M of $\partial\Omega$ states that there must be a sphere S of some radius $r_0 > 0$ contained in Ω such that $S \cap \partial\Omega = \{x_M\}$.

Applying Theorem 3.5, (3.71b) violates the strong maximum principle so the maximum cannot occur here. Therefore the maximum must occur at r_e, and

$$\beta(t) \leq \max \beta_e(t). \tag{3.72}$$

As shown in Figure 3.17, the numerical results follow the theoretical prediction in (3.72) for $\Delta r_{\max} \leq \frac{h}{2}$.

3.6 Finite volume discretisation of first stage

In this section the first stage computations are carried out on rectangular mesh elements using the cell-centred finite volume method. This test is carried out because rectangular mesh elements together with finite volume or finite difference discretisation methods are commonly used in commercial reservoir simulators. Domain parameters are in Table 3.2. An equal number of mesh elements is defined along the length and width of the square domain so that the discretisation simplifies to a central-difference approximation in space. For each refinement level the point source well is exactly at the centre of the control volume. Time integration as before is performed using the Matlab stiff solver `ode15s`.

The maximum absolute error results are shown in Figure 3.19, and are similar to the results in Figure 3.17 obtained for finite element spatial discretisation in the first stage computations. As before the maximum absolute error in the dimensionless average wellbore and boundary pressures for the second stage simulations show $\mathcal{O}(h^2)$ convergence. In addition the error in the wellbore pressure is bounded above by the error in the boundary pressure for $\Delta r_{\max} \leq h/2$, where h is the length of a mesh element.

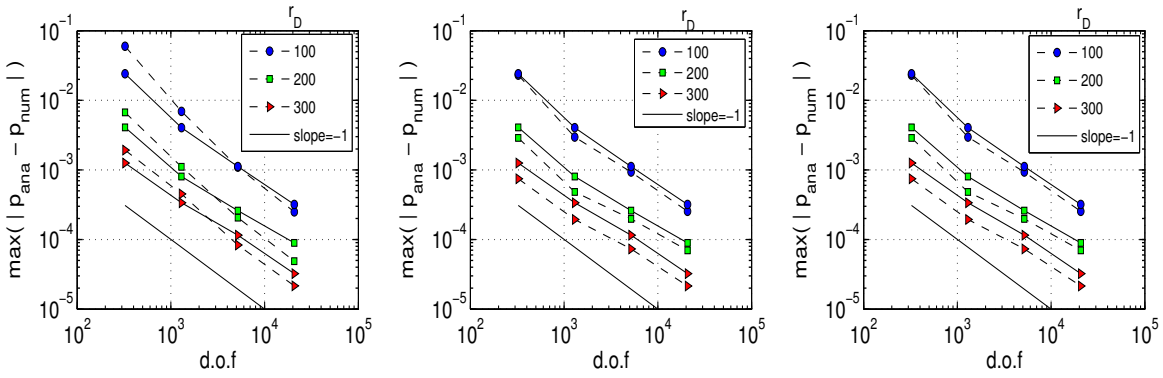

(a) $\Delta r_{\max} = h$ **(b)** $\Delta r_{\max} = \dfrac{h}{2}$ **(c)** $\Delta r_{\max} = \dfrac{h}{4}$

Figure 3.19: *Broken lines*: Maximum error in dimensionless wellbore pressure. *Solid lines*: Maximum error in dimensionless boundary pressure. Maximum taken over time interval $4t_D \in [10^{-2}, 10^4]$.

In Figure 3.20 and Figure 3.21 the absolute error in dimensionless well pressure calculated from the Peaceman well index is plotted for comparison. The Peaceman well index was discussed in Section 2.2.1 as a way to relate steady-state wellblock pressure to wellbore pressure. The well index in this problem is calculated from:

$$\mathrm{WI} = \frac{2\pi kH}{\ln \dfrac{r_{\mathrm{eq}}}{r_w}} \tag{3.73}$$

where for steady-state the equivalent radius r_{eq} is

$$r_{\mathrm{eq}} = 0.14\sqrt{2}\,\Delta x\ , \quad \Delta x = \Delta y. \tag{3.74}$$

Peaceman [82] also proposed the following transient equivalent radius for unsteady-state:

$$r_{\mathrm{eq}} = \Delta x \sqrt{4t_D \left(\frac{r_w}{\Delta x}\right)^2 \exp\left(-\gamma - \frac{4\pi kH}{q\mu} p\right)} \tag{3.75}$$

where $t_D = \eta t / r_w^2$ and $\Delta x = \Delta y$.

The Peaceman solutions are calculated from the same global solutions generated for the decoupled overlapping grids computation. Figure 3.20 clearly shows that the decoupled overlapping grids method performs significantly better than the Peaceman well index solutions. The accuracy of the wellbore pressure from the decoupled overlapping grids method improves with grid refinement, whereas

this is not the case for the solution using the Peaceman well index. The plots show that the absolute error reaches its peak during an initial transient phase before settling at a steady-state value.

The maximum absolute error for the results in Figure 3.20 is plotted in Figure 3.21. It shows more clearly the improvement in accuracy with grid refinement of the wellbore pressure calculated by decoupled overlapping grids method compared with those calculated using the Peaceman well index methods.

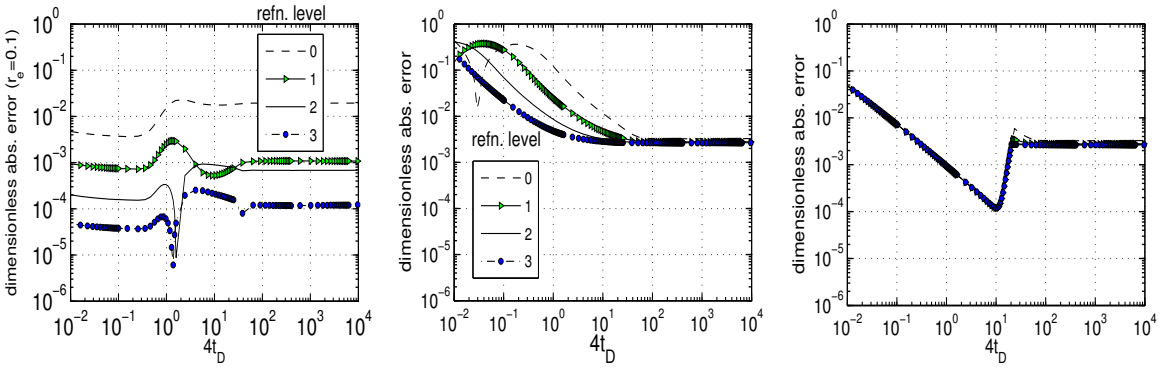

(a) Solution using decoupled overlapping grids method with $\Delta r_{\max} = \dfrac{h}{2}$.

(b) Solution from steady-state Peaceman well index.

(c) Solution from unsteady-state Peaceman well index.

Figure 3.20: Comparison of dimensionless absolute error in wellbore pressure from decoupled grids and using Peaceman well index. $r_e = 0.1$.

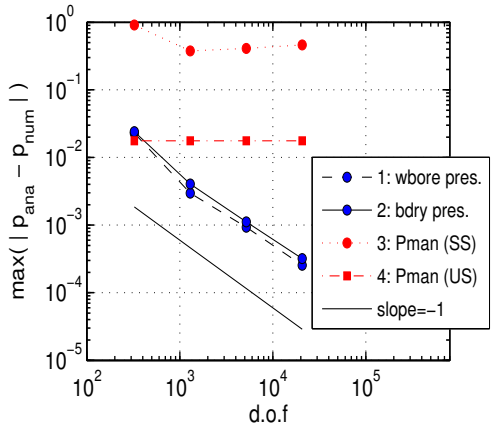

Figure 3.21: Comparison of maximum error in wellbore pressure from decoupled grids and using Peaceman well index. In Legend, 1: wellbore pressure (decoupled overlapping grids); 2: local domain external boundary pressure; 3: Peaceman steady-state well index; 4: Peaceman unsteady-state well index. Maximum taken over time interval $4t_D \in [10^{-2}, 10^4]$.

3.7 Comparison with solutions on locally refined mesh

In this section the average wellbore pressure from the decoupled overlapping grids method is compared to results for a finite radius, interior boundary wellbore that is fully resolved in the global computational domain by local grid refinement (LGR).

3.7.1 Locally refined finite element mesh

Here full resolution of the finite radius well is achieved through local refinement of a finite element mesh. This is implemented using the Comsol Multiphysics[28] a finite element software.

A comparison of the results from both methods is shown in Figure 3.22. Table 3.3 contains the mesh properties for the simulations. From Figure 3.22 and Table 3.3, it is seen that the method of decoupled overlapping grids gives good results for less computational effort (fewer degrees of freedom) compared to local grid refinement for linear Lagrange elements. This is clearly shown by maximum absolute error plot in Figure 3.22(c). The accuracy of the LGR finite element

solution can be improved by using quadratic Lagrange elements instead of linear elements, as shown in Figure 3.22(b). However the use of quadratic Lagrange elements for a well test study could potentially become highly computationally intensive. For instance a change in well position will require a regeneration of the mesh in the entire simulation domain for a wellbore resolved by local grid refinement. On the other hand for the decoupled overlapping grids method only the position of the point source need be changed in the global problem, together with a possible regeneration of the mesh on a significantly smaller local region surrounding the wellbore for the post-process stage.

Refn. level	N_v	N_t	N_r	*d.o.f.*
	Figure 3.22(a)			
0	312	566	12	324
1	1189	2264	27	1216
2	4641	9056	56	4697
3	18337	36224	114	18451
	Figure 3.22(b)			
Lin. elements : 0	919	1762		
: 1	3600	7048		$N_v = d.o.f.$
: 2	14248	28192		
Quad. elements	14248	7048		

Table 3.3: Mesh properties for Figure 3.22. N_v =number of vertices, N_t =number of triangles, N_r =number of radial grid points.

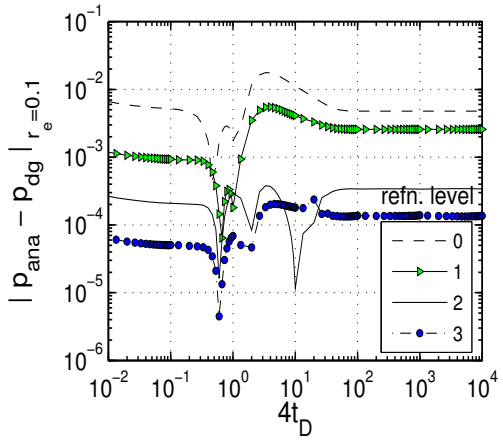

(a) Solution using decoupled overlapping grids method with $\Delta r_{\max} = \frac{h}{2}$.

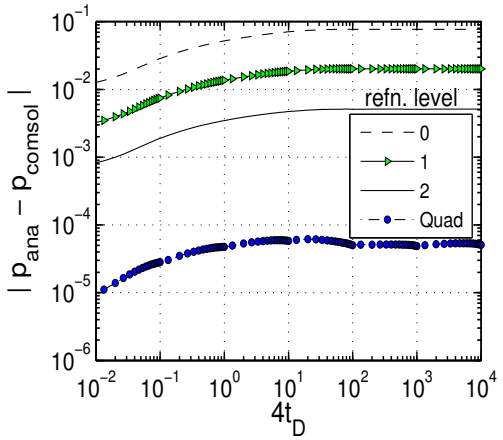

(b) Solution from Comsol (LGR). Refinement levels are for linear Lagrange elements.

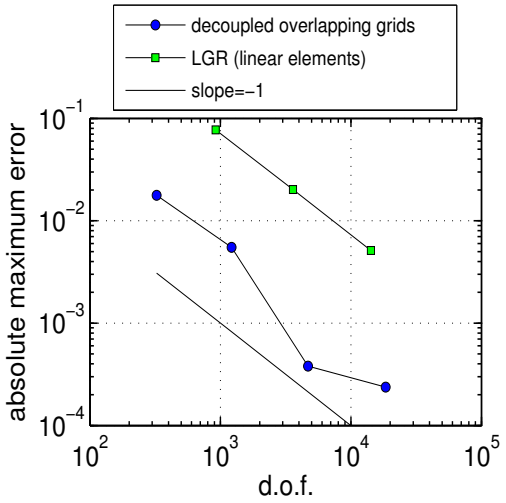

(c) Maximum absolute error for over time interval $4t_D \in [10^{-2}, 10^4]$.

Figure 3.22: Absolute error in dimensionless average wellbore pressure for $r_e = 0.1$ (see Table 3.3).

3.7.2 Hybrid grid

The hybrid grid implemented in this section was proposed by Pedrosa and Aziz [85], and has been used, for example, in [31, 56, 102]. The hybrid grid is composed of a polar grid in the near-well region and a rectangular grid away from the well. The two regions are connected by irregularly shaped blocks. A schematic of the grid system is shown in Figure 3.23.

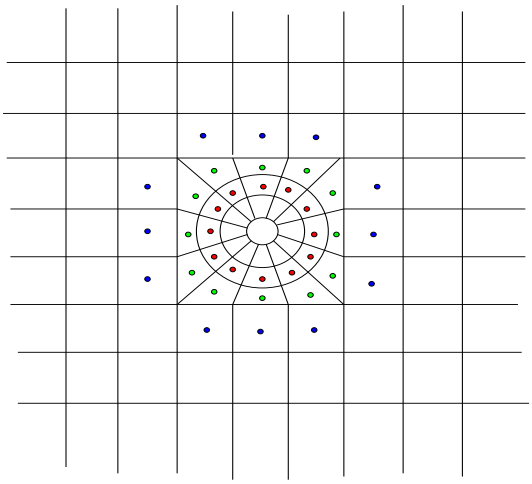

Figure 3.23: Schematic of hybrid grid

The irregular blocks are bordered by polar and rectangular grids. To determine the transmissibility at the polar-irregular block interface, an apparent exterior radius is computed such that the resulting polar block has the same area as the irregular block, that is,

$$r_{\text{app},j} = \sqrt{\frac{2A_{\text{irr},j}}{\Delta\theta_j} + r_e^2} \tag{3.76}$$

where r_e is the external radius of the polar region. This apparent radius is then used to calculate the radial transmissibility. Likewise at the rectangular-irregular block interface, an apparent length is computed so that the resulting rectangular block has the same area as the irregular block, for example,

$$L_j = \frac{A_{\text{irr},ij}}{\Delta x_i} \, . \tag{3.77}$$

This apparent length is used then to compute the transmissibility. To determine

the angular transmissibility of the irregular block, a similar procedure is adopted. An apparent radius is computed for the 2 adjacent irregular blocks such that the total area of the 2 apparent radial blocks is equal to the total area of the adjacent irregular blocks. So (3.76) is used with $A_{\text{irr},j}$ replaced by $A_{\text{irr},j} + A_{\text{irr},j+1}$ and $\Delta\theta_j$ by $\Delta\theta_j + \Delta\theta_{j+1}$. The angular transmissibility is then computed using the new radius and the angles of the irregular blocks.

The Jacobian matrix structure for a sample grid is shown in Figure 3.24. The matrix is constructed starting with the entries for the polar gridblocks (`pp`), followed by entries for the irregular gridblocks (`ii`) and finally entries for the rectangular gridblocks `rr`. The entries at the interface of the regions are indicated in the diagram.

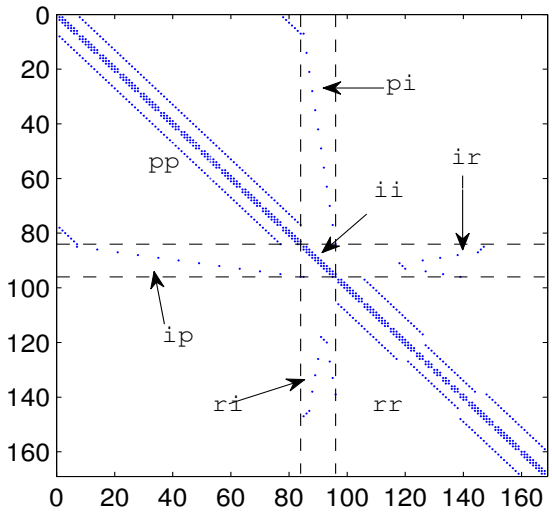

Figure 3.24: Jacobian matrix structure for a sample grid showing the entries for different regions. `p`=polar, `i`=irregular, `r`=rectangular.

Results from the hybrid grid simulation are compared against results from the decoupled overlapping grids method with the first stage solved on a finite volume mesh (see Section 3.6). The simulations are carried out in a square of size 1 with the well at the centre of the square. The cell spacing Δx and $\Delta r_{\max}$ for the hybrid grid are equal to the values for the first and second stages of the decoupled overlapping grids simulation respectively. Given the external radius r_e, the inset that contains the polar grid in the hybrid implementation is the smallest square that contains a circle of this radius. The external radius is then adjusted

so that the shortest perpendicular distance is at most $\frac{1}{2}\Delta x$ from the rectangular grid. Logarithmic spacing is applied along the r–direction in the polar region of the hybrid grid to get a refined grid near the wellbore. Table 3.4 shows the mesh properties of the simulations. The external radius r_e and well radius r_w are 0.1 and 10^{-3} respectively for the hybrid and decoupled overlapping grid simulations.

		Decoupled overlapping grids			Hybrid grid		
Refn. level	N_{rbx}	*d.o.f.*	N_{rmp}	N_r	*d.o.f.*	N_{rmp}	N_r
0	17	303	289	14	544	264	13
1	35	1255	1225	30	2260	1144	30
2	71	5105	5041	64	9104	4752	63
3	143	20579	20449		out of memory		

Table 3.4: Mesh properties for Figure 3.25. N_{rbx} =number of rectangular cells along one side of the square domain, N_r =number of radial mesh points, N_{rmp} =number of rectangular mesh points.

We first note that for the decoupled overlapping grids simulation, the first stage is discretised with cell-centred finite volume method, while the second stage is discretised with vertex-centred finite volume method (thereby allowing the direct computation of pressure values at the wellbore). For the hybrid grid simulation, the discretisation in the entire domain is by cell-centred finite-volume method, and so the wellblock pressure must be extrapolated to the wellbore. Linear extrapolation in the logarithmic radial distance was used here. Secondly, while the second stage of the decoupled overlapping grids method can be solved in one-dimension (as outlined in Section 3.1), a full two-dimensional polar grid must be implemented in the hybrid case thereby increasing the computational effort. For the simulations in this section, the computer ran out of memory for the hybrid grid implementation at the third refinement level.

Simulation results are plotted in Figure 3.25. A mass balance check for the hybrid grid simulations was conducted to confirm conservation. The abrupt change in Figure 3.25(b) suggests a pollution of the error behaviour at the polar-rectangular grid boundary. Prior to this abrupt change, the absolute error for the two methods are of similar magnitude as shown in Figure 3.25(a) and (b). The absolute maximum error plot in Figure 3.25(c) clearly show that the decoupled overlapping grids method gives better performance for fewer degrees of freedom.

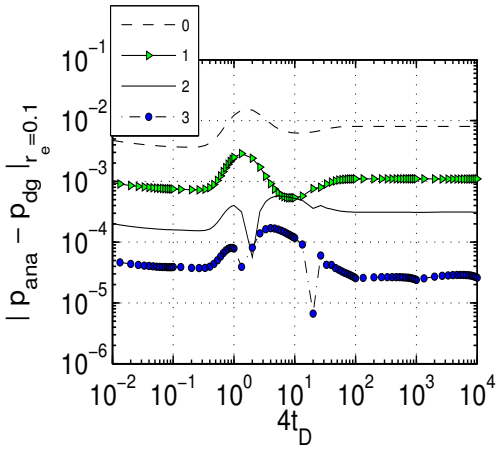

(a) Solution using decoupled overlapping grids method with $\Delta r_{\max} = \frac{h}{2}$. First stage solved on a cell-centred finite-volume mesh.

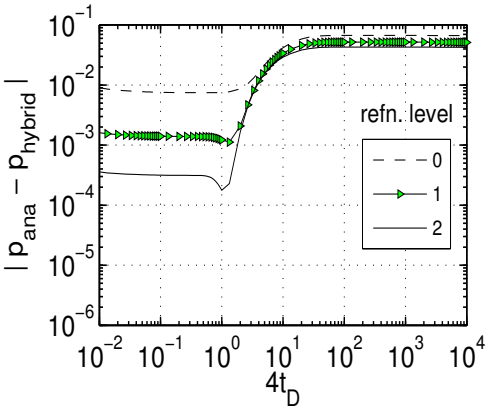

(b) Solution from hybrid grid

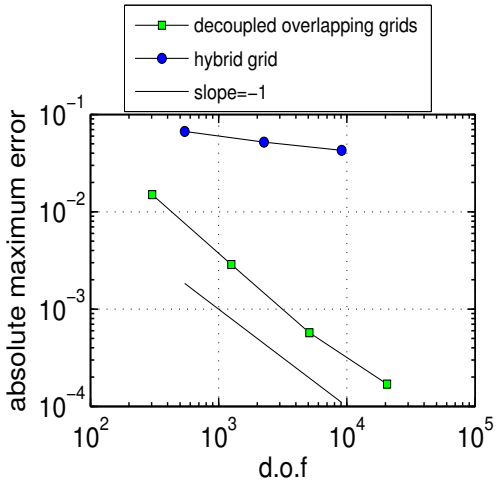

(c) Maximum absolute error for over time interval $4t_D \in [10^{-2}, 10^4]$.

Figure 3.25: Absolute error in dimensionless average wellbore pressure for $r_e = 0.1$ (see Table 3.4).

3.8 Summary

In this chapter we have studied the error in the decoupled overlapping grids method in a two-dimensional homogeneous domain. Numerical experiments showed that the maximum absolute error in the local domain external boundary data interpolated from the first-stage simulations, and in the wellbore pressure from the second-stage simulations, occur during an initial transient stage before the effect of the boundaries are felt. The exception to this is when the local domain external boundary data is measured close to the global domain boundary, in which case an initial transient stage is not observed in the absolute error profile, and the maximum absolute error occurs at steady-state.

The numerical results showed an $\mathcal{O}(h^2)$ convergence in the maximum absolute error of the local domain external boundary pressure and the wellbore pressure. It was also deduced that for $\Delta r_{\max} \leq h/2$, the maximum absolute error in the wellbore pressure is bounded above by the maximum absolute error in the interpolated local domain boundary pressure. Theoretical proof was presented to corroborate these numerical results.

A comparison of decoupled overlapping grids method to some other methods for computing wellbore pressure in the literature was carried out. In all cases the numerical results show better performance from the decoupled overlapping grids method.

Chapter 4

Vertical Well in a Heterogeneous Domain

4.1 Introduction

In this chapter, we apply the method of decoupled overlapping grids to model the transient pressure of a fully-penetrating vertical well in a heterogeneous domain. The heterogeneities discussed are radial, angular and random discontinuity in reservoir permeability and a well near an impermeable boundary. The impermeable boundary considered here is the domain boundary. However the same principle would apply to a well that interacts with other features that introduce heterogeneity within the reservoir, such as sealing faults or fractures. As in the previous chapter, we focus on equations for single-phase flow of a slightly-compressible fluid.

4.2 Discontinuous reservoir permeability

In the previous chapter numerical experiments indicated that for a homogeneous domain the maximum error in average wellbore pressure was bounded above by the maximum error in the average external boundary pressure of the local domain when $\Delta r_{\max} \leq h/2$, where $\Delta r_{\max}$ is the maximum mesh size of the second-stage (local) simulation and h is the average mesh size of the first-stage (global) simulation. Here we investigate the validity of this relationship for three heterogeneous permeability case studies: radial discontinuity, angular

discontinuity, and random discontinuity.

Simulation results are compared against benchmark solutions calculated by the finite element method with the wellbore resolved by local grid refinement. The benchmark simulations are implemented in Comsol Multiphysics. The investigation in Section 3.7.1 showed that the finite element implementation in Comsol with quadratic Lagrange elements gave a significantly better level of accuracy compared to linear Lagrange elements. Therefore quadratic Lagrange elements are used in the benchmark simulations.

The Comsol `bdf_ida` solver is used for time-stepping in the benchmark simulations. This is a variable order, variable step-size solver that implements the backward differentiation formulas (BDF). The linear systems in the simulation are solved by direct LU factorization of the sparse matrix using the `umfpack` solver. On the other hand the time-stepping for the decoupled overlapping grid equations is carried out in Matlab using `ode15s`, a variable order solver based on the numerical differentiation formulas (NDF) [91], which are similar to the BDF. The linear systems in the simulation are solved directly by LU factorization of the sparse matrix, also using the `umfpack` solver. Since both the benchmark and the decoupled overlapping grids simulations are solved using similar methods, we will use the number of degrees of freedom in the simulations as an indication of the amount of work done.

In the subsequent studies the parameters (q, μ, H, c_t, ϕ) are set to 1. Other simulation parameters are listed in Table 4.1.

Parameter	Value
x_e, y_e	1,1
(x_w, y_w)	(0.5,0.5)
r_w	10^{-3}
r_e	0.1, 0.2, 0.3

Table 4.1: Simulation parameters. (x_w, y_w) = well position, r_w = well radius, r_e = radius of post-process domain.

4.2.1 Radial permeability discontinuity

A circular region extending a distance r_{sd} from the centre of the well is assigned a constant permeability k, and the region outside this circle is assigned a constant permeability k_2 where $k/k_2 = 0.1$. The global problem in (3.1) is solved on finite element meshes, some of which are shown in Figure 4.1. Each refinement level is obtained by uniform refinement of the previous level. The corresponding mesh properties are in Table 4.2.

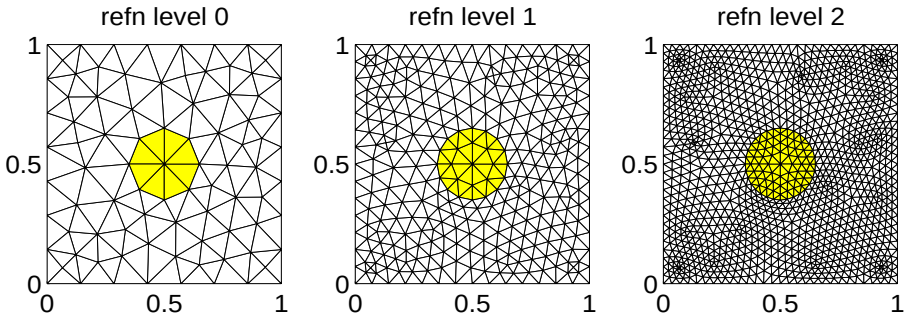

Figure 4.1: Mesh and permeability distribution for first stage. $r_{sd} = 0.15$, $k/k_2 = 0.1$.

R. Level	0	1	2	3
N_t	144	576	2304	9216
N_v *(d.o.f)*	87	317	1209	4721
h	0.1266	0.0633	0.0317	0.0158

Table 4.2: First stage mesh properties. R. Level = refinement level, N_t = number of triangles, N_v =number of vertices.

R. Levels = r_e	$\Delta r_{\max}$	0	1	2	3
			N_r *(d.o.f)*		
0.1	h	0*	5	13	27
	$h/2$	5	13	27	56
	$h/4$	13	27	56	115
0.2	h	0^+	0^+	31	64
	$h/2$	0^+	31	64	131
	$h/4$	31	64	131	265
0.3	h	10	24	51	105
	$h/2$	24	51	105	213
	$h/4$	51	105	213	429

*: $\Delta r_{\max} > r_e$
$^+$: $\Delta r_{\max} > r_e - r_{sd}$

Table 4.3: Second stage mesh properties. N_r =number of radial gridpoints.

In this case study the local problem in (3.2) satisfies the conditions stated in Section 3.1 which allow it to be solved in one (radial) dimension only. The local equations are discretised using the finite volume method. In order to get consistent results, it is necessary for the location of the permeability discontinuity to coincide with a control volume interface. Hence the computation nodes are obtained as follows. Let R_l, R_r denote the positions of the nodes on the left and right sides of the discontinuity respectively (where $R = \ln r$). Given the mesh size on the log scale, $\Delta R = \ln r_e - \ln(r_e - \Delta r_{\max})$, we set

$$R_l = \ln r_{sd} - \Delta R/2, \qquad R_r = \ln r_{sd} + \Delta R/2, \tag{4.1}$$

and compute the number of nodes on the left and right sides of the discontinuity respectively from

$$N_l = \text{ceil}\left[\frac{R_l - \ln r_w}{\Delta R}\right], \qquad N_r = \text{ceil}\left[\frac{\ln r_e - R_l}{\Delta R}\right]. \tag{4.2}$$

The mesh properties for the second stage simulations are in Table 4.3.

Figure 4.2 shows the absolute error profile of average wellbore pressure plotted against dimensionless time $t_{_D} = kt/(\mu\phi c_t r_e^2)$, where the reference permeability k is that of the interior sub-domain. It shows that in general the error in the wellbore pressure goes through a peak value during the initial transient phase before settling to a steady-state value (in a similar manner to the absolute error results for a homogeneous domain discussed in Chapter 3).

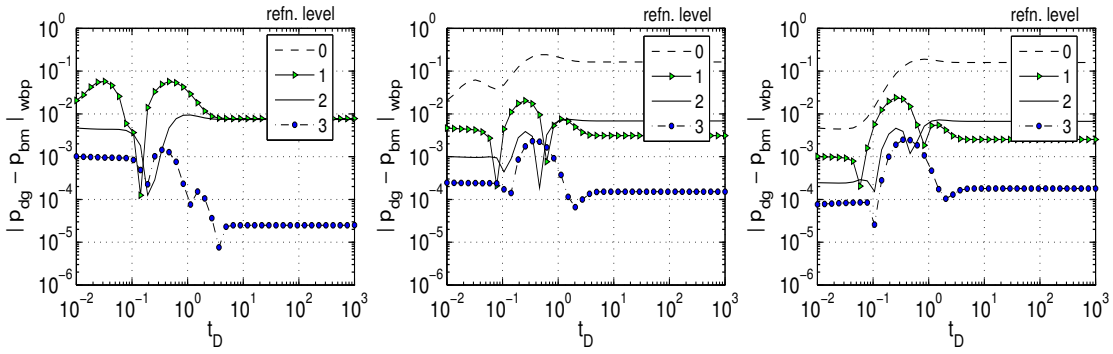

(a) $r_e = 0.1$. $\Delta r_{\max} = h,\ h/2,\ h/4$

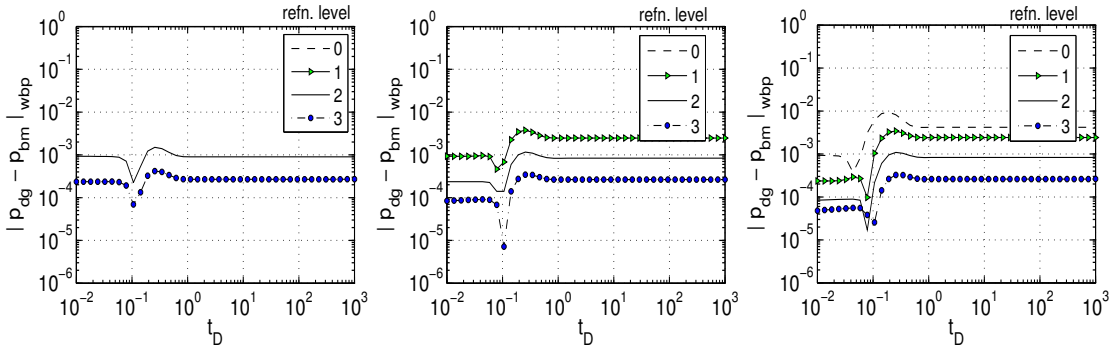

(b) $r_e = 0.2$. $\Delta r_{\max} = h,\ h/2,\ h/4$

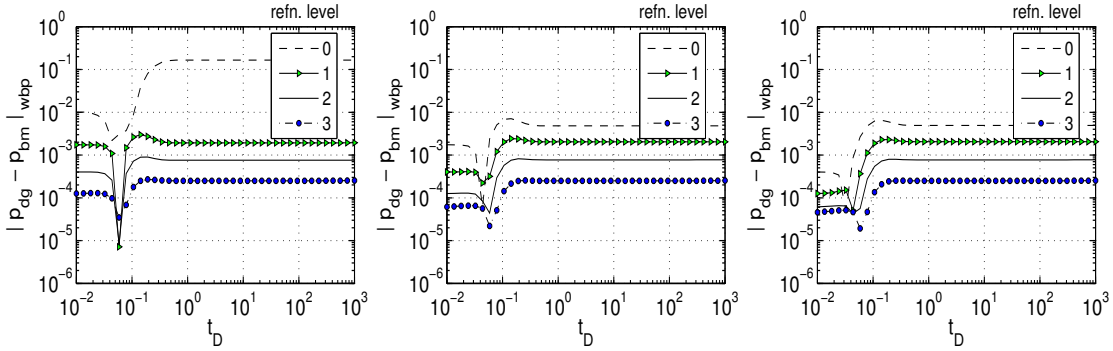

(c) $r_e = 0.3$. $\Delta r_{\max} = h,\ h/2,\ h/4$

Figure 4.2: Absolute error in dimensionless average wellbore error.

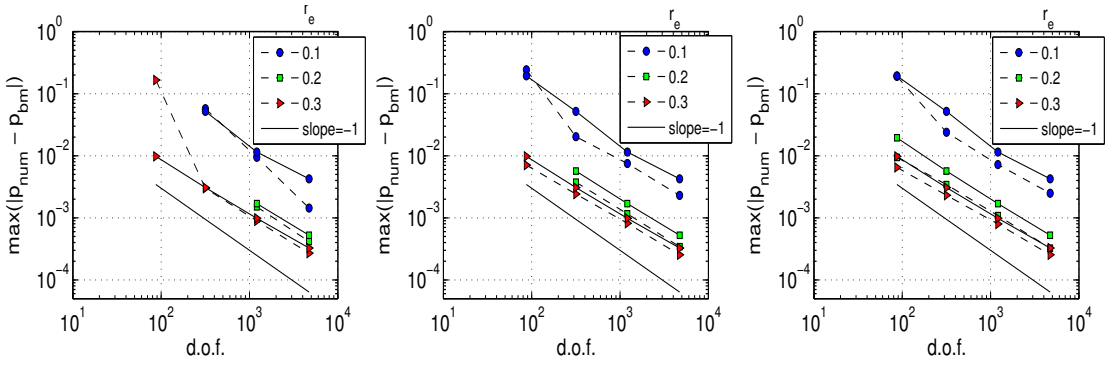

(a) $\Delta r_{\max} \approx h$ **(b)** $\Delta r_{\max} \approx \frac{h}{2}$ **(c)** $\Delta r_{\max} \approx \frac{h}{4}$

Figure 4.3: *Broken lines*: Maximum error in dimensionless average wellbore pressure. *Solid lines*: Maximum error in dimensionless average boundary pressure. Maximum taken over simulation time.

The maximum absolute error in the dimensionless average wellbore pressure and dimensionless average external boundary pressure (of the local domain) are plotted in Figure 4.3 against the degrees of freedom of the finite element mesh used to compute the global solution. It is seen that for $\Delta r_{\max} \leq h/2$ the error in the wellbore pressure is bounded above by the error in the boundary condition. Even for $\Delta r_{\max} \approx h$, the maximum error in the wellbore and boundary pressure are of similar magnitude (for refinement levels of the global simulation ≥ 1). These results are similar to those observed for the homogeneous case study in Section 3.4.2. We also note that there is only a slight deterioration in the $\mathcal{O}(h^2)$ convergence rate that was observed for the homogeneous case.

The degrees of freedom of the mesh used to compute the benchmark solution in this section is 15336. In comparison, the most expensive computation using the decoupled overlapping grids method (refinement level 3 for global solution, $r_e = 0.3$ and $\Delta r_{\max} = h/4$ for local solution) required a total degree of freedom of 5150. Figure 4.3 shows that despite this significant difference in computational effort, the simulation result using the decoupled overlapping grids method comes within a dimensionless absolute error of $\mathcal{O}(10^{-4})$ with respect to the benchmark solution (the actual absolute error is also in the same range).

4.2.2 Angular permeability discontinuity

In this case study the domain is divided into four quadrants. The top right and bottom left quadrants are assigned a permeability value k, and the top left and bottom right quadrants a permeability value k_2 where $k/k_2 = 0.1$. The finite element mesh used in the first stage of the computation is shown in Figure 4.4. Each refinement level is obtained by uniform refinement of the previous level. The corresponding mesh properties are in Table 4.4.

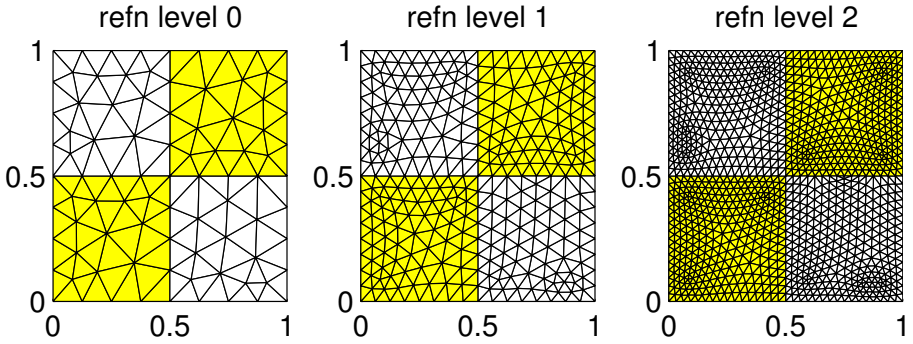

Figure 4.4: Mesh and permeability distribution for first stage. $k/k_2 = 0.1$.

R. Level	0	1	2	3
N_t	142	568	2272	9088
N_v	88	317	1201	4673
h	0.1275	0.0638	0.0319	0.0159

Table 4.4: First stage mesh properties (R. Level = refinement level).

r_e	*R. Levels* = $\Delta r_{\max}$	0	1	2	3
			d.o.f		
0.1	h	0*	337	1345	5537
	$h/2$	108	461	2065	8705
	$h/4$	232	1181	5233	22001
0.2	h	112	485	2193	9281
	$h/2$	256	1309	5809	24585
	$h/4$	1080	4925	21113	85985
0.3	h	176	893	3853	16433
	$h/2$	664	2969	12961	53857

*: $\Delta r_{\max} > r_e$

Table 4.5: Total degrees of freedom for simulations (global + local).

A full 2D problem in R–θ is solved in the circular local domain using the finite volume method. Again it is necessary for the discontinuity to coincide with control volume interfaces of the local mesh to achieve consistent results. The two-dimensional polar mesh is constructed such that the mesh sizes in the R–

θ coordinates are approximately equal. The total degrees of freedom (that is, global+local) used in the simulations is listed in Table 4.5.

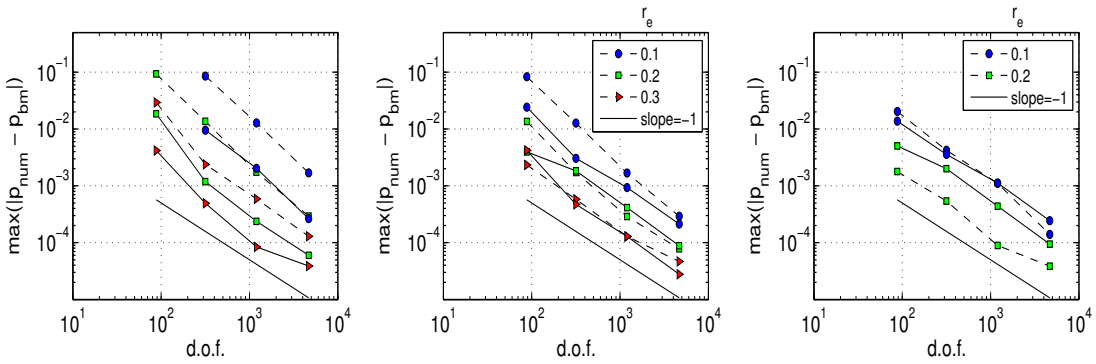

(a) $\Delta r_{\max} = h$ **(b)** $\Delta r_{\max} = \frac{h}{2}$ **(c)** $\Delta r_{\max} = \frac{h}{4}$

Figure 4.5: *Broken lines*: Maximum error in dimensionless average wellbore pressure. *Solid lines*: Maximum error in dimensionless average boundary pressure. Maximum taken over simulation time.

The maximum absolute error in the dimensionless average wellbore pressure and average external boundary pressure (of the local domain) are plotted in Figure 4.5 against the degrees of freedom of the finite element mesh used to compute the global solution. The plot for $\Delta r_{\max} = h$ shows that the maximum error in wellbore pressure is above that of the boundary pressure for all refinement levels of the underlying global simulation simulation. Refining the mesh for the local problem by setting $\Delta r_{\max} = h/2$ results in maximum errors of similar magnitude, especially for $r_e = 0.2$ and 0.3. Further refinement to $\Delta r_{\max} = h/4$ yields better results, with the maximum error in wellbore pressure strictly bounded above by the maximum error in boundary pressure for $r_e = 0.2$. An $\mathcal{O}(h^2)$ convergence rate is observed for the results.

The degrees of freedom of the mesh used to compute the benchmark solution in this section is 34040. In comparison Table 4.5 shows the total degrees of freedom in the simulations using decoupled overlapping grids. Most entries in this table are less than half the degrees of freedom of the benchmark solution, and for the highest of these (refinement level 3, $r_e = 0.3$, $\Delta r_{\max} = h$), the maximum absolute dimensionless error in the wellbore pressure is within $\mathcal{O}(10^{-4})$ of the benchmark solution (the actual absolute error is in the same range). Therefore a high level of accuracy can be achieved using the decoupled overlapping grids for significantly

less computational effort.

The absolute error profiles for the exterior and interior (wellbore) boundaries of the local domain are plotted against dimensionless time in Figure 4.6 and Figure 4.7 respectively (reference permeability = k). Most of the plots for the error in boundary pressure show the characteristic property of reaching a maximum during an initial transient phase before settling to a steady-state value, with exceptions occurring in the coarser simulation cases (see Figure 4.6). On the other hand, for the wellbore pressure (see Figure 4.7), only the very refined grids show this property of the absolute error attaining a maximum during an initial transient phase. This is because the strong heterogeneity present at the wellbore makes the use of a very fine mesh at the wellbore necessary in order to obtain this property of the absolute error. Comparison of plots in Figure 4.6 and Figure 4.7 to Figure 4.5 indicates that the maximum absolute error in wellbore pressure is bounded above (or of a similar magnitude) to the maximum absolute error in boundary pressure only when this property of the maximum absolute error occurring during an initial transient phase is satisfied in both the global and local simulations.

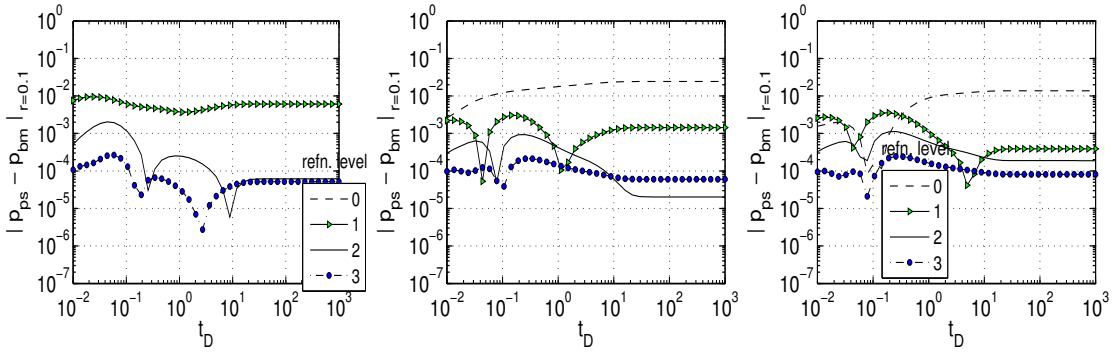

(a) $r_e = 0.1$. $\Delta r_{\max} = h,\ h/2,\ h/4$

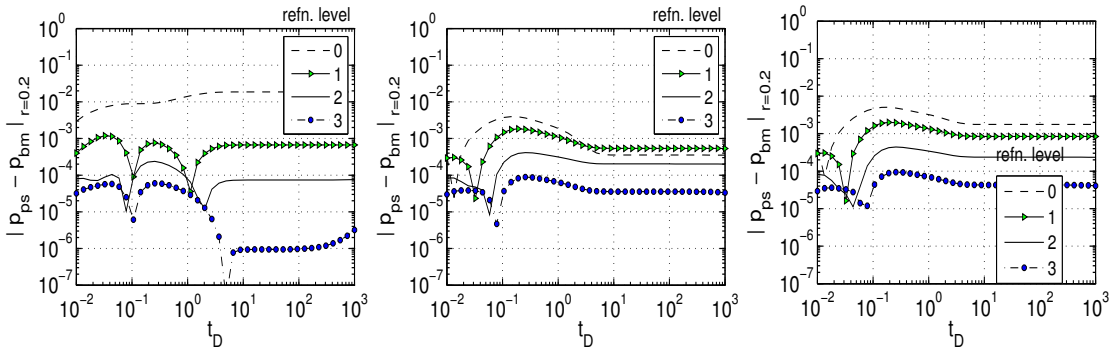

(b) $r_e = 0.2$. $\Delta r_{\max} = h,\ h/2,\ h/4$

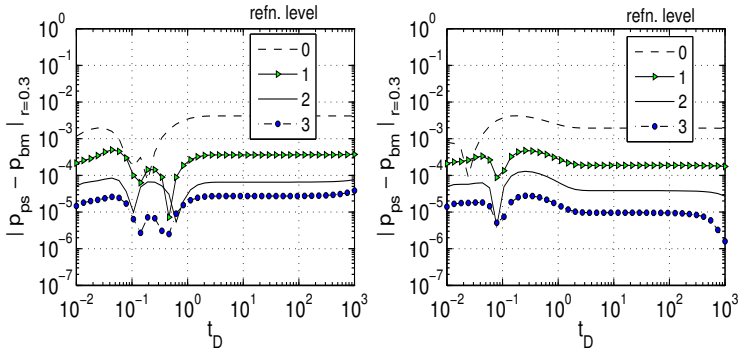

(c) $r_e = 0.3$. $\Delta r_{\max} = h,\ h/2$

Figure 4.6: Absolute error in dimensionless boundary error for local domain.

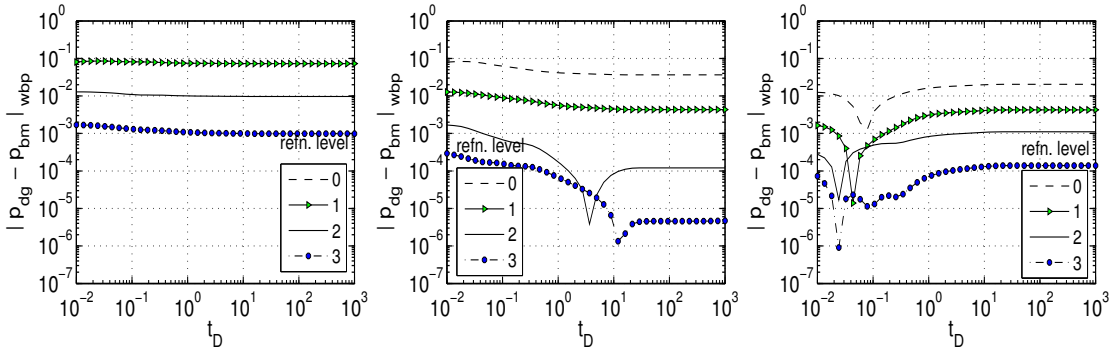

(a) $r_e = 0.1$. $\Delta r_{\max} = h,\ h/2,\ h/4$

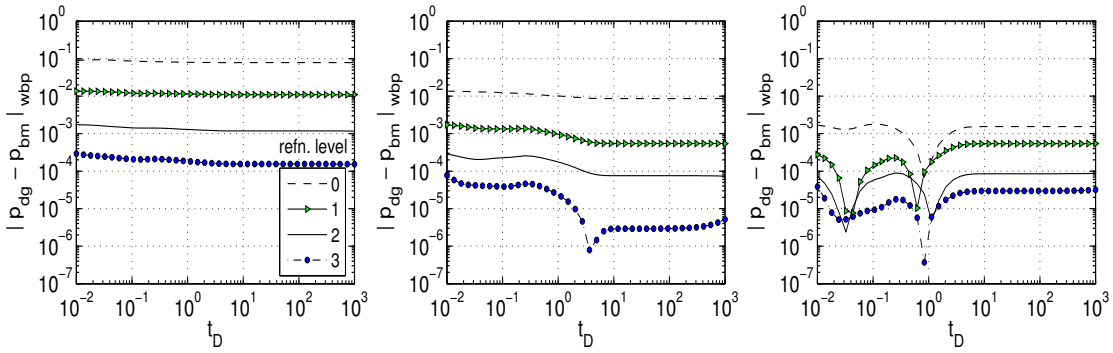

(b) $r_e = 0.2$. $\Delta r_{\max} = h,\ h/2,\ h/4$

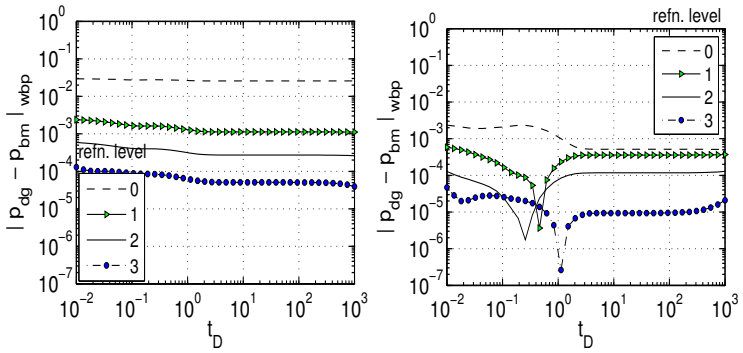

(c) $r_e = 0.3$. $\Delta r_{\max} = h,\ h/2$

Figure 4.7: Absolute error in dimensionless wellbore error.

4.2.3 Fully heterogeneous permeability distribution

The computational domain in this section is assigned an isotropic, correlated, log-normal random permeability distribution, which is a closer representation of a realistic reservoir permeability distribution. The permeability distribution is generated using the method outlined by Eberhard [43].

To begin with, a random field is generated from

$$F_N(x) := \overline{F} + \sqrt{\frac{2\sigma_F^2}{N}} \sum_{j=1}^{N} \cos\left(q^{(j)} \cdot x + \alpha^{(j)}\right), \qquad x \in \mathbb{R}^d, \tag{4.3}$$

where $\overline{F}$ and σ_F^2 are the mean and variance of the random field respectively. The vectors $q^{(j)}$ and the phases $\alpha^{(j)}$ are independent random numbers whose distributions determine the covariance function of the resulting random field F_N.

To generate a Gaussian covariance spectrum of the form

$$C(x - x') = \sigma_F^2 \exp\left(-\sum_{i=1}^{d} \frac{(x_i - x_i')^2}{2l_i^2}\right) \tag{4.4}$$

with correlation lengths l_i in the direction x_i, $i = 1 \ldots, d$, and variance σ_F^2, the components $q_i^{(j)}$ are drawn from a Gaussian distribution with vanishing average and variance $1/l_i^2, i = 1, \ldots, d$. The phases $\alpha^{(j)}$ are uniformly distributed in the interval $[0, 2\pi]$. In the limit as $N \to \infty$, due to the central limit theorem, $F_N(x)$ is a Gaussian distributed random field characterised by the covariance function in (4.4) [43].

Given the Gaussian random field $F_N(x)$, the lognormal random field $f(x)$ is then generated from $f(x) = \exp(F_N(x))$.

Figure 4.8 shows the mesh permeability distribution for the first stage of the computations. Each refinement level is obtained by uniform refinement of the previous level. The original permeability distribution is generated at the vertices of the coarse mesh (refinement level 0), and extended to new vertices in subsequent refinement levels by linear interpolation. The parameters used to generate the coarse permeability distribution are $\overline{F} = 2, \sigma_F^2 = 3, l_i = 0.1 (i = 1, 2)$. Mesh properties are in Table 4.6.

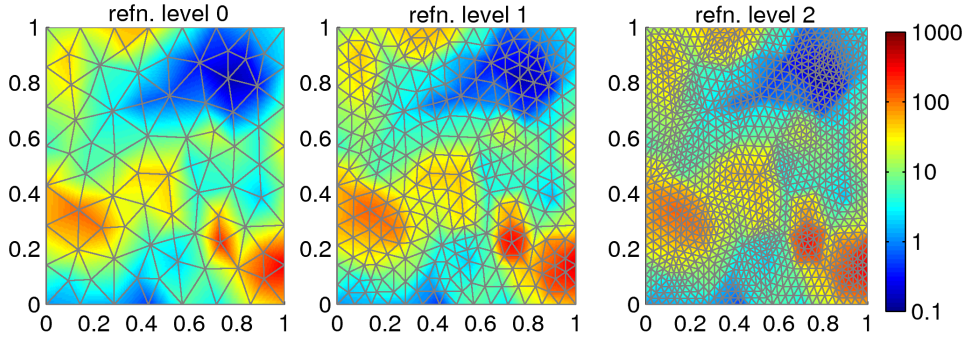

Figure 4.8: Mesh for first stage (permeability interpolated from values at triangle nodes)

R. Level	0	1	2	3
N_t	144	576	2304	216
N_v	87	317	1209	4721
h	0.1266	0.0633	0.0317	0.0158

Table 4.6: First stage mesh properties (R. Level = refinement level).

R. Levels =		0	1	2	3
r_e	$\Delta r_{\max}$		*d.o.f*		
0.1	h	0	337	1417	5585
	$h/2$	107	525	2073	8753
	$h/4$	295	1181	5241	22201
0.2	h	111	485	2201	9401
	$h/2$	255	1309	5889	24785
	$h/4$	1079	4997	21273	87713
0.3	h	175	917	4121	16593
	$h/2$	687	3229	13081	54369

*: $\Delta r_{\max} > r_e$

Table 4.7: Total degrees of freedom for simulations.

The local problem is solved in a two-dimensional polar region using the finite volume method. The permeability distribution for the local problem is interpolated linearly from the original coarse permeability distribution on refinement level 0. The total degrees of freedom (that is, global+local) used in the simulations are listed in Table 4.7.

Figure 4.9 shows the absolute maximum error in dimensionless average wellbore and average external boundary pressures (of the local domain). It is seen that with the exception of $r_e = 0.3$, the maximum errors are within the same order of magnitude. The absolute error is plotted against dimensionless time for the average wellbore and average external boundary pressures in Figure 4.10 and Figure 4.11 respectively (reference permeability $k = 1$). The graphs show that although there is an initial transient period followed by a steady-state er-

ror, the maximum error hardly ever occurs during the initial transient phase. A possible reason for this is the fact all permeabilities are interpolated from the base coarse permeability distribution on refinement level 0, and so are approximations of the original rather than being exactly equal as in the previous case studies. Nevertheless, the maxima are not far apart, and Figure 4.9 shows an $\mathcal{O}(h^2)$ convergence rate. Also a comparison of the peak errors that occur before steady-state is reached in Figure 4.10 and Figure 4.11 shows that the initial peak wellbore error is bounded above by the initial peak error at the boundary.

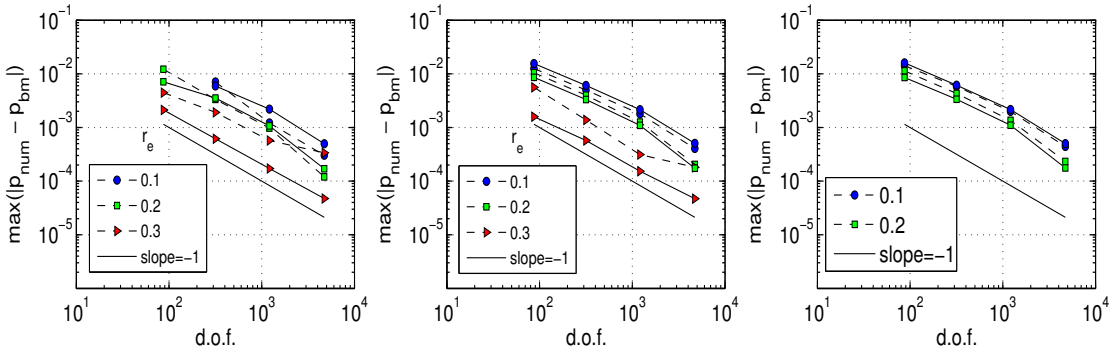

(a) $\Delta r_{\max} = h$ **(b)** $\Delta r_{\max} = \frac{h}{2}$ **(c)** $\Delta r_{\max} = \frac{h}{4}$

Figure 4.9: *Broken lines*: Maximum error in dimensionless wellbore pressure. *Solid lines*: Maximum error in dimensionless boundary pressure. Maximum taken over simulation time.

The degrees of freedom of the mesh used to compute the benchmark solution in this section is 43060. In comparison Table 4.7 shows the total degrees of freedom in global and local computations. Most entries in this table are less than half the degrees of freedom of the benchmark solution, and for the highest of these (refinement level 3, $r_e = 0.3$, $\Delta r_{\max} = h$), the maximum absolute dimensionless error in the wellbore pressure is within $\mathcal{O}(10^{-4})$ of the benchmark solution (the actual absolute error is in the same range). Therefore a high level of accuracy can be achieved for significantly less computational effort.

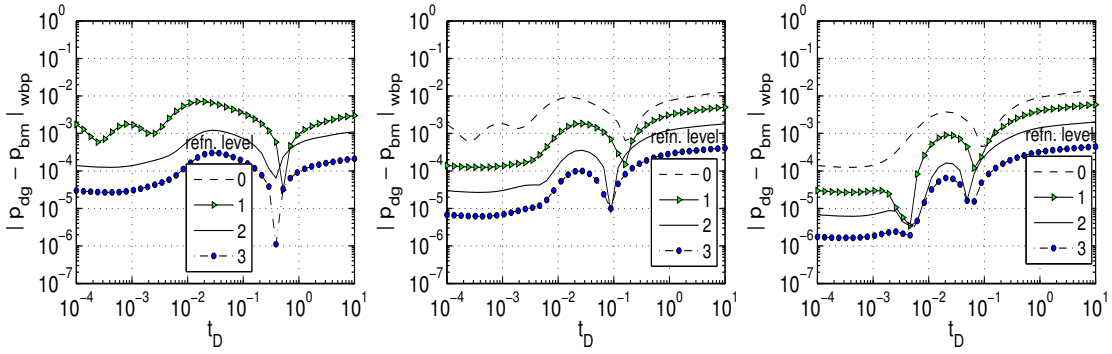

(a) $r_e = 0.1$. $\Delta r_{\max} = h,\ h/2,\ h/4$

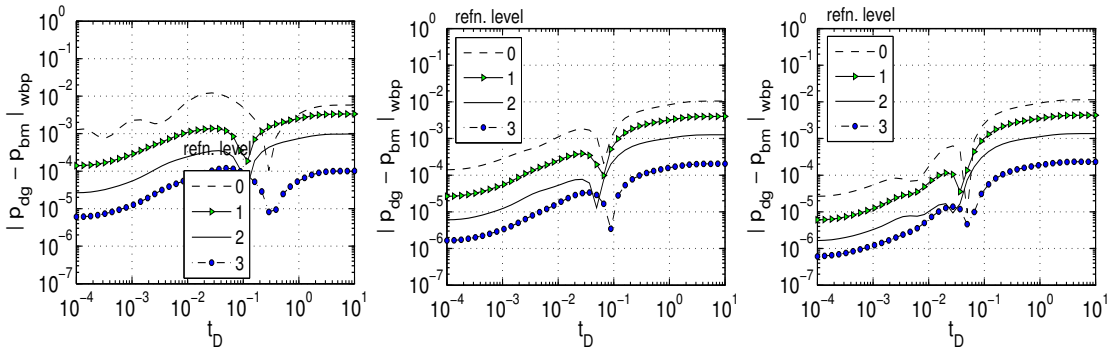

(b) $r_e = 0.2$. $\Delta r_{\max} = h,\ h/2,\ h/4$

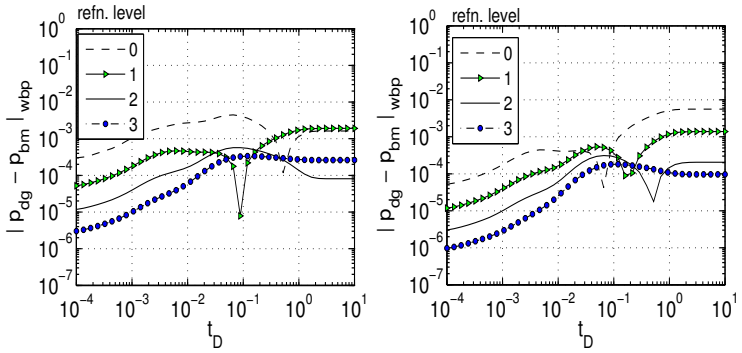

(c) $r_e = 0.3$. $\Delta r_{\max} = h,\ h/2$

Figure 4.10: Absolute error in dimensionless wellbore error.

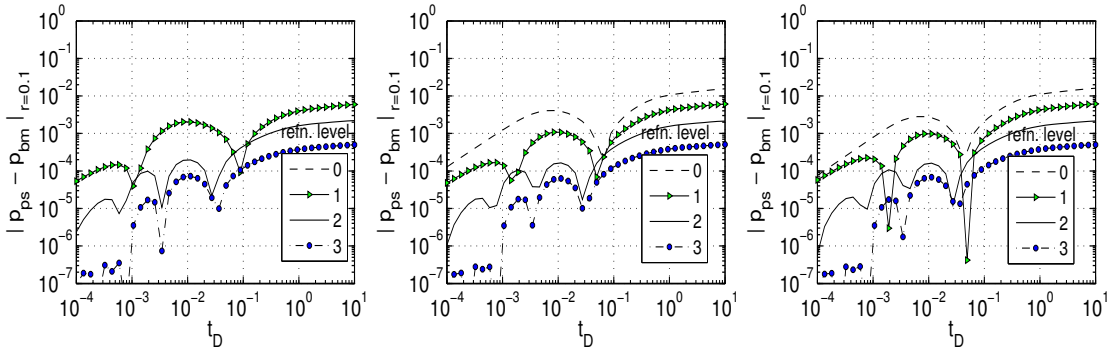

(a) $r_e = 0.1$. $\Delta r_{\max} = h,\ h/2,\ h/4$

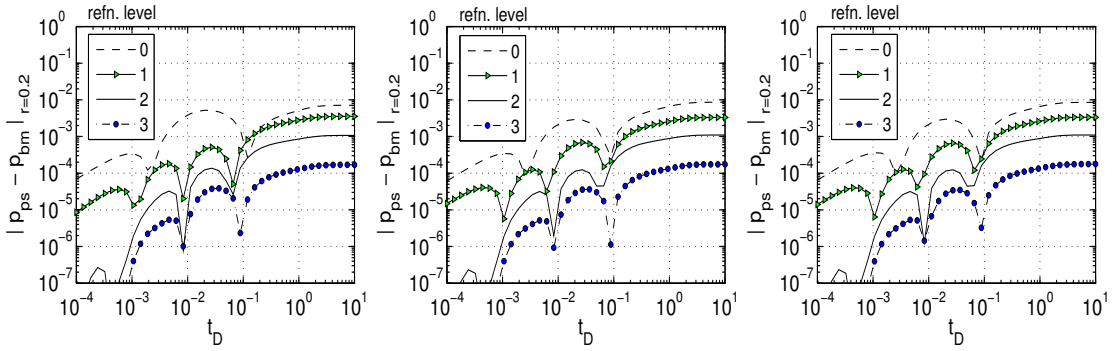

(b) $r_e = 0.2$. $\Delta r_{\max} = h,\ h/2,\ h/4$

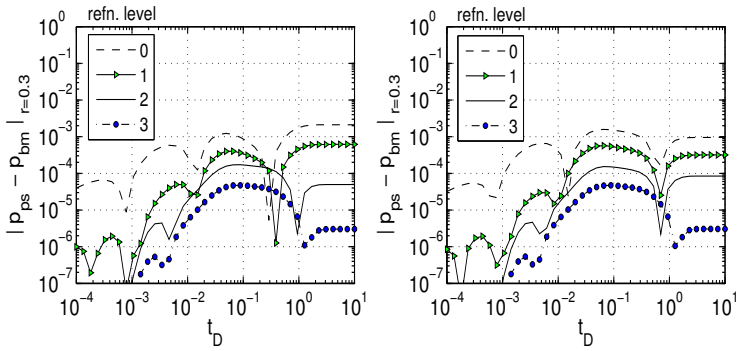

(c) $r_e = 0.3$. $\Delta r_{\max} = h,\ h/2$

Figure 4.11: Absolute error in dimensionless boundary error for local domain.

4.3 Impermeable boundary

In this study a well is placed close to the impermeable domain boundary so that the post-process domain intersects the impermeable boundary. This example illustrates the relative ease with which the method of decoupled overlapping grids can be applied to compute transient well pressure in complex reservoir geometry. The principle extends to other similar problems such as a well close to a fault or a fracture.

We maintain the parameter values in Table 4.1 with the exception of the well position (x_w, y_w) which is now (0.85,0.5). Also we consider a homogeneous domain with parameters $(q, \mu, H, c_t, \phi, k) = 1$. A representation of the model problem is shown in Figure 4.12. As before the local post-process domain is defined from the wellbore to a fixed radial distance away. However in this case the external boundary of the local domain is intersected by the global impermeable boundary for some external radii r_e.

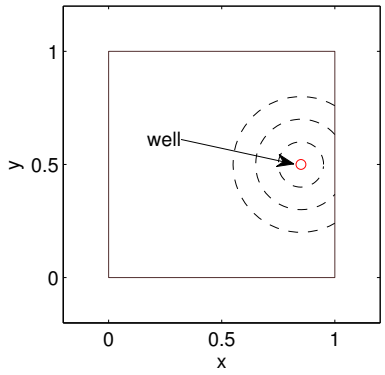

Figure 4.12: Model problem. Well position:$(x_w, y_w) = (0.85, 0.5)$. Broken lines show post-process domain for $r_e = 0.1, 0.2, 0.3$.

The local problem is solved in the transformed R–θ coordinate system ($R := \ln r$). The solution domain in this coordinate system is rectangular if the local domain is not intersected by the global domain; otherwise it has a curved edge. Taking advantage of the symmetry of this case study along $y = 0.5$, the local solution is computed only in $\theta = 0 : \pi$, applying a no-flow boundary condition at $\theta = 0$ and $\theta = \pi$. The broken lines in Figure 4.12 show the Dirichlet section of the local domain external boundary for different external radii r_e. The data for this section is interpolated from the solution of the global problem. For $r_e = 0.2, 0.3$,

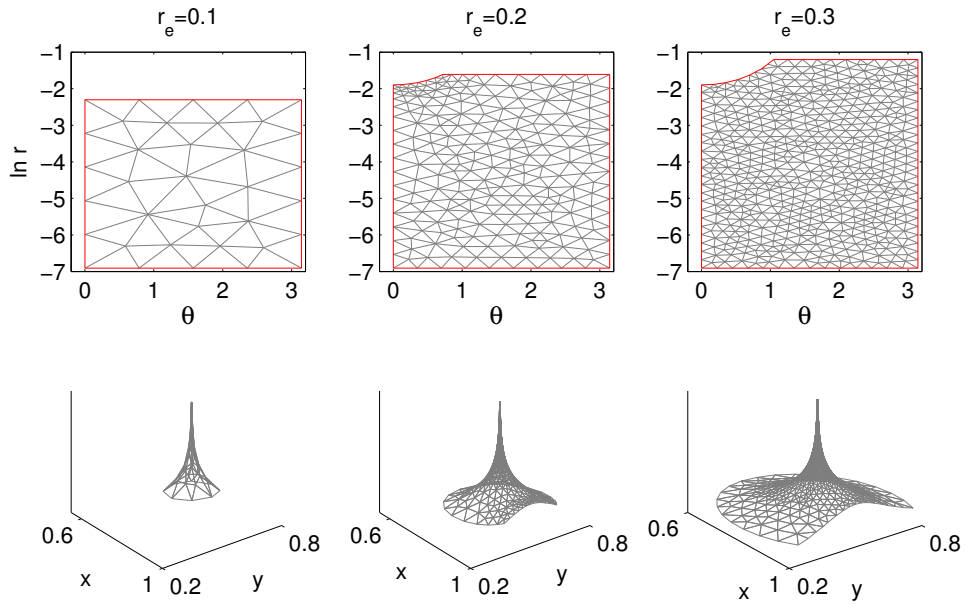

Figure 4.13: Meshes in transformed local domain and approximate solution at end of the simulation. Global refinement level = 2, $\Delta r_{\max} = h$.

the global boundary intersects the local domain to give the Neumann section of the local domain external boundary. This section satisfies the no-flow condition global boundary condition.

We semi-discretize both global and local problems using the finite element method on a triangular mesh, which is easy to adapt to the irregular shape of the local computational domain. The curved edge in the transformed local domain is approximated by a minimum of 6 segments, and when more than 6 segments are used the number of segments is chosen so as to keep the mesh size in the transformed local domain fairly uniform. Sample meshes in the transformed local solution domain, together with the computed solution at the end of the simulations, are shown in Figure 4.13. The mesh properties for the global and local simulations are listed in Table 4.8. Here h denotes the maximum mesh size in the global domain and $\Delta r_{\max}$ denotes the maximum mesh size in the original (untransformed) local domain.

R. Levels =		0	1	2	3
Global					
	d.o.f	87	317	1209	4271
	h	0.1266	0.0633	0.0317	0.0158
Local					
r_e	$\Delta r_{\max}$	*d.o.f*			
0.1	h	0*	36	198	860
	$h/2$	36	198	860	3695
0.2	h	101	245	995	4260
	$h/2$	245	995	4260	17663
0.3	h	135	569	2452	10285
	$h/2$	569	2452	10285	42432

Table 4.8: Mesh properties.

R. Levels =		0	1	2	3
r_e	$\Delta r_{\max}$	*d.o.f*			
0.1	h	0*	353	1407	5581
	$h/2$	123	515	2069	8416
0.2	h	188	562	2204	8981
	$h/2$	332	1312	5469	22384
0.3	h	222	886	3661	15006
	$h/2$	656	2769	11494	47153
*: $\Delta r_{\max} > r_e$					

Table 4.9: Total degrees of freedom.

A comparison of the maximum absolute error in the internal (wellbore) and external boundaries of the local domain is plotted in Figure 4.14 against the degrees of freedom for the global stage simulation. The error at the external boundary is computed only for the Dirichlet boundary portion, which has data interpolated linearly from the underlying global solution. The plots show that for the irregular domains ($r_e = 0.2, 0.3$) the maximum error in the wellbore pressure is bounded above by the maximum error in the boundary pressure for $\Delta r_{\max} = h, h/2$. For $r_e = 0.1$ this property is true for $\Delta r_{\max} = h/2$, while for $\Delta r_{\max} = h$ the errors are within the same order of magnitude. The plots also show an $\mathcal{O}(h^2)$ convergence of the error. Therefore the results for a well near an impermeable boundary agree with those obtained for an isolated well in

Chapter 3.

The degrees of freedom of the mesh used to compute the benchmark solution in this section is 14334. In comparison Table 4.9 shows the total degrees of freedom from the global and local computations. Again most entries in Table 4.9 are less than half the degrees of freedom of the benchmark solution, and from Figure 4.14 it is seen that high level of accuracy can be achieved for significantly less computational effort.

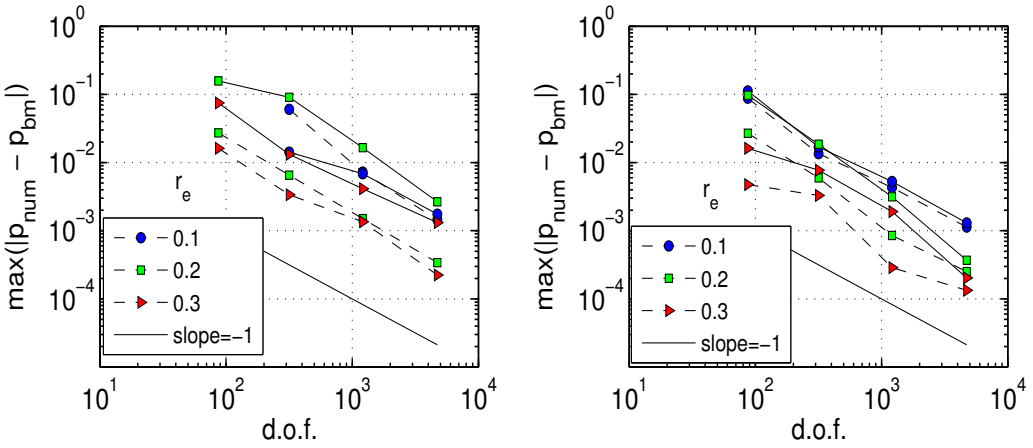

(a) $\Delta r_{\max} = h$ **(b)** $\Delta r_{\max} = \frac{h}{2}$

Figure 4.14: *Broken lines*: Maximum error in dimensionless wellbore pressure. *Solid lines*: Maximum error in dimensionless boundary pressure. Maximum taken over simulation time.

4.4 Summary

In this chapter we have presented some examples which show that the decoupled overlapping grids method can be used to accurately compute transient wellbore pressure in the presence of heterogeneities within the reservoir. The simulation results support the guideline suggested in Chapter 3 of setting $\Delta r_{\max} \leq h/2$ to get the maximum error in average wellbore pressure at least within the same magnitude as the maximum error in the average boundary pressure of the local domain.

Chapter 5

Uniform Flux Strip

In this chapter we discuss an application of the decoupled overlapping grids method to compute the pressure at a strip or crack producing at a uniform rate. This problem can be seen as a simplified model for a fully penetrating fractured vertical well.

5.1 Model description

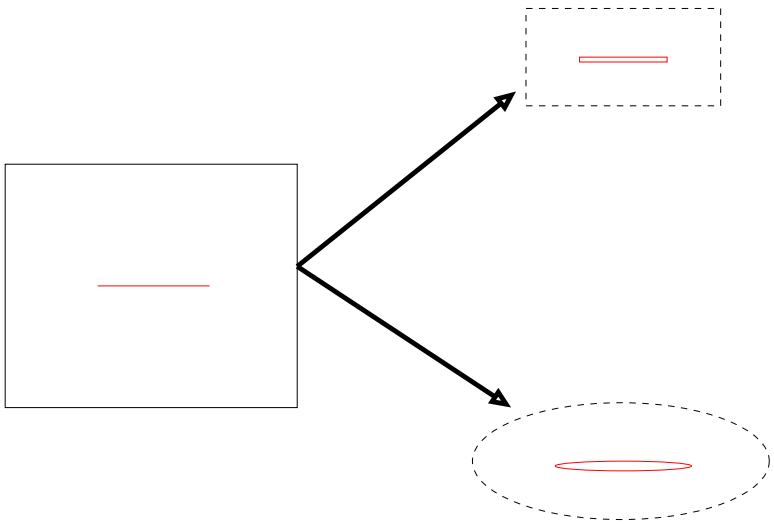

Figure 5.1: Schematic representation of problem.

A producing strip of length equal to 0.4 and width equal to 0.002 is centred in a square domain of length 1. A schematic representation of the first and second (post-process) stages of the problem is shown in Figure 5.1. The first

stage is solved in the global domain with the producing strip modelled by a line source. Computations for the post-process stage in elliptic and rectangular domains are discussed in the sections below. The benchmark solution is calculated in Comsol Multiphysics using quadratic Lagrange elements. For the simulations in this chapter the parameters $(q, \mu, H, c_t, k) = 1$.

In the first stage simulations the line source is approximated by a collection of point sources on a triangular finite element mesh. The point sources are not constrained to vertices of the mesh, rather the vertices of the enclosing triangles are assigned weights based on the location of the point sources. In Section 5.2 and Section 5.3 below, the post-process stage computations are carried out in a rectangular domain and an elliptic domain respectively.

5.2 Post-process stage in rectangular domain

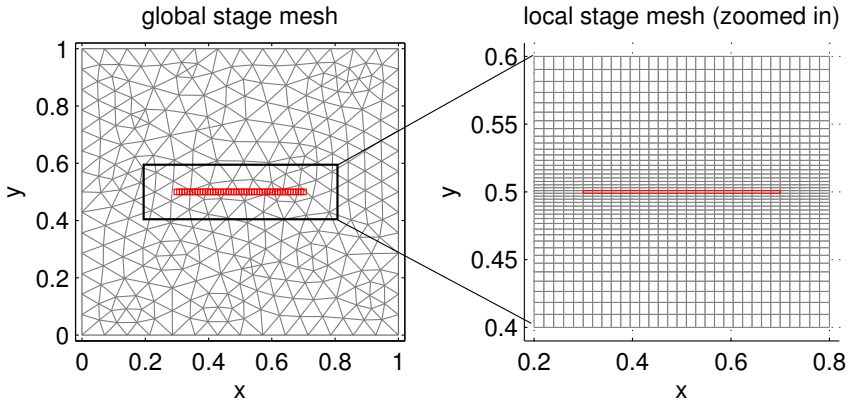

Figure 5.2: Mesh for global and local stage simulations showing the line source and strip locations respectively. Global mesh d.o.f = 317, local mesh d.o.f = 1250.

Figure 5.2 shows the mesh used in the global and local simulations in this section. For the local stage the mesh is non-uniform and graded in the y–direction, and the uniform flux strip is modelled explicitly as a hole in the mesh. Spatial discretisation on the local mesh is by the cell-centred finite volume method. Simulation tests were carried out which showed that the error from this method was (slightly) better than the error from the vertex-centred finite volume method. The pressure at the wellbore was obtained by linear extrapolation using the equation

for the flux at the wellbore:

$$\mathbf{n} \cdot \left(\frac{\mathbf{k}}{\mu} \nabla p_{\text{fw}}(\mathbf{x}, t) \right) = -q_l(t),$$

where q_l is the flux per unit length of the wellbore.

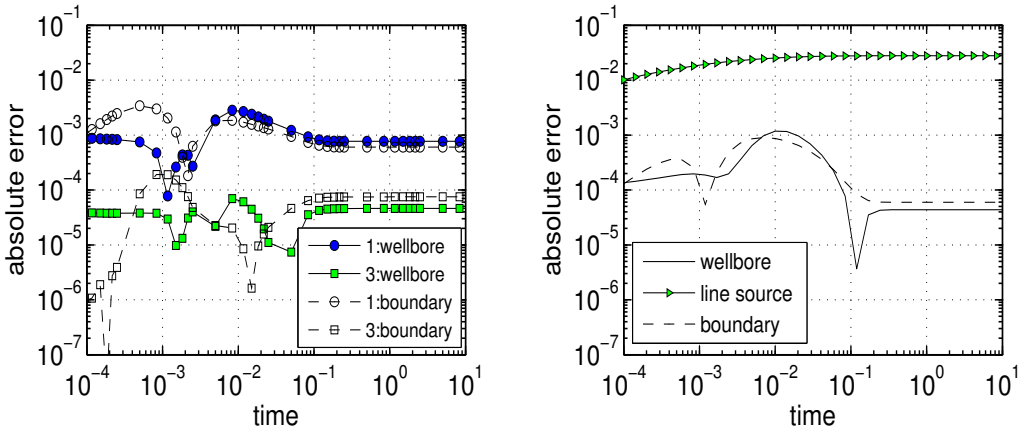

(a) Absolute error for fully penetrating vertical well in homogeneous domain where $r_e = 0.1, \Delta r_{\max} = \frac{h}{2}$ (see Section 3.4.2).

(b) Absolute error for configuration in Figure 5.2. $\Delta r_{\max} < \frac{h}{2}$.

Figure 5.3: Absolute error in average pressure at wellbore and local domain boundary for a fully penetrating vertical well and a fully penetrating crack. The numbers in the legend of (a) indicate refinement levels. Benchmark solution d.o.f. = 17454.

Absolute error results are plotted in Figure 5.3, alongside absolute error results obtained in Section 3.4.2 for a fully penetrating vertical well in a homogeneous reservoir. We note that for the uniform flux strip problem $h/4 < \Delta r_{\max} < h/2$, where $\Delta r_{\max}$ denotes the maximum mesh size in the local domain and h the average mesh size in the underlying global grid. It is seen that for the uniform flux strip problem, the maximum error in the average pressure at the wellbore and local domain boundary occur during an initial transient stage, in a similar manner to the vertical well problem. In addition the maximum errors in Figure 5.3(b) are within the same range. Also plotted in Figure 5.3(b) is the error in the pressure at the strip surface interpolated from the global line source simulation. It is seen that this error is much worse than that of the solution from the decoupled overlapping grids method.

The degrees of freedom of the mesh used to compute the benchmark solution

in this section is 17454. In comparison the total degrees of freedom used in the decoupled overlapping grids computation is 1567. Figure 5.3 shows that the maximum error in the average pressure at the producing strip comes within $\mathcal{O}(10^{-3})$ of the benchmark solution. So a high level of accuracy is achieved from the decoupled overlapping grids method for significantly fewer degrees of freedom.

5.3 Post-process stage in elliptic domain

Here the equations in (3.2) are written in elliptic coordinates. In order to get logarithmically spaced ellipses, we use the following definition of Cartesian to elliptic coordinate system:

$$x = a\cosh e^{\mu}\cos\theta,\ \ y = a\sinh e^{\mu}\sin\theta, \tag{5.1}$$

where e^{μ} is a non-negative number, $\theta \in [0, 2\pi)$, and $-a, +a$ are the locations of the foci. So the equations in (3.2) take the form

$$\frac{\partial p_{\text{fw}}(\mathbf{x},t)}{\partial t} = \frac{1}{a^2(\sinh^2 e^{\mu} + \sin^2\theta)}\left[e^{-\mu}\frac{\partial}{\partial\mu}\left(e^{-\mu}\frac{\partial p_{\text{fw}}(\mathbf{x},t)}{\partial\mu}\right) + \frac{\partial^2 p_{\text{fw}}(\mathbf{x},t)}{\partial\theta^2}\right] \text{ in } \Gamma\times(0,T] \tag{5.2a}$$

$$e^{-\mu}\frac{\partial p_{\text{fw}}(\mathbf{x},t)}{\partial\mu} = a\sqrt{\sinh^2 e^{\mu} + \sin^2\theta}\,\frac{q}{|\partial\Gamma_w|} \qquad \text{in } \partial\Gamma_w\times(0,T] \tag{5.2b}$$

$$p_{\text{fw}}(\mathbf{x},t) = p_{\text{ps}}(\mathbf{x},t) \qquad \text{in } \partial\Gamma_o\times(0,T] \tag{5.2c}$$

$$p_{\text{fw}}(\mathbf{x},0) = 0 \qquad \text{in } \Gamma \tag{5.2d}$$

which are discretised in space using the vertex-centred finite volume method. Figure 5.4 shows the mesh used in the global and local simulations.

Absolute error results are plotted in Figure 5.5, alongside absolute error results obtained in Section 3.4.2 for a fully penetrating vertical well in a homogeneous reservoir. We note that in this case $h/2 < \Delta r_{\max} < h$ for the uniform flux strip problem, where $\Delta r_{\max}$ denotes the maximum mesh size in the local domain and h the average mesh size in the underlying global grid. The absolute error results for an elliptic post-process domain (see Figure 5.5(b)) are similar to those obtained

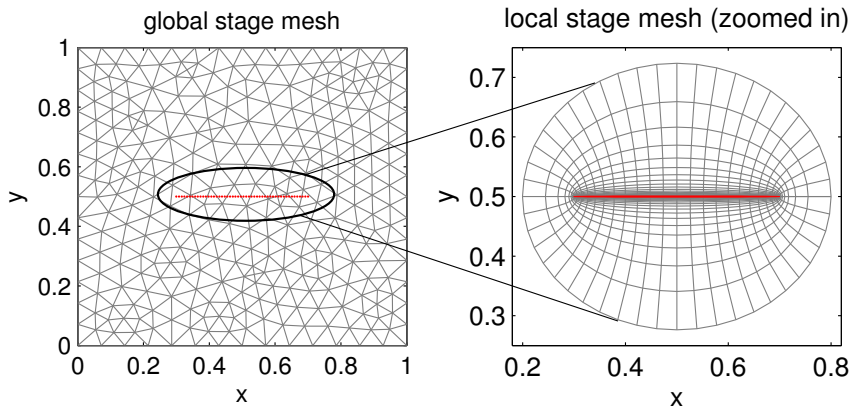

Figure 5.4: Mesh for global and local stage simulations showing the line source and strip locations respectively. Global mesh d.o.f = 317, local mesh d.o.f = 960.

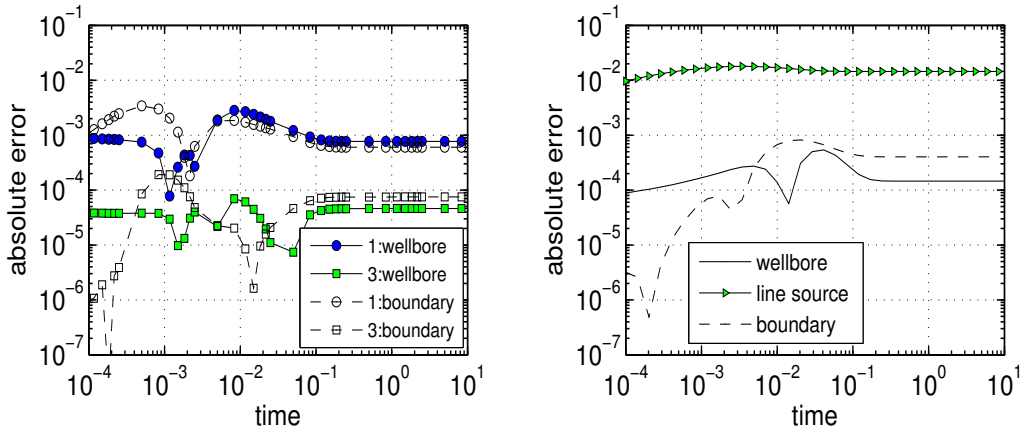

(a) Absolute error for fully penetrating vertical well in homogeneous domain where $r_e = 0.1, \Delta r_{\max} = \frac{h}{2}$ (see Section 3.4.2).

(b) Absolute error for configuration in Figure 5.4. $\Delta r_{\max} > \frac{h}{2}$.

Figure 5.5: Absolute error in average pressure at wellbore and local domain boundary for fully penetrating vertical well and fully penetrating crack. The numbers in the legend in (a) indicate refinement levels. Benchmark solution d.o.f. = 17672.

for a rectangular post-process domain (see Figure 5.3(b)). The maximum absolute error in the simulations occur during an initial transient phase, and these maxima are in the same range. The absolute error in the average pressure at the strip surface from the decoupled overlapping grids method is much better than the absolute error in the average pressure calculated by interpolating the global line source solution to the strip surface. Also since the degrees of freedom for the benchmark computation is 17672 while the total degrees of freedom of the

decoupled overlapping grids computation is 1277, and the maximum error in the wellbore pressure is $\mathcal{O}(10^{-3})$, it is clear that high level of accuracy is achieved from the decoupled overlapping grids method for significantly fewer degrees of freedom.

5.4 Summary

We have applied the decoupled overlapping grids method to compute the pressure at a thin strip producing at a uniform rate in a homogeneous domain. This problem can be seen as a simplified model of a fully penetrating vertically fractured well. Computations for the post-process stage were carried out in a rectangular domain and an elliptic domain. In both cases the simulation results show that a high level of accuracy can be achieved for significantly less computational effort, when compared to benchmark solutions where the strip is fully resolved by local refinement and the spatial discretisation method implemented is the finite element method with quadratic Lagrange elements. Also the absolute error trends (in average strip and local domain boundary pressure) for this problem are similar to those for a fully penetrating vertical well in a homogeneous domain: the maximum error occurs during an initial transient phase, and the maximum error in the average strip pressure is bounded above or at least within the same range as the maximum error in the average pressure of the local domain boundary.

Chapter 6

Horizontal Well Model

6.1 Introduction

In this chapter the method of decoupled overlapping grids is applied to compute the transient pressure of a horizontal well in a three-dimensional drainage region. We validate numerical results by comparison with semi-analytic solutions. An application to wells inclined at an angle to the principal axes (slanted wells) is also discussed. Two classical boundary conditions of flow into the well, the uniform flux and uniform pressure conditions, are investigated.

6.2 Background

Although horizontal wells have been studied for some time now, most work on the computation of the transient wellbore pressure of horizontal wells in a three-dimensional domain deal with analytic and semi-analytic models (see for example [4, 11, 20, 21, 39, 46, 49, 51–54, 66, 71, 75–79, 86, 87]).

One of the early analytic models for a horizontal well was by Gringarten and Ramey [52–54], who applied appropriate source (Green's) functions together with Newman's product to generate analytic models for different simplified reservoir configurations. Ozkan and Raghavan [76] extended these models by documenting a library of solutions in the Laplace domain. Goode and Thambynayagam [51] applied successive integral transforms to solve a model where the horizontal well was first approximated by a thin strip. Using this method they identified different flow regimes for early, intermediate and late time flows. These flow regimes are

useful for estimating reservoir properties, for instance, horizontal permeability can be estimated from the early-time linear flow [19]. Other methods that have been applied to horizontal well modelling include the boundary element method [39, 46], discrete flux element method [10], and Fourier series method [11, 20, 21] (although this model is strictly only accurate at pseudo-steady state).

For simplified reservoir properties, analytic and semi-analytic models for computing the transient pressure of horizontal wells typically require less computational resources when compared to a full scale numerical implementation. The full scale numerical implementation will require a fine mesh of the same size as the wellbore in the wellbore vicinity, and can easily become computationally prohibitive for 3D simulations, especially when considering well testing applications. However analytic models have limited application since they are based on simplified reservoir properties and cannot easily account for the complexity of realistic reservoirs. On the other hand, the method of decoupled overlapping grids is more robust; it captures the underlying reservoir heterogeneity and can be applied to any well configuration.

6.3 Model equations

For a single-phase slightly compressible fluid (ignoring gravity effects and density change), we have the following global and local equations:

Global problem

$$\phi c_t \frac{\partial p_{\text{ls}}}{\partial t}(\mathbf{x},t) = \nabla \cdot \left(\frac{\mathbf{k}}{\mu} \nabla p_{\text{ls}}(\mathbf{x},t) \right) + \int_\gamma q_l(\boldsymbol{\gamma},t)\delta(\mathbf{x}-\boldsymbol{\gamma})\, d\gamma \qquad \text{in } \Omega \times (0,T] \tag{6.1a}$$

$$\mathbf{n} \cdot \left(\frac{\mathbf{k}}{\mu} \nabla p_{\text{ls}}(\mathbf{x},t) \right) = 0 \qquad \text{in } \partial\Omega \times (0,T] \tag{6.1b}$$

$$p_{\text{ls}}(\mathbf{x},0) = 0 \qquad \text{in } \Omega \tag{6.1c}$$

Local problem

$$\phi c_t \frac{\partial p_{\text{fw}}}{\partial t}(\mathbf{x},t) = \nabla \cdot \left(\frac{\mathbf{k}}{\mu} \nabla p_{\text{fw}}(\mathbf{x},t) \right) \qquad \text{in } \Gamma \times (0,T] \tag{6.2a}$$

$$\mathbf{n} \cdot \left(\frac{\mathbf{k}}{\mu} \nabla p_{\text{fw}}(\mathbf{x},t) \right) = \frac{q_l(\mathbf{x},t)}{2\pi} \qquad \text{in } \partial\Gamma_w \times (0,T] \tag{6.2b}$$

$$p_{\text{fw}}(\mathbf{x},t) = p_{\text{ls}}(\mathbf{x},t) \qquad \text{in } \partial\Gamma_o \times (0,T] \tag{6.2c}$$

$$p_{\text{fw}}(\mathbf{x},0) = 0 \qquad \text{in } \Gamma \tag{6.2d}$$

where p_{ls} and p_{fw} are the pressure drawdowns for the line source and finite radius wellbore solutions respectively, $\boldsymbol{\gamma}$ represents the path of the line source, and q_l is the production/injection rate per unit well length.

6.4 Framework for analytic solutions

In this section we outline a framework for computing an analytic solution of the line source problem starting from a one-dimensional instantaneous point source solution. For references see [18, 44, 52].

6.4.1 Instantaneous point source solution

The instantaneous point source problem in an infinite one-dimensional domain is:

$$p_t = \eta p_{xx}, \qquad -\infty < x < \infty, \tag{6.3a}$$

$$p(x, t=0) = q\delta(x - x^*), \tag{6.3b}$$

$$p(x \to \pm\infty, t) = 0, \tag{6.3c}$$

($\eta = k/(\phi c_t \mu)$) which has the standard solution:

$$p(x,t) = q p_1(x,t;x^*) = \frac{q}{\sqrt{4\pi\eta t}} e^{-(x-x^*)^2/(4\eta t)}. \tag{6.4}$$

The 3D analogue to (6.4) for an instantaneous point source of strength q at (x^*, y^*, z^*) is [18, p.256]:

$$p(x,y,z,t) = \frac{q}{8(\pi\eta t)^{\frac{3}{2}}} \exp\left(-\frac{(x-x^*)^2+(y-y^*)^2+(z-z^*)^2}{4\eta t}\right), \tag{6.5a}$$

$$= q p_1(x,t;x^*) p_1(y,t;y^*) p_1(z,t;z^*). \tag{6.5b}$$

The method of images is used to account for the effects of boundaries. For $x \in [0, x_e]$ with a point source of unit strength at x^* and Neumann boundary conditions, the instantaneous point source solution is

$$p_1(x,t;x^*) = \frac{1}{\sqrt{4\pi\eta t}} \sum_{n=-\infty}^{\infty} e^{-(x-x^*+2nx_e)^2/(4\eta t)} + e^{-(x+x^*+2nx_e)^2/(4\eta t)}. \tag{6.6}$$

An equivalent Fourier series form of (6.6) can be derived from Poisson's summation formula [18, p.275] to get:

$$p_1(x,t;x^*) = \frac{1}{x_e}\left[1 + 2\sum_{n=1}^{\infty} \exp\left(-\frac{\eta n^2\pi^2}{x_e^2}t\right) \cos\frac{n\pi x}{x_e} \cos\frac{n\pi x^*}{x_e}\right]. \tag{6.7}$$

(6.6) is quicker to converge for short time and (6.7) is quicker to converge for long time.

Similarly to (6.5), the solution in a box of dimensions $x_e \times y_e \times z_e$ due to an instantaneous point source of unit strength at (x^*, y^*, z^*) is then

$$p_{\text{inst}}(x,y,z,t;x^*,y^*,z^*) = p_1(x,t;x^*) p_1(y,t;y^*) p_1(z,t;z^*), \tag{6.8}$$

where p_1 is given by (6.6) or (6.7).

6.4.2 Time-dependent point source solution

If the source term at $\mathbf{x}^* = (x^*, y^*, z^*)$ is $q(t)$ per unit time at time t, then the solution at $\mathbf{x} = (x, y, z)$ at time t is

$$p_{\text{cont}}(\mathbf{x}, t; \mathbf{x}^*) = \int_0^t q(\tau) p_{\text{inst}}(\mathbf{x}, t-\tau; \mathbf{x}^*)\, d\tau. \tag{6.9}$$

6.4.3 Time-dependent line source solution

If the source term is a line source of strength $q_l(\boldsymbol{\gamma}, t)$ per unit length per unit time, the solution at (x, y, z) at time t is obtained by integrating in time and along the path $\boldsymbol{\gamma}$:

$$p_{ls}(\mathbf{x}, t) = \int_{\gamma} \int_{0}^{t} q_l(\boldsymbol{\gamma}, \tau) p_{\text{inst}}(\mathbf{x}, t - \tau; \boldsymbol{\gamma}) \, d\tau \, d\gamma. \tag{6.10}$$

Equation (6.10) gives a closed form analytic solution for the line source problem (6.1). In some situations this solution can only be approximated numerically giving rise to a semi-analytic formulation.

6.5 Description of case study

A schematic diagram of the case study is shown in Figure 6.1. The global domain, shown in Figure 6.1(a), is a homogeneous rectangular domain of dimensions x_e, y_e, z_e. The horizontal well is placed parallel to the x-axis. The local post-process domain, shown in Figure 6.1(b), is a cylinder which has external boundary data interpolated from the solution of the global problem, and an internal boundary representing the wellbore. This cylinder is extended a distance L_{ext} beyond ends of the wellbore to prevent measuring (interpolating) the boundary data for the local problem at the well surface. The flow rate of the extended wellbore section is set to zero.

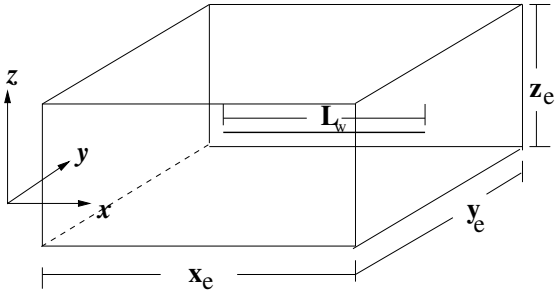

(a) Global problem

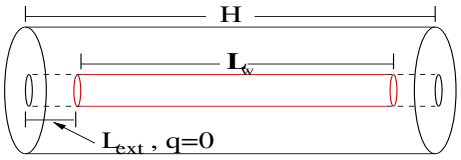

(b) Local problem

Figure 6.1: Schematic representation of horizontal well case study.

This case study satisfies the conditions stated in Section 3.1 for the reduction of the local problem to a 2D problem by taking the average in the angular direction. Also a coordinate transformation

$$r \to \ln r \stackrel{\text{def}}{=} R$$

is applied to give a refined grid near the wellbore. Hence we solve the following equations in the local domain:

$$\frac{\phi\mu c_t}{k}\frac{\partial p}{\partial t} = e^{-2R}\frac{\partial^2 p}{\partial R^2} + \frac{\partial^2 p}{\partial x^2} \qquad \text{in } \Gamma \times (0,T] \tag{6.11a}$$

$$p(R_e, x, t) = p_E(x,t) \qquad \text{along the cylinder body} \tag{6.11b}$$

$$p(R, x_B, t) = p_B(R,t) \qquad \text{at the bottom cylinder face} \tag{6.11c}$$

$$p(R, x_T, t) = p_T(R,t) \qquad \text{at the top cylinder face} \tag{6.11d}$$

$$p(R,0) = 0 \qquad \text{in } \Gamma \tag{6.11e}$$

together with the equations for the boundary condition at the wellbore. The parameters (k, μ, c_t, ϕ) are set to 1 for the case study.

We will investigate two classical models for the boundary condition at the wellbore: the uniform flux condition and the uniform pressure (or infinite con-

ductivity) condition. For the uniform flux condition the flow rate per unit well length is assumed constant. This induces a non-uniform pressure distribution along the wellbore. For the infinite conductivity model the pressure along the wellbore is assumed constant thereby inducing a non-uniform flow rate along the wellbore.

The uniform flux and uniform pressure conditions are simplifications, and a more realistic representation would incorporate flow within the wellbore, for example by modelling pressure drop within the wellbore due to frictional and gravitational effects. Such models are often referred to as finite conductivity models (see [75, 86, 98, 102]). The same principle for the application of the decoupled overlapping grids method discussed in this chapter applies to these models as well.

6.6 Uniform flux solution

For the uniform flux problem the following extra condition is defined for (6.11) at the wellbore:

$$\frac{\partial p}{\partial R} = -\frac{q\mu}{2\pi k L_w} \qquad \text{at } \partial\Gamma_w \times (0, T] \,. \tag{6.12}$$

where L_w is the length of the well. Simulation parameters are listed in Table 6.1.

(x_e, y_e, z_e)	(1, 1, 0.3)
L_w	0.4
(y_w, z_w)	$(y_e/2,\ z_e/2)$
r_w	10^{-3}
t	$10^{-3} : 10^{2}$
q	1

Table 6.1: Simulation parameters. r_w = well radius, (y_w, z_w) = well coordinates in the y–z plane.

6.6.1 Computing the semi-analytic solution

Since $q = 1$, the analytic line source solution for the global problem is (from (6.10))

$$p_{ls}(\mathbf{x}, t) = \frac{1}{L_w} \int_0^t \int_\gamma p_{\text{inst}}(\mathbf{x}, t - \tau; \boldsymbol{\gamma})\, d\tau\, d\gamma, \tag{6.13}$$

where p_{inst} given in (6.8) is evaluated using (6.6) for early time and (6.7) for late time.

Since the line source is parallel to the x-axis, the x-component of p_{inst} can be analytically integrated along the line source, so that we have

$$p_{ls}(\mathbf{x}, t) = \frac{1}{L_w} \int_0^t F_1(x, t - \tau) p_1(y, t - \tau, y^*) p_1(z, t - \tau, z^*)\, d\tau, \tag{6.14}$$

where for the method of images solution,

$$F_1(x,t) = \frac{1}{2} \sum_{n=-\infty}^{\infty} \left[-\text{erf}\, \frac{x - x_b + 2nx_e}{2\sqrt{t}} + \text{erf}\, \frac{x - x_a + 2nx_e}{2\sqrt{t}} \right] + \left[\text{erf}\, \frac{x + x_b + 2nx_e}{2\sqrt{t}} - \text{erf}\, \frac{x + x_a + 2nx_e}{2\sqrt{t}} \right], \tag{6.15a}$$

and for the Fourier series solution,

$$F_1(x,t) = \frac{1}{x_e} \left[x_b - x_a + 2 \sum_{n=1}^{\infty} \frac{x_e}{n\pi} \exp\left(-\frac{\kappa n^2 \pi^2}{x_e^2} t \right) \left(\sin \frac{n\pi x_b}{x_e} - \sin \frac{n\pi x_a}{x_e} \right) \cos \frac{n\pi x}{x_e} \right], \tag{6.15b}$$

with the line source path $\gamma \in [x_a, x_b]$.

The simulation time $t \in [0, T]$ is divided into early, intermediate, and late time intervals ending at t_1, t_2 and T respectively. For early time $0 \le t \le t_1$, $p_{ls}(\mathbf{x}, t)$ is calculated from (6.13) with $F_1(x, t - \tau)$ given by (6.15a). For intermediate time $t_1 < t \le t_2$, we have

$$p_{ls}(\mathbf{x}, t) = p_{ls}(\mathbf{x}, t_1) + \frac{1}{L_w} \int_{t_1}^t F_1(x, t - \tau) p_1(y, t - \tau, y^*) p_1(z, t - \tau, z^*)\, d\tau, \tag{6.16}$$

where $p_{ls}(\mathbf{x}, t_1)$ is the early time solution, and $F_1(x, t - \tau)$ above is given by

(6.15b). For late time $t_2 \gg \max(x_e^2, y_e^2, z_e^2)$, p_{inst} in (6.8) has an effective value of $1/(x_e y_e z_e)$. Therefore we have

$$p_{ls}(\mathbf{x}, t) = p_{ls}(\mathbf{x}, t_2) + \frac{(t - t_2)}{(x_e y_e z_e)}, \quad t_2 < t \leq T, \tag{6.17}$$

where $p_{ls}(\mathbf{x}, t_2)$ is calculated from (6.16), and the last term on the RHS of (6.17) is from integrating (6.13) with $p_{\text{inst}} = 1/(x_e y_e z_e)$.

The time integral in (6.14) is computed numerically using an adaptive quadrature code that implements a Gauss-7 Kronod-15 quadrature rule [92]. The simulation time is divided into sub-intervals and numerical time integration is performed on each subinterval. The results are then added up cumulatively to get the pressure history.

We determine a suitable time to switch from the method of images solution to the Fourier series solution and from this to the long time solution by comparing the results from these methods at the combination of points listed in Table 6.2. Firstly Figure 6.2(a) shows the convergence of the analytic solution when the number of images and Fourier terms is doubled from 8 to 16. It shows that the error in using 8 instead of 16 images is less than 10^{-10} for times t_D up to 1, and the error in using 8 instead of 16 Fourier terms is less than 10^{-10} for times t_D from 0.2 onwards. Secondly Figure 6.2(b) shows the absolute difference in the method of images and Fourier series solutions, and the Fourier series and long time solution in (6.17) on each time subinterval. Based on Figure 6.2, 8 images and Fourier series terms are used to compute the semi-analytic solution, and the switch time from the method of images solution to the Fourier series solution is chosen at $t_D = 0.5$, and from Fourier series solution to the long time solution is at $t_D = 10$.

x	0, 0.125, 0.25, 0.375, 0.5
y	0.5
z	0.151, 0.12, 0.28

Table 6.2: Measurement points for Figure 6.2

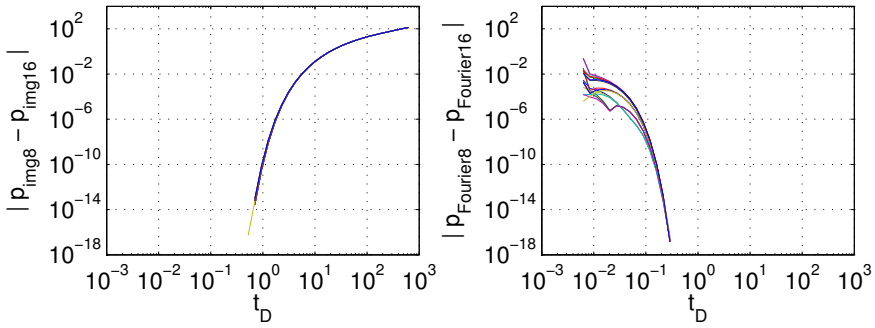

(a) Convergence of method of images (left) and Fourier series (right) solutions.

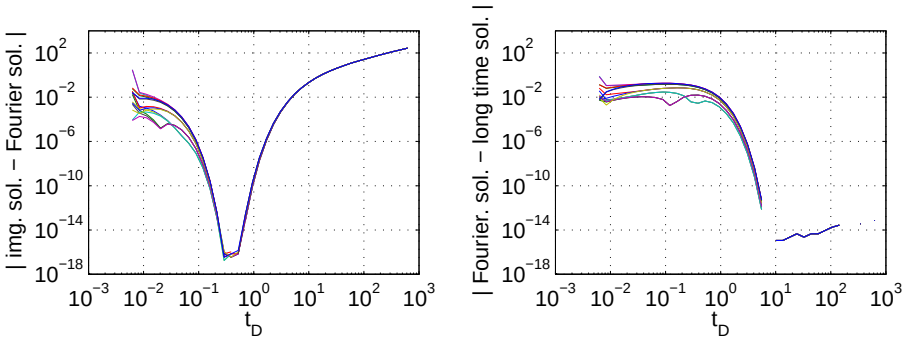

(b) Switching from method of images to Fourier solution (left) and Fourier to long time solution (right). $N_{\text{img}} = 8$, $N_{\text{Fourier}} = 8$.

Figure 6.2: Absolute error in dimensionless pressure on the sub-intervals of time integration. $t_D = kt/(\phi\mu c_t L_w^2)$

6.6.2 Computing the numerical solution

The vertex-centred finite volume method is used to compute the numerical solution of the global and local problems. The global mesh is constructed so that points representing the line source coincide with computation nodes.

Based on the guideline for selecting the local domain mesh size for 2D simulations suggested in Chapter 3, the local mesh is generated such that $\Delta r_{\max} = h/2$, where h is the average mesh size for the global problem. In addition the mesh spacing in the R-x directions is kept fairly uniform.

6.6.3 Comparison of numerical and semi-analytic solutions

Refn. Level	0	1
d.o.f	3087	21853
h	0.05	0.025

Table 6.3: First stage mesh properties

r_e	L_{ext}	*d.o.f for Refn. levels*		
			$(\Delta r_{\max} = h/2)$	$(\Delta r_{\max} = h/4)$
		0	*1*	*0*
0.05	0.05	102	518	518
	0.15	126	630	630
0.1	0.05	289		
	0.15	357		

Table 6.4: Second stage mesh properties

Mesh properties for the global and local stage simulations are listed in Table 6.3 and Table 6.4.

Figure 6.3 – Figure 6.6 show the absolute difference in the semi-analytic and numerical solutions. x_w represents position along the wellbore length and x_E represents position along the axial boundary of the cylinder, which extends a length L_{ext} beyond each end of the wellbore. The simulation time for each line is given by the corresponding value in the legend multiplied by 10^{-1}. The plots show that the error goes through an initial transient phase before settling to a steady-state distribution. The errors measured at the cylinder face (third column) are highest close to the wellbore and decrease with distance away from the wellbore as expected.

The plots for the error along the wellbore (first column) and the axial boundary of the cylinder (second column) show that the error rises sharply close to the toe and heel of the wellbore. This is primarily due to the inadequacy of the linear approximation used in the discrete equations in capturing the steep pressure gradients at the ends of the wellbore (see Figure 6.7). For the coarse grid simulations shown in Figure 6.3 and Figure 6.4, it is seen that increasing L_{ext} leads to a noticeable decrease in the error at the toe and heel of the wellbore. However for the fine grid simulations in Figure 6.5 and Figure 6.6, increasing L_{ext} does not have a significant effect on the error along the wellbore. Figure 6.7 shows that in the cases where increasing L_{ext} has more effect, the steep profile at the ends of the wellbore is crudely approximated.

Neglecting the peaks in the error at the ends of the of the wellbore, the maximum error along the wellbore length (which occurs halfway along the wellbore length) is less than, or at least within the same order of magnitude, as the maximum error along the axial boundary of the local domain. This is consistent with the observations made in the Chapter 3 for fully penetrating vertical wells in a homogeneous domain, where the maximum error in the the average wellbore pressure is bounded above by the maximum error in the average external boundary pressure of the post-process domain for $\Delta r_{\max} \leq h/2$.

Comparing the base case in Figure 6.3 to the plots in Figure 6.5–Figure 6.6 and neglecting the peaks in error at the ends, it is seen that the maximum wellbore error (which occurs at the centre of the wellbore) is improved when the underlying global grid is refined (Figure 6.5), or when the post-process domain is increased (Figure 6.4), but not when the local mesh size $\Delta r_{\max}$ is reduced from $h/2$ to $h/4$ (Figure 6.6). Of the improved results, Figure 6.4 (coarse underlying global grid and larger r_e) requires fewer degrees of freedom compared to Figure 6.6 (fine underlying global grid and smaller r_e), as seen in Table 6.3 and Table 6.4.

Overall the simulations show a good agreement between the numerical and semi-analytic solutions. The relative peak error at the ends of the wellbore is less than 8% in all the simulations, and the relative maximum error occurring midway along the well length is less than 3% in all the simulations.

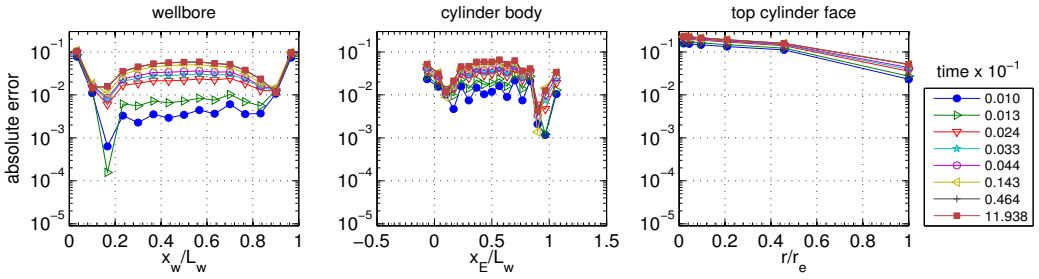

(a) $L_{\text{ext}} = 0.05$

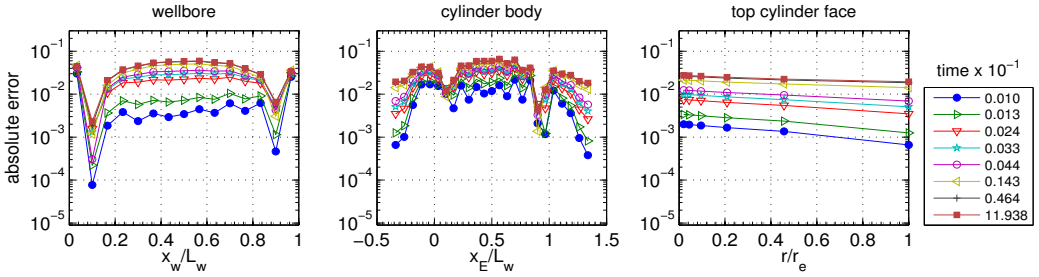

(b) $L_{\text{ext}} = 0.15$

Figure 6.3: Time profile of absolute error for Refn. Level 0, $r_e = 0.05$.

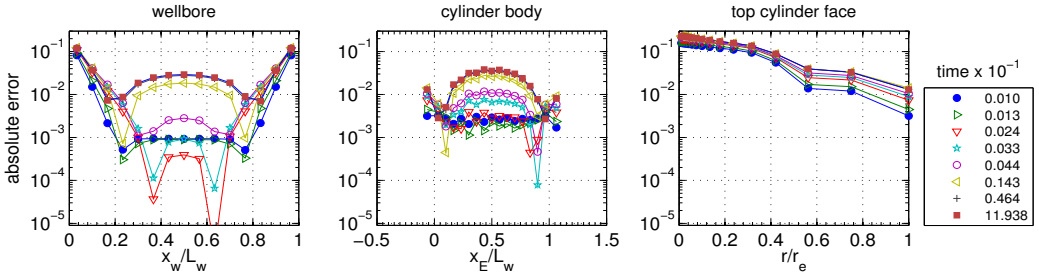

(a) $L_{\text{ext}} = 0.05$

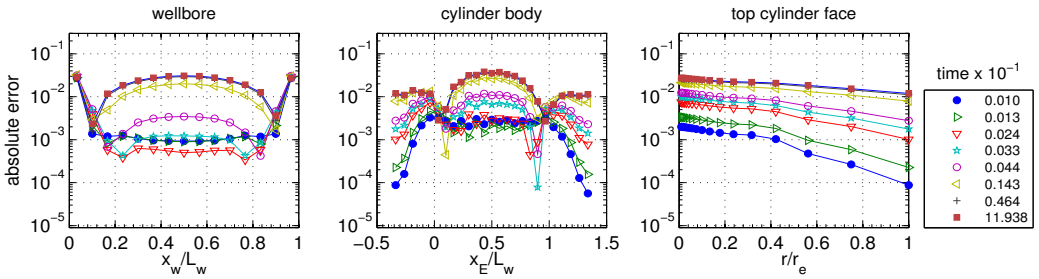

(b) $L_{\text{ext}} = 0.15$

Figure 6.4: Time profile of absolute error for Refn. Level 0, $r_e = 0.1$.

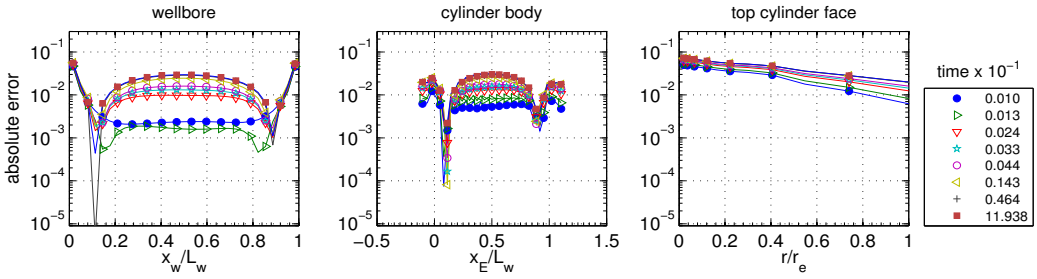

(a) $L_{\text{ext}} = 0.05$

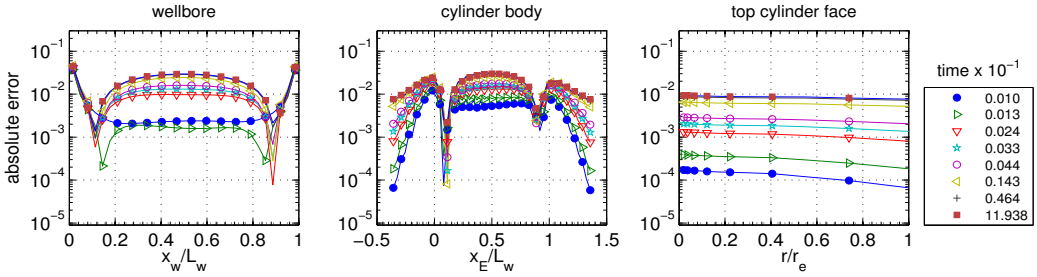

(b) $L_{\text{ext}} = 0.15$

Figure 6.5: Time profile of absolute error for Refn. Level 1, $r_e = 0.05$.

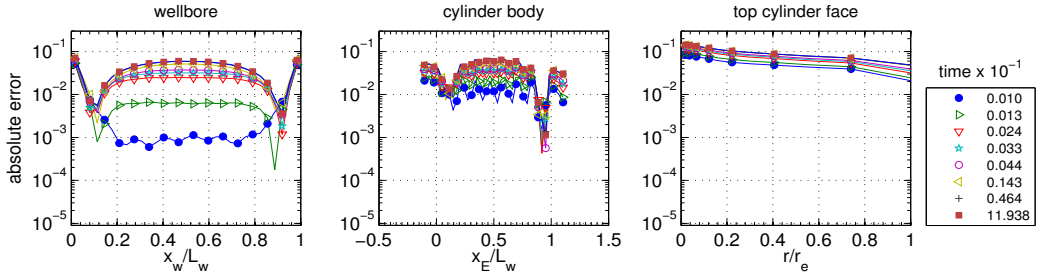

(a) $L_{\text{ext}} = 0.05$

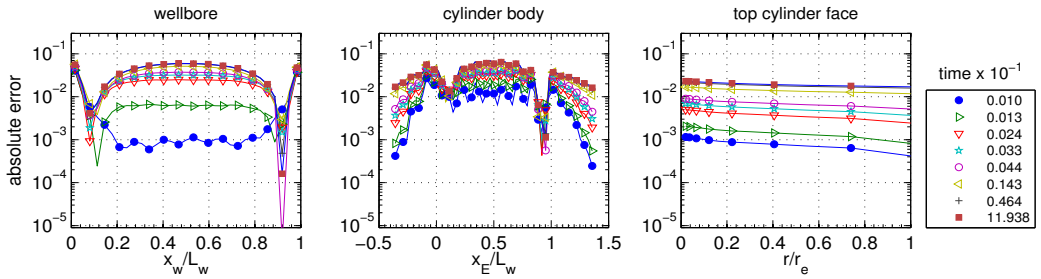

(b) $L_{\text{ext}} = 0.15$

Figure 6.6: Time profile of absolute error for $\Delta r_{\max} = h/4$, Refn. Level 0, $r_e = 0.05$.

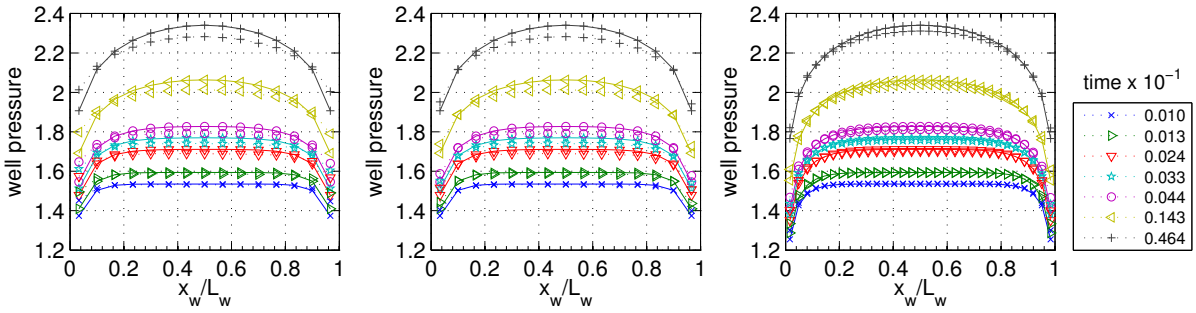

Figure 6.7: Pressure along wellbore. $r_e = 0.05$. L→R: Figure 6.3(a), Figure 6.3(b), Figure 6.6(a). Dotted line: numerical solution, Bold line: analytic solution.

6.7 Uniform pressure solution

For the uniform pressure problem, a second constraint is required in addition to the uniform pressure constraint for both global and local problems. This constraint can either be a specified total flow rate at the wellbore or specified wellbore pressure. We implement the total flow rate condition in this section. Therefore the following extra conditions are defined at the wellbore:

$$p(\mathbf{x}, t) = p_w(t), \tag{6.18a}$$

$$q(t) = \int_\gamma q_l(\gamma, t)\, d\gamma, \tag{6.18b}$$

Here γ represents the line source path for the global problem, or the wellbore surface for the local problem. Simulation parameters are listed in Table 6.5.

(x_e, y_e, z_e)	$(1,\ 1,\ 0.3)$
L_w	0.4
(y_w, z_w)	$(y_e/2,\ z_e/2)$
r_w	10^{-3}
t	$10^{-4} : 1$
q	0.4

Table 6.5: Simulation parameters. r_w = well radius, (y_w, z_w) = well coordinates in the y–z plane.

6.7.1 Computing the semi-analytic solution

The semi-analytic solution is obtained by solving the following equations:

$$p_{ls}(\mathbf{x},t) = \int_\gamma \int_0^t q_l(\boldsymbol{\gamma},\tau) p_{\text{inst}}(\mathbf{x}, t-\tau;\boldsymbol{\gamma})\, d\tau\, d\gamma, \tag{6.19a}$$

$$q(t) = \int_\gamma q_l(\gamma,t)\, d\gamma, \tag{6.19b}$$

where both the pressure p_{ls} and well flow rate per unit length q_l are unknown. We implement a technique that is often found in the literature for approximating (6.19) (see for instance [52, 54, 75, 86, 87]). The well is divided into N_{seg} equal length segments, each having uniform flux per unit length equal to q_{l,w_i}. The uniform pressure condition is then enforced by equating the pressure drops at the midpoints of the segments. This gives $N_{\text{seg}}-1$ equations, and the last equation comes from the total constant rate constraint. Hence the following set of equations are solved to get q_{l,w_i}:

$$p_{ls}(\mathbf{x}_{w_i},t) = p_{ls}(\mathbf{x}_{w_{i+1}},t), \qquad i = 1 \ldots N_{\text{seg}}-1, \tag{6.20a}$$

$$q(t) = \sum_{i=1}^{N_{\text{seg}}} q_{l,w_i}(t) L_{w_i}, \tag{6.20b}$$

where $p_{ls}(\mathbf{x}_{w_i},t)$, the pressure on well segment i, is given by

$$p_{ls}(\mathbf{x}_{w_i},t) = \int_0^t \left[\sum_{j=1}^{N_{\text{seg}}} q_{l,w_j}(\tau) S_j(\mathbf{x}_{w_i}, t-\tau) \right] d\tau \tag{6.21}$$

$$\text{for} \qquad S_j(\mathbf{x}_{w_i},t) = \int_{w_j} p_{\text{inst}}(\mathbf{x}_{w_i},t;\boldsymbol{\gamma})\, d\gamma, \tag{6.22}$$

L_{w_i} is the length of well segment i, and p_{inst} is given by (6.8). Once q_{l,w_i} has been computed the pressure at any position $\mathbf{x}$ in the domain can be calculated from (6.21) replacing $\mathbf{x}_{w_i}$ with $\mathbf{x}$.

The solution of (6.20) involves the sequential computation of the convolution integral (6.21) at each time level. To eliminate this sequential time computation, we solve the problem in Laplace space. We implement the parabolic contour integration of the Bromwich integral proposed by Weideman and Trefethen [104]

to compute the inverse Laplace transform. The basic Iseger algorithm in Table 3.1 is not used here because the nature of the source term $S(\mathbf{x}, t)$ in (6.22) enforces the need for very small time steps to accurately invert the solution at early time.

Taking the Laplace transform of (6.20), we get:

$$\overline{p}_{ls}(\mathbf{x}_{w_i}, s) = \overline{p}_{ls}(\mathbf{x}_{w_{i+1}}, s), \qquad i = 1 \dots N_{\text{seg}} - 1, \tag{6.23a}$$

$$\overline{q}(s) = \sum_{i=1}^{N_{\text{seg}}} \overline{q}_{l,w_i}(s) L_{w_i}, \tag{6.23b}$$

where

$$\overline{p}_{ls}(\mathbf{x}_{w_i}, s) = \sum_{j=1}^{N_{\text{seg}}} \overline{q}_{l,w_j}(s) \overline{S}_j(x_{w_i}, s). \tag{6.24}$$

To simplify the calculation of the Laplace transform of the source term $\overline{S}_j(x_{w_i}, s)$, the integration in (6.22) is performed using the midpoint rule. Therefore

$$\overline{S}_j(x_{w_i}, s) = L_{w_j} \overline{p}_{\text{inst}}(\mathbf{x}_{w_i}, s; \mathbf{x}_j) \tag{6.25}$$

for $\mathbf{x}_j$ the midpoint of line segment j.

The flux distribution is uniform initially, but undergoes a transition period before reaching a steady-state distribution along the wellbore. Therefore we use the form of p_{inst} given by the method of images in (6.6), which is more accurate and quick to converge at early time, to compute the transient flux distribution. From (6.8) and (6.6)

$$p_{\text{inst}}(\mathbf{x}, t; \mathbf{x}^*) = p_1(x, t; x^*) p_1(y, t; y^*) p_1(z, t; z^*), \tag{6.26}$$

$$p_1(x, t; x^*) = \frac{1}{\sqrt{4\pi\eta t}} \sum_{n=-\infty}^{\infty} e^{-(x - x^* + 2nx_e)^2/(4\eta t)} + e^{-(x + x^* + 2nx_e)^2/(4\eta t)}. \tag{6.27}$$

Let

$$X_{1n} = (x - x^* + 2nx_e)^2, \quad X_{2n} = (x + x^* + 2nx_e)^2, \tag{6.28}$$

and $Y_{1n}, Y_{2n}, Z_{1n}, Z_{2n}$ be defined similarly. Then

$$p_{\text{inst}}(\mathbf{x}, t; \mathbf{x}^*) = \frac{1}{(\sqrt{4\pi\eta t})^3} \sum_{n=-\infty}^{\infty} \sum_{m=-\infty}^{\infty} \sum_{p=-\infty}^{\infty} \left[\sum_{i=1}^{2} \sum_{j=1}^{2} \sum_{k=1}^{2} \exp\left(-\frac{X_{in} + Y_{jm} + Z_{kp}}{4\eta t} \right) \right], \tag{6.29}$$

and so

$$\overline{p}_{\text{inst}}(\mathbf{x}, s; \mathbf{x}^*) = \frac{1}{4\pi\eta} \sum_{n=-\infty}^{\infty} \sum_{m=-\infty}^{\infty} \sum_{p=-\infty}^{\infty} \Bigg[\sum_{i=1}^{2} \sum_{j=1}^{2} \sum_{k=1}^{2} \frac{1}{\sqrt{X_{in} + Y_{jm} + Z_{kp}}} \exp\left(-\frac{1}{\eta} \sqrt{s(X_{in} + Y_{jm} + Z_{kp})} \right) \Bigg], \tag{6.30}$$

since

$$\mathcal{L}\left[\frac{1}{t\sqrt{t}} \exp(-a/t) \right] = \sqrt{\frac{\pi}{a}} \exp(-2\sqrt{as}), \quad a > 0\,. \tag{6.31}$$

6.7.2 Computing the numerical solution

The vertex-centred finite volume method is used to compute the numerical solution of the global and local problems. Discretisation in space yields the following system of differential-algebraic equations:

$$\dot{\underline{p}} = A\underline{p} + B\underline{q}_l, \tag{6.32a}$$

$$\underline{0} = C\underline{p} + D\underline{q}_l + \underline{q}, \tag{6.32b}$$

with the vectors

$$\underline{p} = [p_{11}\ p_{12}\ \ldots\ p_{mn}]^T, \quad \underline{q}_l = [q_{l_1}\ q_{l_2}\ \ldots\ q_{l_{N_w}}]^T, \quad \underline{q} = [0\ 0\ \ldots\ q(t)]^T.$$

A is the discretisation matrix for the Laplacian operator, and matrix B accounts for the location of line source term in (6.1) for the global solution, and finite radius well source term in (6.2) for the local solution. In the global simulation, the points representing the line source are constrained to coincide with computation nodes. The uniform pressure condition in (6.18a) is implemented in the first $N_w - 1$ rows of the matrices C and D. These matrices ensure that points $p_{w_i} \in \underline{p}$ that make

up the source term satisfy

$$p_{w_i} = p_{w_{i+1}} \qquad \Rightarrow \qquad \dot{p}_{w_i} - \dot{p}_{w_{i+1}} = 0\,; \qquad i = 1 \ldots N_w - 1. \tag{6.33}$$

The N_wth row of C contains zeros, while the N_wth row of D contains the well segment lengths L_{w_j} so that, from (6.18b),

$$q(t) = \sum_{i=1}^{N_w} q_{l_j} L_{w_j}. \tag{6.34}$$

6.7.3 Comparison of numerical and semi-analytic solutions

Refn. Level	0	1
d.o.f	1125	7569
h	0.0726	0.0363

Table 6.6: First stage mesh properties.

r_e	L_{ext}	*d.o.f for Refn. Levels*		
		($\Delta r_{\max} = h/2$)		($\Delta r_{\max} = h/4$)
		0	*1*	*0*
0.05	0.05	60	252	252
	0.15	82	360	360
0.1	0.05	165		
	0.15	132		

Table 6.7: Second stage mesh properties.

Mesh properties for the global and local stage simulations are listed in Table 6.6 and Table 6.7. The semi-analytic solution is plotted in Figure 6.8 and the numerical solutions are shown in Figure 6.9 – Figure 6.12. The simulation time for each line is given by the corresponding value in the legend multiplied by 10^{-2}.

In Figure 6.8 the semi-analytic solution has been calculated on 32, 64 and 128 equal length segments. It is seen that initially the flux is uniform and then the curve develops sharp peaks at the ends. As the number of segments used in the approximation is increased from 32 to 64 to 128, the steepness of the flux at the ends of the well becomes more pronounced. There is also a noticeable difference in the pressure values calculated in these cases. We expect that the calculated pressure values are more accurate as the number of segments is increased.

The pressure results for the decoupled overlapping grids method shown in

Figures 6.9 – 6.12 do not vary much for the different test cases. In addition, these pressure values are close to those of the analytic solution on 128 segments shown in Figure 6.8. Significantly less time was needed to compute the numerical solution compared to the analytic solution on 128 well segments.

By comparing the wellbore flux calculated for $L_{\text{ext}} = 0.05$ and $L_{\text{ext}} = 0.15$ in Figures 6.9 – 6.12, it is seen that the effect of increasing L_{ext} on the wellbore flux is noticeable only for the results shown in Figure 6.10, that is, refinement level 0 and $r_e = 0.1$. For the rest of the computations, which were carried out with $r_e = 0.05$, increasing L_{ext} does not have a pronounced effect.

Comparing the coarse grid approximations in Figure 6.9 and Figure 6.10, it is seen that increasing the external radius of the local domain from $r_e = 0.05$ to 0.1 leads to a more U-shaped steady-state wellbore flux profile. The fine grid approximations in Figure 6.11 and Figure 6.12 have the same degrees of freedom for the local simulation but the boundary conditions are interpolated from different refinement levels of the underlying global mesh. It is seen that the shape of the wellbore flux in Figure 6.11, which has boundary data interpolated from refinement level 1, is closer to the analytic curves in Figure 6.8 compared to Figure 6.12, which has boundary data interpolated from refinement level 0. So the more accurate underlying grid solution results in a more accurate wellbore flux profile, as expected.

Ultimately the accuracy of the flux per unit length from the numerical computations depends on the grid resolution. A finer mesh is better able to capture the peaks at the ends of the wellbore. Another approach could be to use a non-uniform grid clustered towards the ends of the wellbore to get a better approximation of the steep flux variation here. We however note that the wellbore pressure values for all the test cases do not show a noticeable variation and are close to the analytic solution computed with 128 segments, suggesting that a good approximation of the pressure is obtained even on a crude mesh.

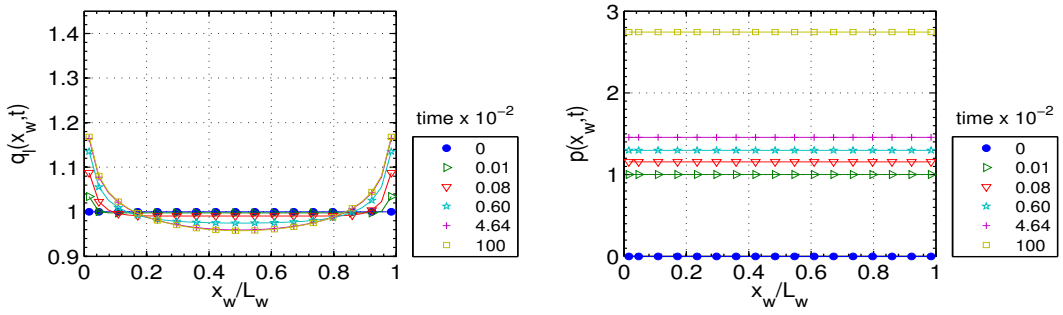

(a) 32 well segments

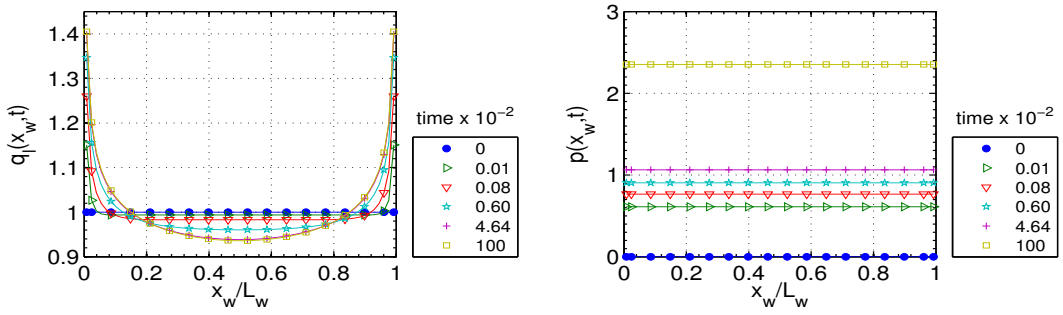

(b) 64 well segments

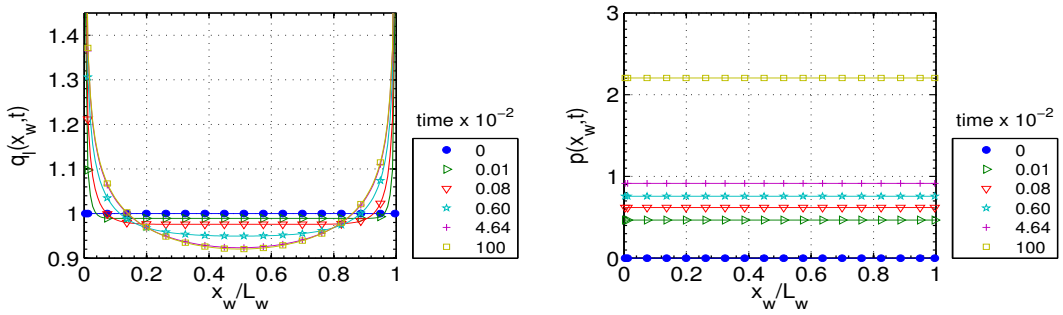

(c) 128 well segments

Figure 6.8: Semi-analytic solution. Well flow-rate per unit length (left) and well pressure (right).

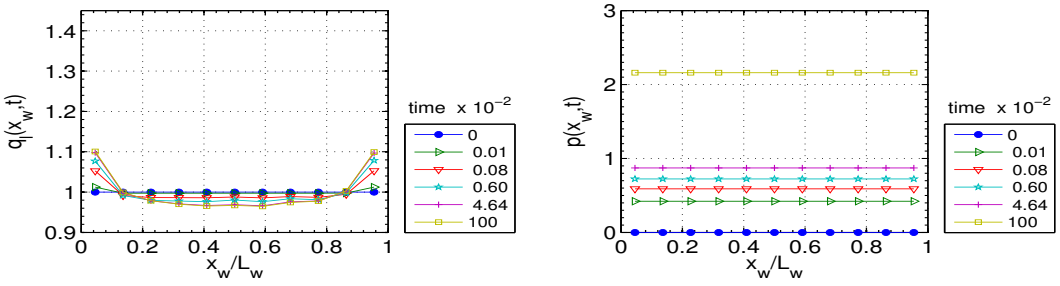

(a) $L_{\text{ext}} = 0.05$

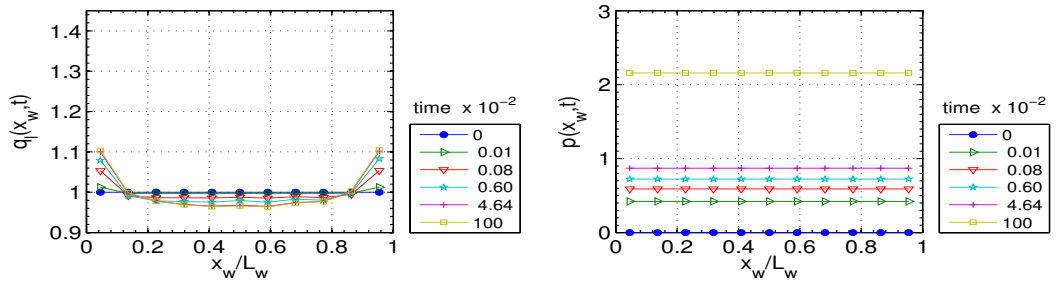

(b) $L_{\text{ext}} = 0.15$

Figure 6.9: Well flow-rate per unit length (left) and well pressure (right) for Refn. Level 0, $r_e = 0.05$.

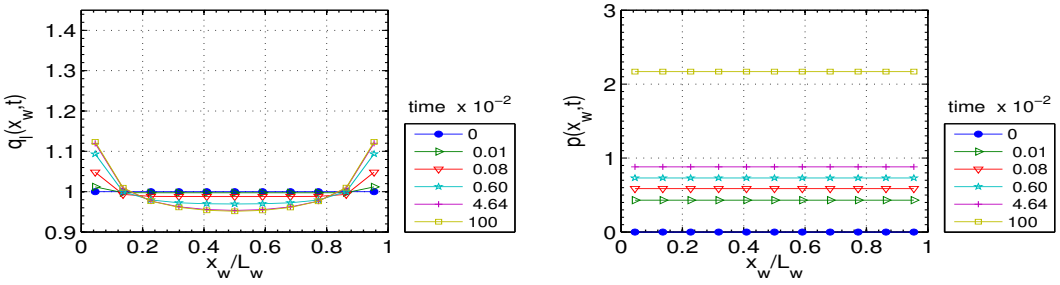

(a) $L_{\text{ext}} = 0.05$

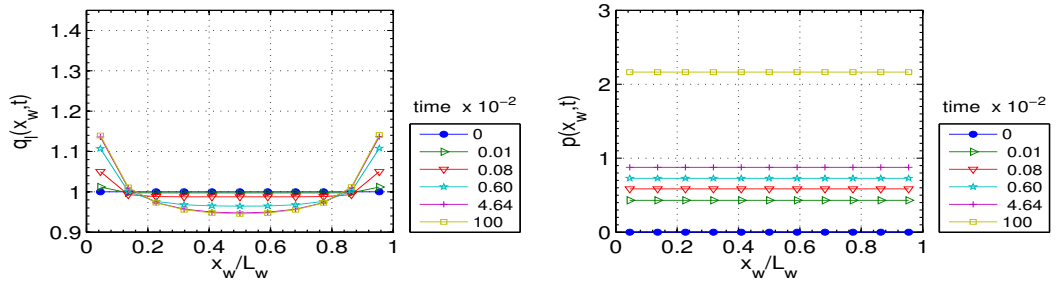

(b) $L_{\text{ext}} = 0.15$

Figure 6.10: Well flow-rate per unit length (left) and well pressure (right) for Refn. Level 0. $r_e = 0.1$.

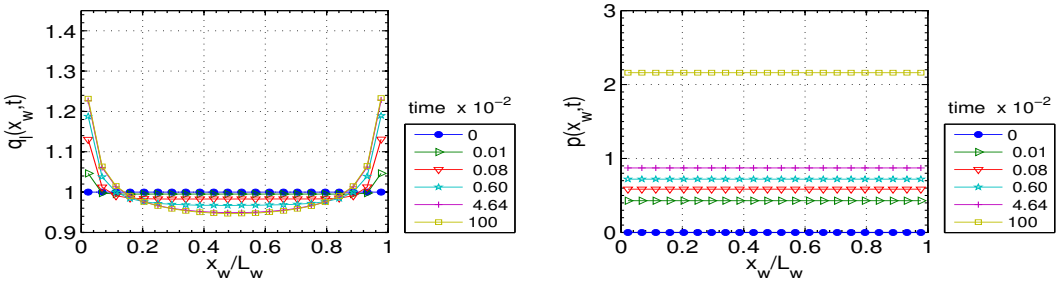

(a) $L_{\text{ext}} = 0.05$

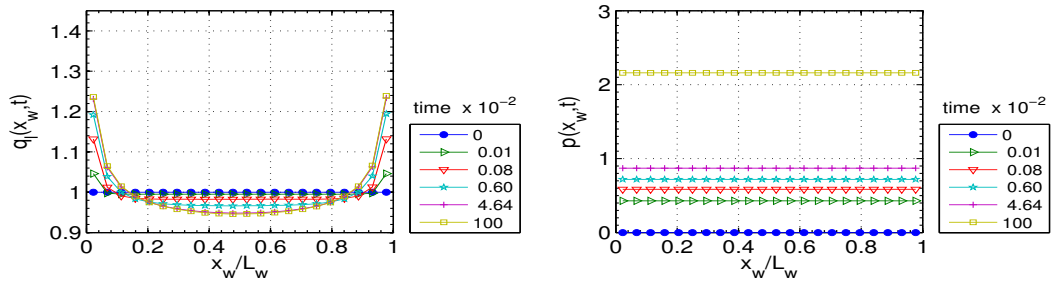

(b) $L_{\text{ext}} = 0.15$

Figure 6.11: Well flow-rate per unit length (left) and well pressure (right) for Refn. Level 1, $r_e = 0.05$.

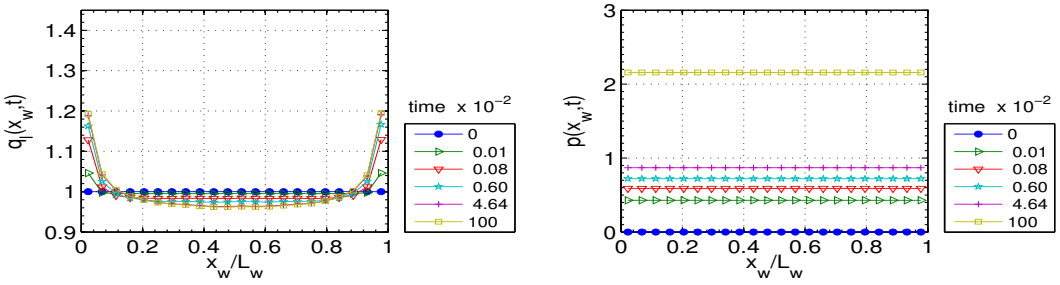

(a) $L_{\text{ext}} = 0.05$

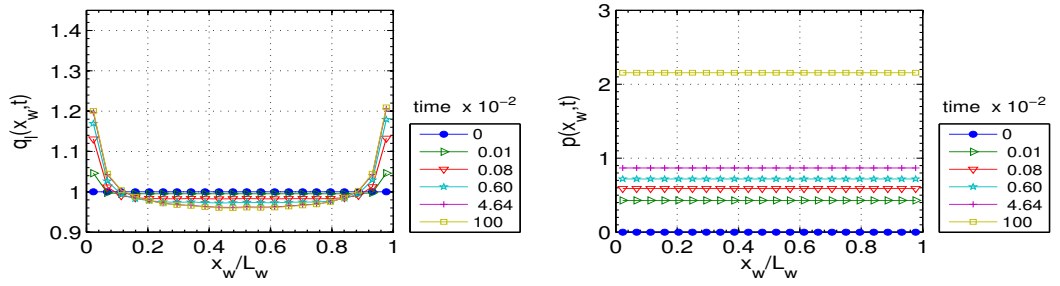

(b) $L_{\text{ext}} = 0.15$

Figure 6.12: Well flow-rate per unit length (left) and well pressure (right) for Refn. Level 0, $r_e = 0.05, \Delta r_{\max} = h/4$.

6.8 Slanted well

In this section we apply the decoupled overlapping grids method to investigate effect of rotation and elevation of a horizontal well in a homogeneous domain on well flow rate and wellbore pressure. The uniform pressure condition is implemented at the wellbore. The dimensions of the global domain are $(x_e, y_e, z_e) = (0.9, 0.9, 0.5)$, the radius for the local simulation $r_e = 0.1$, the well length $L_w = 0.4359$, and the extension beyond the well length in the local domain is $L_{\text{ext}} = 0.1$. The global simulations are carried out on a $17 \times 17 \times 17$ grid which is fairly uniform in the horizontal plane and non-uniform in the vertical plane: it is constructed to be more refined in the interval containing the line source. The mesh for the local stage is generated by setting $\Delta r_{\max} = h/4$.

Five different configurations of rotation and elevation are investigated. For case 1 the well is parallel to the x–axis and its centre is aligned with the centre of the global domain. With this configuration as the starting point the well is rotated by angle θ in the horizontal plane or ϕ in the vertical place to get case $2 - 4$ (see Figure 6.13). Case 5 shows results for an off-centre well; it has the same angles as case 4 but its centre is moved by 0.1 along the x–axis. Simulation results are plotted in Figure 6.14.

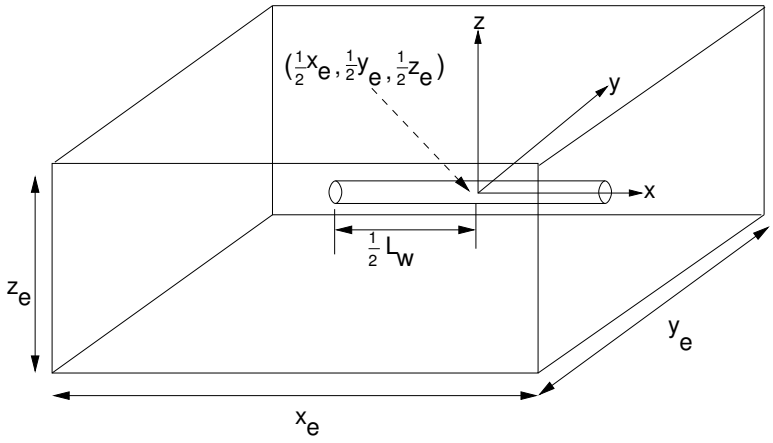

(a) Case 1. Well parallel to x–axis.

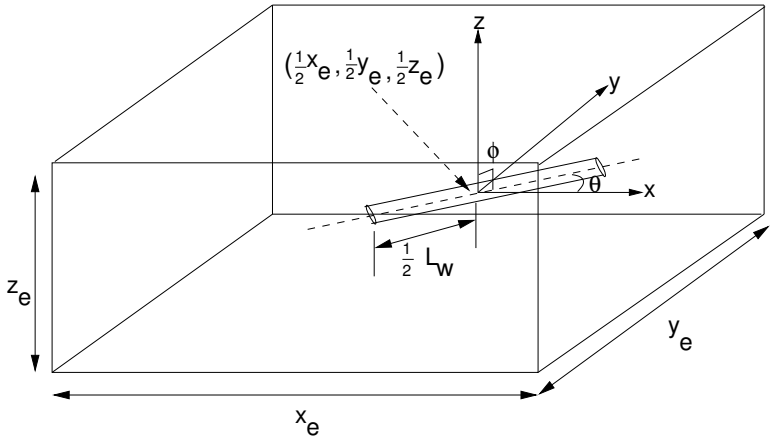

(b) Case 2. Rotation by θ in the horizontal plane.

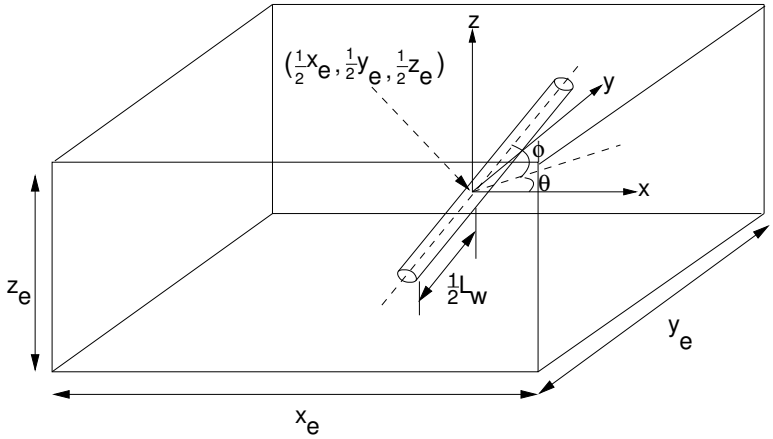

(c) Case 4. Rotation by θ in the horizontal plane and ϕ in the vertical plane.

Figure 6.13: Schematic representation of slanted well problem.

Comparison of case 1 with case 2 shows no observable change in the wellbore pressure or flux properties. On the other hand comparing case 1 to cases 3 – 4, a slight increase in the flux at the ends of the wellbore is observed. This is because given the length and position of the wellbore relative to the reservoir dimensions, the rotation in the vertical plane brings the ends of the wellbore closer to the reservoir boundaries compared with a rotation in the horizontal axis. Case 5 shows the impact of boundary effects on the wellbore flux distribution. At initial times before the boundary effects are felt, the flux distribution is symmetric along the length of the wellbore. At later times, the no-flow boundary conditions result in the top end of the well (which is closer to the boundary) having a larger pressure drawdown compared to the bottom part. As a result the flow rate at the top end reduces and the flow rate at the bottom end increases in order to maintain a uniform pressure along the wellbore.

There is little variation in the wellbore pressure plotted in Figure 6.14 for all the configurations. This is expected for this study since the reservoir is homogeneous.

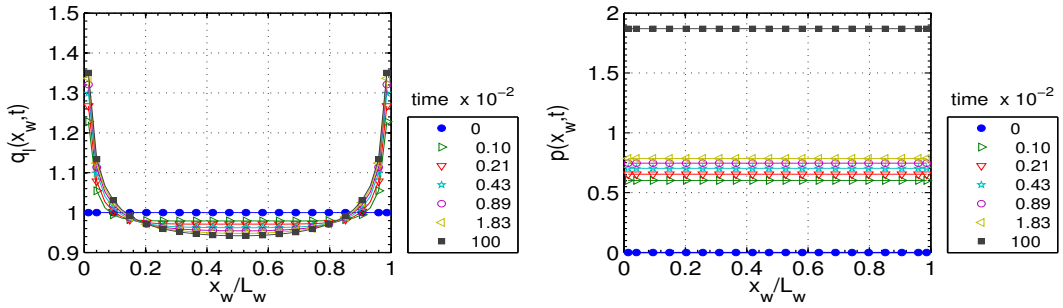

(a) case 1: $\theta = 0°, \phi = 0°$

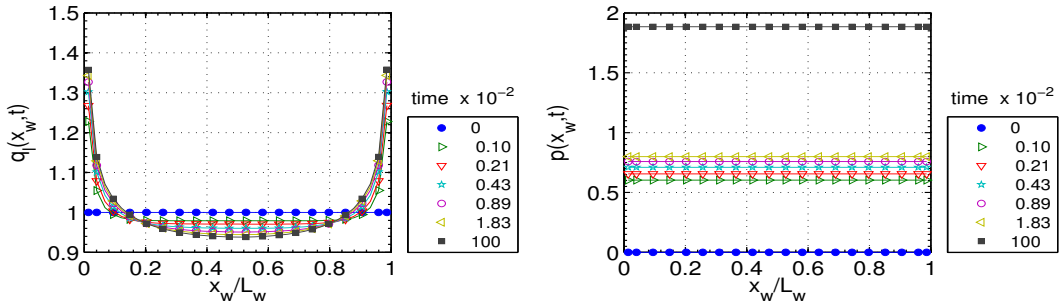

(b) case 2: $\theta = 45°, \phi = 0°$

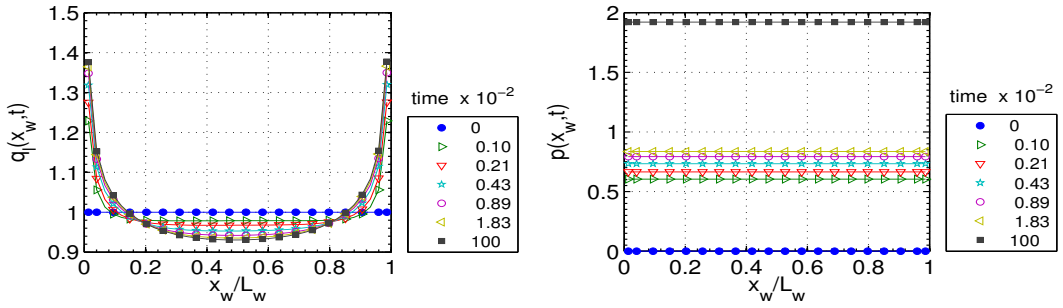

(c) case 3: $\theta = 0°, \phi = 13.263°$

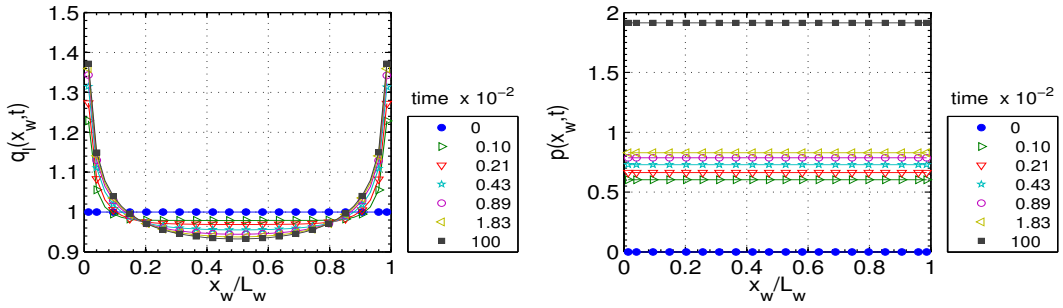

(d) case 4: $\theta = 45°, \phi = 13.263°$

Figure 6.14: Well flow-rate per unit length (left) and well pressure (right) for configurations obtained by rotating case 1 in the horizontal plane by $\theta°$ and in the vertical plane by $\phi°$.

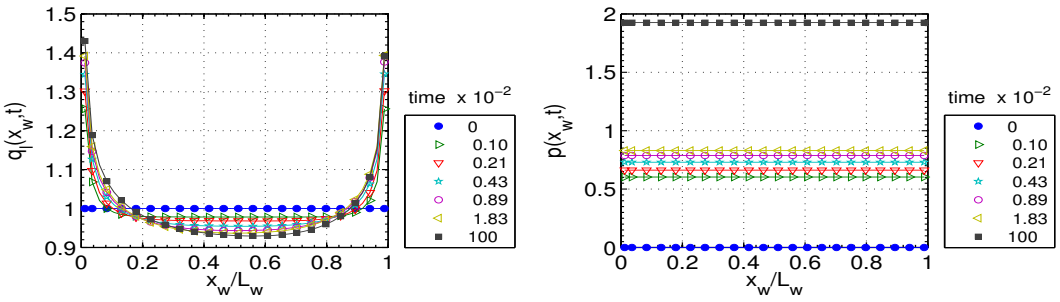

(e) case 5 (off-centre): $\theta = 45°, \phi = 13.263°$, and well midpoint shifted to the right by 0.1. Note the slight asymmetry in q_l.

Figure 6.14: Well flow-rate per unit length (left) and well pressure (right) for configurations obtained by rotating case 1 in the horizontal plane by $\theta°$ and in the vertical plane by $\phi°$.

6.9 Summary

By comparing with highly refined semi-analytic solutions, we have shown in this chapter that the decoupled overlapping grids method is able to produce very accurate results for the transient wellbore pressure of partially penetrating horizontal wells. For the uniform pressure case study, the method is able to produce an accurate pressure profile even on coarse grids, whereas a very fine semi-analytic solution is required to produce the same level of accuracy. The application to a slanted well shows the ability of the method to reproduce expected trends for a non-standard well configuration.

Chapter 7

Recommendations for Future Work

We make the following recommendations for future work:

Non-conventional wells

Non-conventional wells include horizontal, slanted, multi-lateral and undulating wells. These sorts of wells have become quite common in the oil industry because they can be drilled to better exploit special geological features within the reservoir that are not readily accessible with vertical wells, for example fractures and high permeability regions in the reservoir. To our knowledge the work in this thesis is the only one in the literature that offers a great deal of flexibility in modelling the transient wellbore (and near-wellbore) pressure for arbitrary well configurations down to the scale of the wellbore itself, and at the same time accurately incorporates both global and local reservoir heterogeneity effects. We have already presented an application of the decoupled overlapping grids method to computing the transient pressure of horizontal and slanted wells in Chapter 6. Application to other non-conventional well configurations, for example multi-lateral and undulating well, should be implemented.

Well conditions

Only constant total well flow rate applications were considered in this thesis. A natural extension is the application of the method of decoupled overlapping grids to compute transient well pressure for variable well flow rate conditions. The implementation outlined in this thesis remains the same for these conditions.

For the three-dimensional study carried out in Chapter 6, we considered two classical models of flow within the wellbore: the uniform flux and uniform pressure (or infinite conductivity) models. These models are approximations, and a more realistic model of flow should account for pressure drop within the wellbore (for instance by including frictional, gravitational and acceleration effects). Such models, often referred to as finite conductivity models for well flow, have been treated in the literature but only within the context of semi-analytic solutions for transient wellbore pressure [71, 75, 86]. We recommend that the finite conductivity model should be incorporated into the decoupled overlapping grids method. Other well properties, such as skin, should also be accounted for.

Application to field study

The method should be applied to actual field examples to demonstrate its effectiveness. In this case the first stage simulation of the field case study can be carried out in a commercial reservoir simulator, which can easily deal with reservoir heterogeneities and multi-phase flow.

Appendix A

Analytic Solutions and Numerical Considerations

A.1 Analytic solution for point source in infinite domain

We wish to solve (3.4) with (3.5), which are stated again below:

$$\frac{1}{\eta}\frac{\partial p}{\partial t} = \frac{\partial^2 p}{\partial r^2} + \frac{1}{r}\frac{\partial p}{\partial r}, \tag{A.1}$$

$$p(r, 0) = 0, \tag{A.2}$$

$$p(r \to \infty, t) = 0, \tag{A.3}$$

$$\lim_{r \to 0}\left(r\frac{\partial p_{\mathrm{ps}}}{\partial r}\right) = -Q. \tag{A.4}$$

Applying the similarity transformation

$$\xi = \frac{r^2}{\eta t}, \tag{A.5}$$

the equations are reduced to an ODE:

$$4\frac{d}{d\xi}\left(\xi\frac{dp_{\mathrm{ps}}}{d\xi}\right) = -\xi\frac{dp_{\mathrm{ps}}}{d\xi}, \tag{A.6}$$

$$\lim_{\xi\to 0}\left(2\xi\frac{dp_{\mathrm{ps}}}{d\xi}\right) = -Q, \tag{A.7}$$

$$p_{\mathrm{ps}}(\xi\to\infty) = 0. \tag{A.8}$$

Substituting $y = \xi\dfrac{dp_{\mathrm{ps}}}{d\xi}$ in (A.6) gives

$$\frac{dy}{d\xi} = -\frac{y}{4} \quad \text{so that} \quad y = y_0 e^{-\frac{\xi}{4}}. \tag{A.9}$$

From (A.7) $y_0 = -\dfrac{Q}{2}$, hence

$$\xi\frac{dp_{\mathrm{ps}}}{d\xi} = -\frac{Q}{2}e^{-\frac{\xi}{4}}, \quad \text{and so} \quad p_{\mathrm{ps}}(\xi) = -\frac{Q}{2}\int_{\xi}^{\infty}\frac{e^{-\frac{\xi}{4}}}{\xi}\,d\xi. \tag{A.10}$$

Substituting $x = \xi/4$ then gives

$$p_{\mathrm{ps}}(r,t) = \frac{Q}{2}\int_{r^2/(\eta t)}^{\infty}\frac{e^{-x}}{x}\,dx = -\frac{Q}{2}\mathrm{Ei}\left(-\frac{r^2}{4\eta t}\right). \tag{A.11}$$

A.2 Analytic solution for finite radius well in infinite domain

We wish to solve (3.4) with (3.7), which are stated again below:

$$\frac{1}{\eta}\frac{\partial p}{\partial t} = \frac{\partial^2 p}{\partial r^2} + \frac{1}{r}\frac{\partial p}{\partial r}, \tag{A.12}$$

$$p(r,0) = 0. \tag{A.13}$$

$$p(r\to\infty, t) = 0, \tag{A.14}$$

$$r\frac{\partial p_{\mathrm{fw}}}{\partial r}\bigg|_{r=r_w} = -Q. \tag{A.15}$$

Applying the Laplace transform

$$\hat{f}(s) = \int_0^\infty e^{-st} f(t)\, dt$$

to these equations gives

$$\frac{s}{\eta}\hat{p}_{\mathrm{fw}} = \frac{d^2\hat{p}_{\mathrm{fw}}}{dr^2} + \frac{1}{r}\frac{d\hat{p}_{\mathrm{fw}}}{dr}, \tag{A.16a}$$

$$\frac{d\hat{p}_{\mathrm{fw}}}{dr} = -\frac{Q}{sr_w} \qquad \text{at } r = r_w, \tag{A.16b}$$

$$\hat{p}_{\mathrm{fw}}(r \to \infty, s) = 0. \tag{A.16c}$$

Substituting $z = r\sqrt{s/\eta}$ into these equations gives the modified Bessel equation:

$$z^2\frac{d^2\hat{p}_{\mathrm{fw}}}{dz^2} + z\frac{d\hat{p}_{\mathrm{fw}}}{dz} - z^2\hat{p}_{\mathrm{fw}} = 0, \tag{A.17}$$

$$\left.\frac{d\hat{p}_{\mathrm{fw}}}{dz}\right|_{z=z_w} = -\frac{Q}{z_w s}, \tag{A.18}$$

$$\hat{p}_{\mathrm{fw}}(z \to \infty, s) = 0, \tag{A.19}$$

($z_w = r_w\sqrt{s/\eta}$), with general solution

$$\hat{p}_{\mathrm{fw}} = AI_0(z) + BK_0(z). \tag{A.20}$$

I_0 and K_0 are modified Bessel functions of the first and second kind respectively. To ensure that $\hat{p}_{\mathrm{fw}} \to 0$ as $z \to \infty$, we need $A = 0$. Then applying (A.18) to (A.20) gives

$$\frac{d\hat{p}_{\mathrm{fw}}}{dz}(z_w) = -BK_1(z_w) = -\frac{Q}{z_w s}, \tag{A.21}$$

$$B = \frac{Q}{z_w s K_1(z_w)}. \tag{A.22}$$

So

$$\hat{p}_{\text{fw}}(r,s) = \frac{Q\sqrt{\eta}K_0\big(r\sqrt{s/\eta}\big)}{r_w(\sqrt{s})^3 K_1(r_w\sqrt{s/\eta})}. \tag{A.23}$$

A.3 Average Fourier series solution at a fixed radius away from a point source

Given

$$p_{\text{ps}}(x,y,t) = \frac{4}{x_e y_e}\left\{\frac{t}{4} + \frac{1}{2}\sum_{n=1}^{\infty}\frac{x_e^2}{n^2\pi^2}\left[1-\exp\left(-\frac{n^2\pi^2}{x_e^2}t\right)\right]\cos\frac{n\pi x_w}{x_e}\cos\frac{n\pi x}{x_e} + \right.$$
$$\frac{1}{2}\sum_{k=1}^{\infty}\frac{y_e^2}{k^2\pi^2}\left[1-\exp\left(-\frac{k^2\pi^2}{y_e^2}t\right)\right]\cos\frac{k\pi y_w}{y_e}\cos\frac{k\pi y}{y_e} +$$
$$\left.\sum_{n=1}^{\infty}\sum_{k=1}^{\infty}\frac{x_e^2 y_e^2}{\pi^2(n^2y_e^2+k^2x_e^2)}\left[1-\exp\left(-\left[\frac{n^2\pi^2}{x_e^2}+\frac{k^2\pi^2}{y_e^2}\right]t\right)\right]\cos\frac{n\pi x_w}{x_e}\cos\frac{k\pi y_w}{y_e}\cos\frac{n\pi x}{x_e}\cos\frac{k\pi y}{y_e}\right\} \tag{A.24}$$

from (3.19) we want to compute

$$p_{\text{ps}}(r,t) = \frac{1}{2\pi}\int_0^{2\pi} p_{\text{ps}}(x_w + r\cos\theta, y_w + r\sin\theta, t)\, d\theta. \tag{A.25}$$

We proceed to calculate $\dfrac{x_e y_e}{4}p_{\text{ps}}(r,t)$ by integrating each term in (A.24). The first term remains as $\dfrac{t}{4}$. For subsequent terms we need the Bessel function:

$$J_0(x) = \frac{1}{2\pi}\int_0^{2\pi}\cos(x\cos\theta)\, d\theta = \frac{1}{2\pi}\int_0^{2\pi}\cos(x\sin\theta)\, d\theta. \tag{A.26}$$

For the second term:

$$\frac{1}{2\pi}\int_0^{2\pi}\cos\left(\frac{n\pi}{x_e}(x_w + r\cos\theta)\right)\, d\theta = \frac{1}{2\pi}\cos\left(\frac{n\pi}{x_e}x_w\right)\int_0^{2\pi}\cos\left(\frac{n\pi}{x_e}r\cos\theta\right)\, d\theta$$
$$-\frac{1}{2\pi}\sin\left(\frac{n\pi}{x_e}x_w\right)\int_0^{2\pi}\sin\left(\frac{n\pi}{x_e}r\cos\theta\right)\, d\theta. \tag{A.27}$$

The integral of the sine function above is zero in this interval. So we are left with

$$\frac{1}{2\pi}\int_0^{2\pi}\cos\left(n\pi(x_w + r\cos\theta)/x_e\right)\ d\theta = \cos\left(\frac{n\pi x_w}{x_e}\right)J_0(n\pi r/x_e). \tag{A.28}$$

Likewise for the third term we have

$$\frac{1}{2\pi}\int_0^{2\pi}\cos\left(k\pi(y_w + r\sin\theta)/y_e\right)\ d\theta = \cos\left(\frac{k\pi y_w}{y_e}\right)J_0(k\pi r/y_e). \tag{A.29}$$

For the fourth term we want to evaluate

$$\frac{1}{2\pi}\int_0^{2\pi}\cos\left(\frac{n\pi}{x_e}(x_w + r\cos\theta)\right)\cos\left(\frac{k\pi}{y_e}(y_w + r\sin\theta)\right)\ d\theta. \tag{A.30}$$

Let $\alpha_1 = n\pi x_w/x_e, \alpha_2 = k\pi y_w/y_e, r_x = n\pi r/x_e, r_y = k\pi r/y_e$. Then we have

$$\begin{aligned}\frac{1}{2\pi}\int_0^{2\pi}\cos(\alpha_1 + r_x\cos\theta)\cos(\alpha_2 + r_y\sin\theta)\ d\theta = \\ \frac{1}{2\pi}\cdot\frac{1}{2}\int_0^{2\pi}\cos\left[(\alpha_1+\alpha_2) + r_x\cos\theta + r_y\sin\theta\right]\ d\theta + \\ \frac{1}{2\pi}\cdot\frac{1}{2}\int_0^{2\pi}\cos\left[(\alpha_1-\alpha_2) + r_x\cos\theta - r_y\sin\theta\right]\ d\theta.\end{aligned} \tag{A.31}$$

To evaluate the first integral on the RHS of (A.31), let

$$r_x\cos\theta + r_y\sin\theta = \beta_1\sin(\theta+\phi_1) \equiv \beta_1(\sin\theta\cos\phi_1 + \cos\theta\sin\phi_1). \tag{A.32}$$

Then

$$r_x = \beta_1\sin\phi_1, \quad r_y = \beta_1\cos\phi_1, \tag{A.33}$$

so that

$$\beta_1 = \sqrt{r_x^2 + r_y^2}, \quad \phi_1 = \tan^{-1}\frac{r_x}{r_y}, \tag{A.34}$$

and

$$\frac{1}{2\pi}\int_0^{2\pi} \cos\left[(\alpha_1+\alpha_2)+r_x\cos\theta+r_y\sin\theta\right]\, d\theta = \frac{1}{2\pi}\int_0^{2\pi} \cos([(\alpha_1+\alpha_2)+\beta_1\sin(\theta+\phi_1))\, d\theta. \quad \text{(A.35)}$$

Applying the change of variables:

$$z = \theta + \phi_1 \quad \text{(A.36)}$$

$$dz = d\theta \quad \text{(A.37)}$$

gives

$$\begin{aligned}\frac{1}{2\pi}\int_{\phi_1}^{\phi_1+2\pi} \cos\left[(\alpha_1+\alpha_2)+\beta_1\sin z\right]\, dz & \\ = \cos(\alpha_1+\alpha_2)\frac{1}{2\pi}\int_{\phi_1}^{\phi_1+2\pi}\cos(\beta_1\sin z)\, dz & \\ - \sin(\alpha_1+\alpha_2)\frac{1}{2\pi}\int_{\phi_1}^{\phi_1+2\pi}\sin(\beta_1\sin z)\, dz, & \quad \text{(A.38)}\\ = \cos(\alpha_1+\alpha_2)J_0(\beta_1). & \quad \text{(A.39)}\end{aligned}$$

For the second integral on the RHS of (A.31):

$$\frac{1}{2\pi}\cdot\frac{1}{2}\int_0^{2\pi} \cos\left[(\alpha_1-\alpha_2)+r_x\cos\theta-r_y\sin\theta\right]\, d\theta,$$

let

$$r_x\cos\theta - r_y\sin\theta = \beta_2\cos(\theta+\phi_2) = \beta_2(\cos\theta\cos\phi_2 - \sin\theta\sin\phi_2), \quad \text{(A.40)}$$

$$r_x = \beta_2\cos\phi_2, \quad r_y = \beta_2\sin\phi_2, \quad \text{(A.41)}$$

so that

$$\beta_2 = \sqrt{r_x^2 + r_y^2} = \beta_1, \quad \phi_2 = \tan^{-1}\frac{r_y}{r_x}. \tag{A.42}$$

Using the change of variables

$$z_2 = \theta + \phi_2, \qquad dz_2 = d\theta, \tag{A.43}$$

gives

$$\frac{1}{2\pi}\int_0^{2\pi} \cos\left[(\alpha_1 - \alpha_2) + \beta_2\cos(\theta+\phi_2)\right]\, d\theta$$

$$= \frac{1}{2\pi}\int_{\phi_2}^{\phi_2+2\pi} \cos\left[(\alpha_1 - \alpha_2) + \beta_2\cos(z_2)\right]\, dz_2, \tag{A.44}$$

$$= \cos(\alpha_1-\alpha_2)\frac{1}{2\pi}\int_{\phi_2}^{\phi_2+2\pi} \cos(\beta_2\cos z_2)\, dz_2$$

$$- \sin(\alpha_1-\alpha_2)\frac{1}{2\pi}\int_{\phi_2}^{\phi_2+2\pi} \sin(\beta_2\cos z_2)\, dz_2, \tag{A.45}$$

$$= \cos(\alpha_1-\alpha_2)J_0(\beta_2). \tag{A.46}$$

And so (A.30) has the solution

$$\frac{1}{2}J_0\left(\pi r\sqrt{\frac{n^2}{x_e^2}+\frac{k^2}{b^2}}\right)\left[\cos\left(\frac{n\pi x_w}{x_e}+\frac{k\pi y_w}{y_e}\right)+\cos\left(\frac{n\pi x_w}{x_e}-\frac{k\pi y_w}{y_e}\right)\right]$$

$$= J_0\left(\pi r\sqrt{\frac{n^2}{x_e^2}+\frac{k^2}{y_e^2}}\right)\cos\frac{n\pi x_w}{x_e}\cos\frac{k\pi y_w}{y_e}. \tag{A.47}$$

Therefore

$$p_{\mathrm{ps}}(r,t) = \frac{4}{x_e y_e}\left\{\frac{t}{4} + \frac{1}{2}\sum_{n=1}^{\infty}\frac{x_e^2}{n^2\pi^2}\left[1-\exp\left(-\frac{n^2\pi^2}{x_e^2}t\right)\right]\cos^2\frac{n\pi x_w}{x_e}J_0(n\pi r/x_e) + \right.$$

$$\frac{1}{2}\sum_{k=1}^{\infty}\frac{y_e^2}{k^2\pi^2}\left[1-\exp\left(-\frac{k^2\pi^2}{y_e^2}t\right)\right]\cos^2\frac{k\pi y_w}{y_e}J_0(k\pi r/y_e) +$$

$$\left.\sum_{n=1}^{\infty}\sum_{k=1}^{\infty}\frac{x_e^2 y_e^2}{\pi^2(n^2y_e^2+k^2x_e^2)}\left[1-\exp\left(-\left[\frac{n^2\pi^2}{x_e^2}+\frac{k^2\pi^2}{y_e^2}\right]t\right)\right]\cos^2\frac{n\pi x_w}{x_e}\cos^2\frac{k\pi y_w}{y_e}J_0\left(\pi r\sqrt{\frac{n^2}{x_e^2}+\frac{k^2}{y_e^2}}\right)\right\}. \tag{A.48}$$

A.4 Maximum error in an infinite domain

In this section we derive an analytic relationship between the maximum error in absolute pressure at fixed radii and the dimensionless radius for an infinite homogeneous domain (see Figure A.1), which was discussed in Section 3.3.2. The outliers in Figure A.1 occur at $r_D = 300$ for $r_w = 0.001$, and at $r_D = 50$ for $r_w = 0.01$, which are closest to the domain boundary. A closed-form expression for the relationship between $\max(|p_{\text{ps}} - p_{\text{fw}}|)$ and r_D in an infinite domain is derived below.

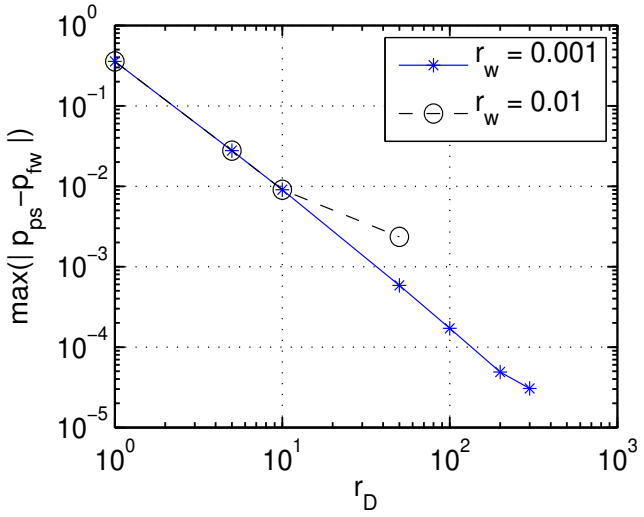

Figure A.1: Maximum error in Figure 3.6 plotted against dimensionless radius $r_D = r_e/r_w$.

The analytic solutions for a finite radius well and a point source well in Laplace space are respectively (see (3.10), (3.13)),

$$\hat{p}_{\text{fw}}(r,s) = \frac{QK_0(r\sqrt{s})}{r_w(\sqrt{s})^3 K_1(r_w\sqrt{s})}, \qquad \hat{p}_{\text{ps}}(r,s) = \frac{Q}{s}K_0(r\sqrt{s}), \tag{A.49}$$

where K_0, K_1 are modified Bessel functions of the second kind. Define the error in Laplace space $\hat{e}_1$ as

$$\hat{e}_1 = \hat{p}_{\text{fw}} - \hat{p}_{\text{ps}} = \frac{QK_0(r\sqrt{s})}{s}\left(\frac{1}{r_w\sqrt{s}K_1(r_w\sqrt{s})} - 1\right). \tag{A.50}$$

Since we are interested in the maximum error at dimensionless time t_D, a change

of variable $s_1 = s/r^2$ is applied to (A.50) before taking the asymptotic expansion as $r_D \to \infty$. The result from the asymptotic expansion is then converted back to $s = s_1 r^2$, the Laplace inverse computed, and this result is then expressed in terms of dimensionless time.

The asymptotic expansion of (A.50) as $r_D \to \infty$ is computed in Maple (see Table A.1). The leading term in this expansion is $\hat{e}_2$

$$\hat{e}_2 = \frac{Qr_w^2}{4}\left[\left(2\ln(2) - 2\ln(r_w) - 2\gamma + 1\right)K_0(r_D r_w\sqrt{s}) - K_0(r_D r_w\sqrt{s})\ln(s)\right]. \quad \text{(A.51)}$$

```
rr := r[D]*r[w]
```

$$r_D r_w$$

```
simplify(subs(s = s/rr^2, e[1]))
```

$$\frac{BesselK\left(0, \sqrt{s}\right) {r_D}^2 {r_w}^2 \left(r_D - \sqrt{s} BesselK\left(1, \frac{\sqrt{s}}{r_D}\right)\right)}{s^{3/2}\left(BesselK\left(1, \frac{\sqrt{s}}{r_D}\right)\right)}$$

```
convert(series(%, r[D] = infinity, 2), polynom)
```

$$-\frac{BesselK\left(0, \sqrt{s}\right) {r_w}^2 \left(1/2\ \left(\ln\left(1/2\sqrt{s}\right) - \ln\left(r_D\right)\right)\sqrt{s} - 1/4\sqrt{s}\left(-2\gamma + 1\right)\right)}{\sqrt{s}}$$

```
e[2] := simplify(subs(s = s*rr^2, %));
```

$$-1/4\, BesselK\left(0, r_D r_w\sqrt{s}\right) {r_w}^2 \left(-2\ln\left(2\right) + 2\ln\left(r_w\right) + \ln\left(s\right) + 2\gamma - 1\right)$$

Table A.1: Maple code for asymptotic expansion of (A.50) as $r_D \to \infty$.

To compute the inverse of (A.51) the differentiation rule of Laplace transforms is applied. Let

$$f = -\frac{1}{2}\mathrm{Ei}\left(-\frac{(r_D r_w)^2}{4t}\right). \tag{A.52}$$

Then
$$\mathcal{L}\left(\frac{df(t)}{dt}\right) = f(0) + s\hat{f}(s) \tag{A.53}$$

$$= s\frac{K_0(r_D r_w\sqrt{s})}{s} = K_0(r_D r_w\sqrt{s}). \tag{A.54}$$

So
$$\mathcal{L}^{-1}\left(K_0(r_D r_w\sqrt{s})\right) = -\frac{1}{2}\frac{d}{dt}\left[\mathrm{Ei}\left(-\frac{(r_D r_w)^2}{4t}\right)\right] \tag{A.55}$$

$$= \frac{1}{2t}\exp\left(-\frac{(r_D r_w)^2}{4t}\right). \tag{A.56}$$

Also from the convolution rule of Laplace transforms,

$$\mathcal{L}^{-1}\big(\hat{f}(s)\hat{g}(s)\big) = \int_0^t f(u)g(t-u)\,du. \tag{A.57}$$

So

$$\begin{aligned}\mathcal{L}^{-1}\big(K_0(r_D r_w\sqrt{s})\ln(s)\big) &= \mathcal{L}^{-1}\left(\left[sK_0(r_D r_w\sqrt{s})\right]\left[\frac{\ln(s)}{s}\right]\right)\\ &= \int_0^t\left[-\frac{4u-(r_D r_w)^2}{8u^3}\exp\left(-\frac{(r_D r_w)^2}{4u}\right)\right]\Big[-\gamma-\ln(t-u)\Big]\,du\\ &= \frac{\ln(r_D)+\ln(r_w)-\ln(2)-\ln(t)}{t}\exp\left(-\frac{(r_D r_w)^2}{4t}\right).\end{aligned} \tag{A.58}$$

Substituting (A.56), (A.58) and $t_D = 4t/r^2$ into (A.51) gives

$$e_2 = \frac{Q}{2}\exp\left(-\frac{1}{t_D}\right)\frac{1+2\ln(r_D)+2\ln(t_D)-2\gamma}{t_D r_D^2} \tag{A.59}$$

where $\gamma \approx 0.5772$ is Euler's constant. Further analysis of (A.59) in Maple did not yield an explicit solution for the turning point. However Figure A.2 shows that a good estimate of the turning point is at $t_D = 1$, so that

$$\max(e_2) \approx \frac{Q\exp(-1)(1+2\ln(r_D)-2\gamma)}{2r_D^2} \quad \text{as} \quad r_D \to \infty\,. \tag{A.60}$$

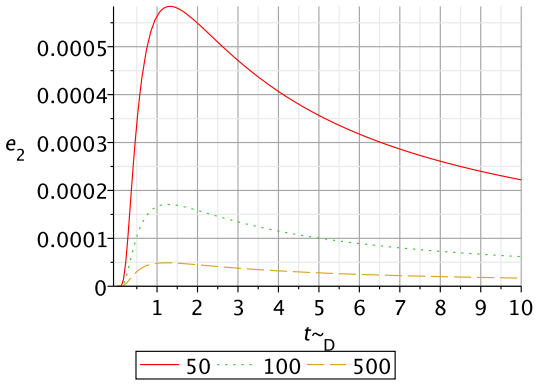

Figure A.2: Plot of e_2 from (A.59) against dimensionless time t_D for different r_D.

The estimate in (A.60), together with the maximum error for $r_w = 0.001$ and $r_w = 0.01$ shown in Figure A.1, are plotted in Figure A.3. It shows that (A.60) closely approximates the maximum error over much of the range of r_D. However, the estimate is not valid as r_D gets smaller, and the results deviate from the prediction when r_D is big enough that measurement points are on or close to the outer boundary of the original, physical domain, for example the outliers at $r_D = 300$ for $r_w = 0.001$, and at $r_D = 50$ for $r_w = 0.01$.

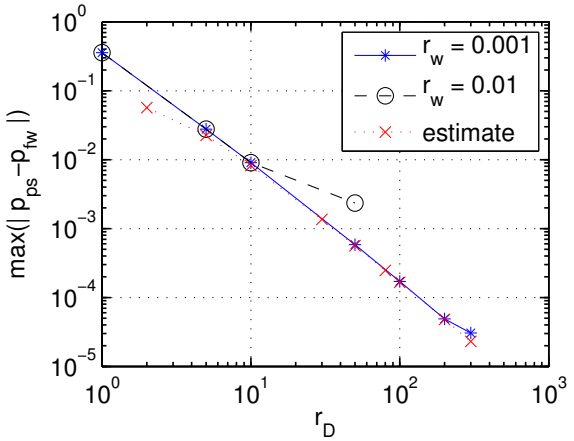

Figure A.3: Actual and estimated maximum error.

A.5 Mass conservation of finite element solution for global stage problem in 2D homogeneous domain

For the point source well problem discussed in Section 3.4.1, we measured the average pressure at fixed radii r_e from the global simulation results. Figure A.4 shows a sharp increase of the absolute error in this quantity for late simulation times. This is due to a lack of mass conservation in the FEM discretisation in Matlab as a result of rounding errors. We explain this below.

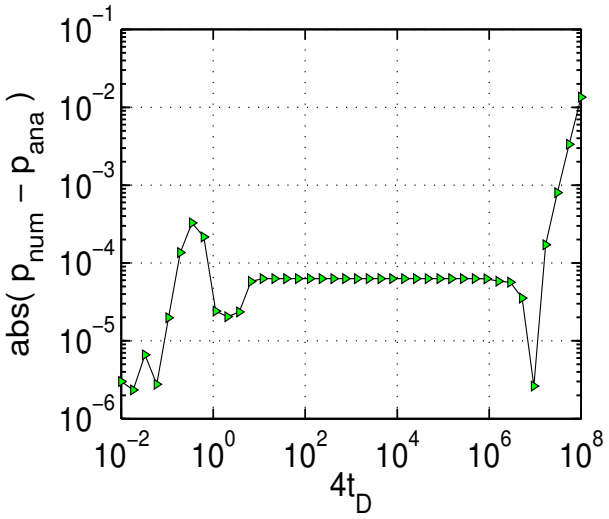

Figure A.4: Absolute error in average pressure measured at radius $r_e = 0.3$. p_{ana} = analytic solution for point source well problem (see Section 3.3.2). p_{num} = numerical solution for point source well problem discretised in space using the finite element method (see Section 3.4.1).

The equations solved for the global point source well problem were given in (3.26). They are stated again below:

$$\frac{\partial p_{\text{ps}}}{\partial t}(\mathbf{x}, t) = \nabla^2 p_{\text{ps}}(\mathbf{x}, t) + \delta(\mathbf{x} - \mathbf{x}_0) \qquad \text{in } \Omega \times (0, T], \tag{A.61a}$$

$$\mathbf{n} \cdot \nabla p_{\text{ps}}(\mathbf{x}, t) = 0 \qquad \text{in } \partial\Omega_o, \tag{A.61b}$$

$$p_{\text{ps}}(\mathbf{x}, 0) = 0 \qquad \text{in } \Omega, \tag{A.61c}$$

where $(q, k, \mu, H, c_t, \phi)$ have been set to 1. The total pressure in the system at

time t is calculated as follows:

$$\int_\Omega \frac{\partial p_{\mathrm{ps}}}{\partial t}(\mathbf{x},t)\, d\Omega = \int_\Omega \nabla^2 p_{\mathrm{ps}}(\mathbf{x},t)\, d\Omega + \int_\Omega \delta(\mathbf{x}-\mathbf{x}_0) \tag{A.62}$$

$$\frac{\partial}{\partial t}\int_\Omega p_{\mathrm{ps}}(\mathbf{x},t)\, d\Omega = \frac{\partial \overline{p}_{\mathrm{ps}}}{\partial t}(t) = 1 \tag{A.63}$$

$$\overline{p}_{\mathrm{ps}}(t) = t. \tag{A.64}$$

Here we have used the divergence theorem and the boundary condition in (A.61b) to set the second integral in (A.62) to zero. The absolute difference $|\overline{p}_{\mathrm{ps}}(t) - t|$ is plotted in Figure A.5 together with the absolute error in the average pressure at $r_e = 0.3$ (from Figure A.4). It is clear from this plot that the sharp increase in the pressure measured at the radius r_e is due to a loss in the conservation of the total pressure.

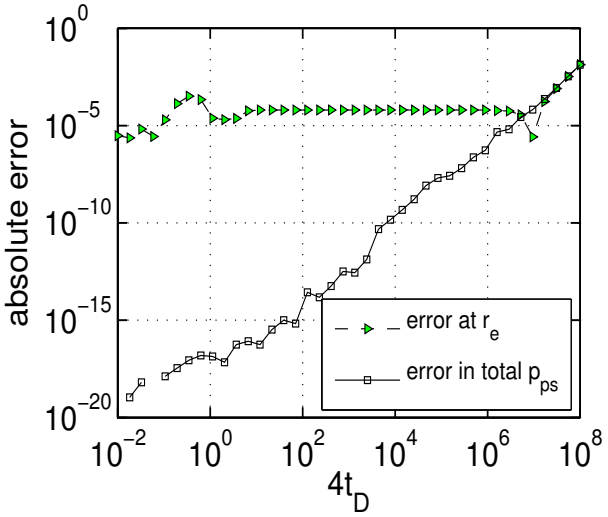

Figure A.5: Absolute error in $\overline{p}_{ps}$ (from (A.64)) and average pressure at $r_e = 0.3$ (see Figure A.4).

Let the vector $\underline{p}_{\mathrm{ps}}$ denote the solution to the semi-discrete approximation of (A.61):

$$M\dot{\underline{p}}_{\mathrm{ps}} = S\underline{p}_{\mathrm{ps}} + \underline{f}, \tag{A.65}$$

where the dot represents the time derivative, M and S are the mass and stiffness matrices respectively, and the vector $\underline{f}$ contains the contribution from the delta function. The integration in (A.62) corresponds to applying a quadrature rule to

the semi-discrete equations in (A.65), that is,

$$\underline{\beta}^T M \underline{\dot{p}}_{\text{ps}} = \underline{\beta}^T S \underline{p}_{\text{ps}} + \underline{\beta}^T \underline{f}. \tag{A.66}$$

From the properties of (A.61) it is expected that $\underline{\beta}^T S = \underline{0}$ (so that $\underline{\beta}^T$ is the left null vector of S, which turns out to be $\underline{\beta}^T = (1, 1, 1, \ldots, 1)$). However due to the rounding error in assembling S in Matlab, we get instead an approximate stiffness matrix $\tilde{S}$ that satisfies $\underline{\beta}^T \tilde{S} = \mathcal{O}(10^{-15})$. The error introduced by $\tilde{S}$ for late simulation times can be better understood if the solution to (A.61) is split into 3 parts:

$$p_{\text{ps}}(\mathbf{x}, t) = v(\mathbf{x}, t) + w(\mathbf{x}) + ct. \tag{A.67}$$

Here $v(\mathbf{x}, t)$ is the initial transient component, $w(\mathbf{x})$ is the pseudo-steady-state component, and c is a constant. The initial transient component $v(\mathbf{x}, t)$ evolves to a constant steady-state as $t \to \infty$,

$$v(\mathbf{x}, t) \to \int_\Omega v(\mathbf{x}, 0)\, d\Omega \tag{A.68}$$

and it is convenient to pick v so that $v(\mathbf{x}, t) \to 0$ as $t \to \infty$. An analogous splitting to (A.67) applies to $\underline{p}_{\text{ps}}$:

$$\underline{p}_{\text{ps}}(t) = \underline{v}(t) + \underline{w} + ct\underline{\beta}, \tag{A.69}$$

and in this case as well, $\underline{v}(t)$ is selected such that $\underline{v}(t) \to 0$ as $t \to \infty$.

Substituting the approximate stiffness matrix $\tilde{S}$ into (A.66) and integrating with respect to time we get:

$$\underline{\beta}^T M \underline{\dot{p}}_{\text{ps}} = \underline{\beta}^T \tilde{S} \underline{p}_{\text{ps}} + \underline{\beta}^T \underline{f}, \tag{A.70}$$

$$\underline{\beta}^T M \underline{p}_{\text{ps}} = \int \underline{\beta}^T \tilde{S} \underline{p}_{\text{ps}}\, dt + t\underline{\beta}^T \underline{f}. \tag{A.71}$$

The term under the integral sign is not zero. Instead from (A.69) we have:

$$\int \underline{\beta}^T \tilde{S} \underline{p}_{\text{ps}} \, dt = \underline{\beta}^T \tilde{S} \int \left(\underline{v}(t) + \underline{w} + ct\underline{\beta} \right) dt, \tag{A.72}$$

$$= t\underline{\beta}^T \tilde{S} \underline{w} + \frac{ct^2}{2} \underline{\beta}^T \tilde{S} \underline{\beta} \qquad \text{as } t \to \infty. \tag{A.73}$$

As $t \to \infty$, the $\mathcal{O}(t^2)$ term in (A.73) becomes significant. This is clearly demonstrated in Figure A.6 where the error in the total pressure has been plotted against time together with a line of slope 2.

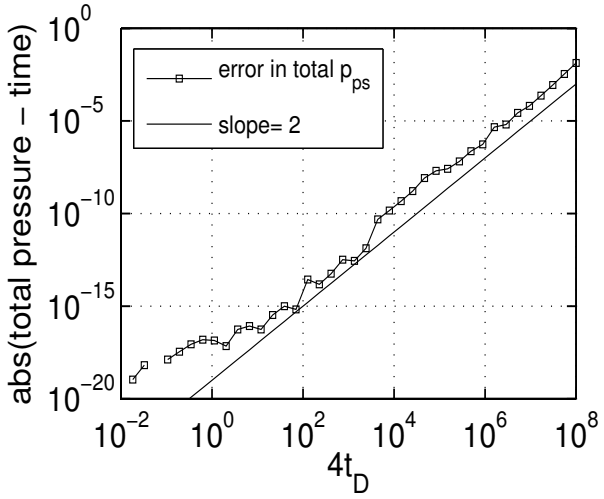

Figure A.6: Error due to approximate stiffness matrix $\tilde{S}$ (see (A.73)).

A fix that can be implemented for this rounding error problem is to compute each component of $\underline{p}_{\text{ps}}$ in (A.69) separately. By doing this and specifying that $\underline{v}(t) \to 0$ as $t \to \infty$, the round off error introduced by the approximate stiffness matrix dies off with the transient component $\underline{v}(t)$. Substituting (A.69) into (A.65) we get:

$$M(\dot{\underline{v}}(t) + c\underline{\beta}) = S(\underline{v}(t) + \underline{w} + ct\underline{\beta}) + \underline{f} \tag{A.74}$$

which decouples into

$$M\underline{\dot{v}} = S\underline{v}; \quad \underline{v}(0) = -\underline{w}; \tag{A.75}$$

$$S\underline{w} = cM\underline{\beta} - \underline{f}. \tag{A.76}$$

As stated earlier, we want $\underline{v}(t) \to 0$ as $t \to \infty$. Since

$$\underline{v}(t) \to \int_\Omega \underline{v}(0)\, d\Omega \equiv -\underline{\beta}^T M\underline{w} \quad \text{as} \quad t \to \infty, \tag{A.77}$$

we set $\underline{\beta}^T M\underline{w} = 0$. This gives an additional constraint for $\underline{w}$. (S is singular so (A.76) can only be solved up to an arbitrary constant unless an additional constraint is specified). Also, multiplying both sides of (A.76) by $\underline{\beta}^T$ gives an expression for c. Therefore we end up with the following equations for $\underline{v}, \underline{w}, c$:

$$M\underline{\dot{v}} = S\underline{v}; \qquad \underline{v}(0) = -\underline{w}; \tag{A.78}$$

$$S\underline{w} = cM\underline{\beta} - \underline{f}; \quad \underline{\beta}^T M\underline{w} = 0; \tag{A.79}$$

$$c = \frac{\underline{\beta}^T f}{\underline{\beta}^T M\underline{\beta}}. \tag{A.80}$$

A comparison of the average pressure at $r_e = 0.3$ obtained from straightforward integration of the semi-discrete equation in (A.65) (unsplit), and from calculating each component of $\underline{p}_{\text{ps}}$ using (A.78)–(A.80) and then assembling using (A.69) (split), is shown in Figure A.7(a). It is seen that there is no sharp increase in the absolute error calculated from the split version. Figure A.7(b) clearly shows that for the split version, the rounding error from the approximate stiffness matrix does not propagate into the late simulation time.

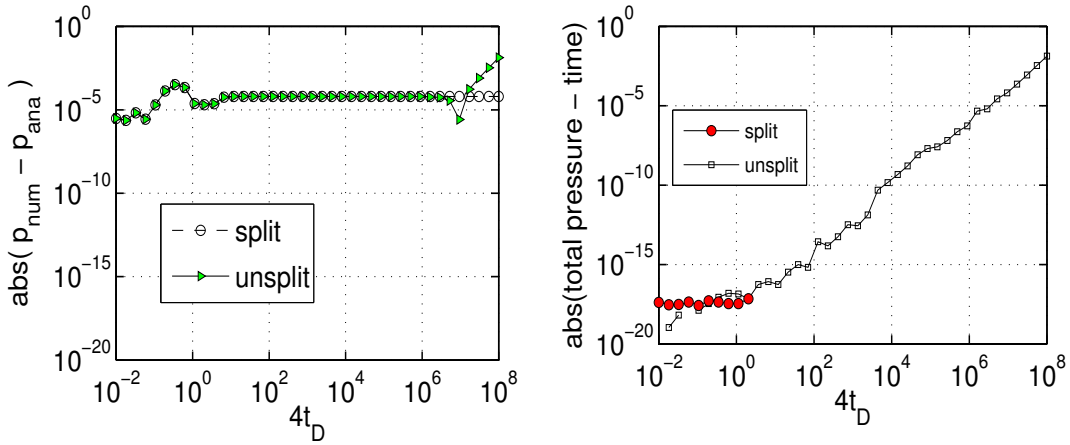

(a) Absolute error in average pressure at $r_e = 0.3$.

(b) Absolute error in total pressure

Figure A.7: Total pressure in domain and average pressure at $r_e = 0.3$ for finite element simulation implemented by (A.78)–(A.80) (split) and by (A.65) (unsplit).

Bibliography

[1] I. Aavatsmark and R.A. Klausen. Well index in reservoir simulation for slanted and slightly curved wells in 3D grids. *SPE Journal*, 8(1):41–48, March 2003. SPE 75275.

[2] J.H. Abou-Kassem and K. Aziz. Analytical well models in reservoir simulation. *SPE Journal*, 25(4):573–579, August 1985. SPE 11719.

[3] C. Aguilar, E. Ozkan, H. Kazemi, M. Al-Kobaisi, and B. Ramirez. Transient behaviour of multilateral wells in numerical models: A hybrid analytical-numerical approach. In *15th SPE Middle East Oil & Gas Show and Conference, Bahrain International Exhibition Center, Kingdom of Bahrain*, 11-14 March 2007. SPE 104581.

[4] R. Aguilera and M. Ng. Transient pressure analysis of horizontal wells in anisotropic naturally fractured reservoirs. *SPE Formation Evaluation*, 6(1):95–100, 1991.

[5] M. Ainsworth and J.T. Oden. *A Posteriori Error Estimation in Finite Element Analysis*. Wiley Interscience. John Wiley & Sons Inc., 2000.

[6] N. Al-Ajmi, M. Ahmadi, E. Ozkan, and H. Kazemi. Numerical inversion of Laplace transforms in the solution of transient flow problems with discontinuities. In *SPE Annual Technical Conference and Exhibition, Denver, Colorado, USA*, 21-24 September 2008. SPE 116255.

[7] N. Al-Mohannadi, E. Ozkan, and H. Kazemi. Grid system requirements in numercial modeling of pressure-transient tests in horizontal wells. *SPE Reservoir Evaluation and Engineering*, pages 122–131, 2007. SPE 94153.

[8] R.A. Archer and R.N. Horne. Green element method and singularity programming for numerical well test analysis. *Engineering Analysis with Boundary Elements*, 26:537–546, 2002.

[9] R.A. Archer and T.T. Yildiz. Transient well index for numerical well test analysis. Presented at SPE Annual Technical Conference and Exhibition, New Orleans, Louisiana, 30 September–3 October 2001. SPE 71575.

[10] F. Azar-Nejad, W.S. Tortike, and S.M. Farouq Ali. 3-d analytical solution to the diffusivity equation for finite sources with application to horizontal wells. In *European 3-D Reservoir Modelling Conference, Stavanger, Norway*, 16-17 April 1996.

[11] D.K. Babu and A.S. Odeh. Productivity of a horizontal well. *SPE Reservoir Engineering*, pages 417–421, November 1989.

[12] D.K. Babu, A.S. Odeh, A.J. Al-Khalifa, and R.C. McCann. The relation between wellblock and wellbore pressures in numerical simulation of horizontal wells. *SPE Reservoir Engineering*, pages 324–328, August 1991. SPE 20161.

[13] J Besson. Performance of slanted and horizontal wells on an anisotropic medium, 1990. SPE 20965.

[14] G. Blanc, D. Y. Ding, A. Ene, T. Estebenet, and D. Rahon. Transient productivity index for numerical well test simulations. *Reservoir Characterization – Recent Advances, AAPG Memoir*, 71:163–174, 1999.

[15] Dominique Bourdet. *Well Test Analysis: The Use of Advanced Interpretation Models*. Elsevier, 2002.

[16] M. Bourgeois and P. Couillens. Use of well test analytical solutions for production prediction. In *European Petroleum Conference London, U.K.*, 25-27 October 1994. SPE 28899.

[17] Susanne C. Brenner and L. Ridgway Scott. *The Mathematical Theory of Finite Element Methods*. Springer, 2002.

[18] H.S. Carslaw and J.C. Jaeger. *Conduction of Heat in Solids*. Oxford University Press, 1959.

[19] Amanat U. Chaudhry. *Oil Well Testing Handbook*. Gulf Professional Publishing, 2004.

[20] G. Chen, D.H. Tehrani, and J.M Peden. Calculation of well productivity in a reservoir simulator (I). Presented at the 13th SPE Symposium on Reservoir Simulation, San Antonio, Texas., 12-15 February 1995. SPE 29121.

[21] G. Chen, D.H. Tehrani, and J.M Peden. Calculation of well productivity in a reservoir simulator (II). Presented at the International Meeting on Petroleum Engineering, Beijing, China, 14-17 November 1995. SPE 29932.

[22] Y. Chen and X. Wu. Upscaled modeling of well singularity for simulating flow in heterogeneous formations. *Computational Geosciences*, 12:29–45, 2008.

[23] Z. Chen and X. Yue. Numerical homogenization of well singularities in the flow transport through heterogeneous porous media. *Multiscale Modeling & Simulation*, 1(2):260–303, 2003.

[24] Z. Chen and Y. Zhang. Well flow models for various numerical methods. *International Journal of Numerical Analysis & Modeling*, 6(3):375–388, 2009.

[25] Zhangxin Chen, Guanren Huan, and Yuanle Ma. *Computational Methods for Multiphase Flows in Porous Media*. Computational Science and Engineering. SIAM, 2006.

[26] G. Chesshire and W.D. Henshaw. Composite overlapping meshes for the solution of partial differential equations. *Journal of Computational Physics*, 90(1):1–64, 1990.

[27] G. Chesshire and W.D. Henshaw. A scheme for conservative interpolation on overlapping grids. *SIAM Journal on Scientific Computing*, 15(4):819–845, 1994.

[28] COMSOL Multiphysics 3.5a. COMSOL, Inc., 1 New England Executive Park, Burlington, MA 01803. Copyright 1998-2008 by COMSOL AB.

[29] F. Daviau, G. Mouronval, G. Bourdarot, and P. Curutchet. Pressure analysis for horizontal wells. *SPE Formation Evaluation*, 3(4):716–724, 1988.

[30] G. Desquesnes, M. Terracol, E. Manoha, and P. Sagut. On the use of high order overlapping grid method for coupling in CFD/CAA. *Journal of Computational Physics*, 220:355–382, 2006.

[31] F. Dickstein, A.Q. Lara, C. Neri, and A.M. Peres. Modeling and simulation of horizontal wellbore-reservoir flow equations. In *Latin American and Caribbean Petroleum Engineering Conference, Rio de Janeiro, Brazil*, 30 August-3 September 1997. 39064-MS.

[32] D.Y. Ding. Near-well upscaling for reservoir simulations. *Oil & Gas Science and Technology - Rev. IFP*, 59:157–165, 2004.

[33] Y. Ding. Transient pressure solution in the presence of pressure drop in the wellbore. In *SPE Annual Technical Conference and Exhibition, Houston, Texas*, 3-6 October 1999.

[34] Y. Ding and L. Jeannin. A new methodology for singularity modelling in flow simulations in reservoir engineering. *Computational Geosciences*, 5(2):93–119, June 2001.

[35] Y. Ding and L. Jeannin. New numerical schemes for near-well modeling using flexible grids. *SPE Journal*, 9(1):109–121, 2004.

[36] Y. Ding and G. Renard. A new representation of wells in numerical reservoir simulation. *SPE Reservoir Engineering*, pages 140–144, May 1994.

[37] Y. Ding, G. Renard, and L. Weill. Representation of wells in numerical reservoir simulation. *SPE Reservoir Engineering*, pages 18–23, February 1998.

[38] Y. Ding, P.A. Lemonnier, T. Estebennet, and J-F. Magras. Control-volume method for simulation in the well vicinity for arbitrary well configurations. *SPE Journal*, 5(1):118–125, March 2000. SPE 62169.

[39] Y. Ding, T. Ha-Duong, J. Giroire, and V. Moumas. Modelling of single-phase flow for horizontal wells in a stratified medium. *Computers & Fluids*, 33:715–727, 2004.

[40] D.B. Duncan and Y. Qiu. Overlapping grids for the diffusion equation. *IMA Journal of Numerical Analysis*, 27:550–575, 2007.

[41] L.J. Durlofsky. An approximate model for well productivity in heterogeneous porous media. *Mathematical Geology*, 32(4):421–438, 2000.

[42] R.C. Jr. Earlougher. *Advances in Well Test Analysis*. Society of Petroleum Engineers, 1977.

[43] Jens P. Eberhard. Simulation of lognormal random fields with varying resolution scale and local average for Darcy flow. *Computing and Visualization in Science*, 9(1):1–10, 2006.

[44] M.J. Economides, C.W. Brand, and T.P. Frick. Well configurations in anisotropic reservoirs. *SPE Formation Evaluation*, pages 257–262, December 1996.

[45] T. Ertekin, J.H. Abou-Kassem, and G.R. King. *Basic Applied Reservoir Simulation*, volume 7 of *SPE Textbook Series*. Society of Petroleum Engineers Inc., 2001.

[46] L. Farina, Y. Ding, and T. Ha-Duong. Transient pressure solution for a horizontal well in a petroleum reservoir by boundary integral methods. *International Journal for Numerical Methods in Engineering*, 49:667–679, 2000.

[47] Peter A. Fokker and Francesca Verga. A semianalytic model for the productivity testing of multiple wells. *SPE Reservoir Evaluation & Engineering*, pages 466–477, June 2008. SPE 94153.

[48] Baris Göktas and Turgay Ertekin. Implementation of a local grid refinement technique in modeling slanted, undulating horizontal and multi-lateral wells. In *SPE Annual Technical Conference and Exhibition, Houston, Texas*, 3-6 October 1999.

[49] Reinaldo J. González-Requena and Juan M. Guevara-Jordan. New approach for describing transient pressure response generated by horizontal wells of arbitrary geometry. *Applied Numerical Mathematics*, 40:433–449, 2002.

[50] P.A. Goode and F.J. Kuchuk. Inflow performance of horizontal wells. *SPE Reservoir Engineering*, pages 319–323, August 1991.

[51] P.A. Goode and R.K.M Thambynayagam. Pressure drawdown and buildup analysis of horizontal wells in anisotropic media. *SPE Formation Evaluation*, pages 683–697, December 1987.

[52] A.C. Gringarten and H.J. Ramey. The use of source and Green's functions in solving unsteady-state problems in reservoirs. *SPE Journal*, pages 285–296, October 1973.

[53] A.C. Gringarten and H.J. Ramey. Unsteady-state pressure distributions created by a well with a single horizontal fracture, partial penetration or restricted entry. *SPE Journal*, pages 413–426, August 1974.

[54] A.C. Gringarten and H.J. Ramey. An approximate infinite conductivity solution for a partially penetrating line-source well. *SPE Journal*, pages 140–148, April 1975. SPE 4733.

[55] A.C. Gringarten, H.J. Ramey, and R. Raghavan. Applied pressure analysis for fractured wells. *Journal of Petroleum Technology*, pages 887–892, July 1975.

[56] P. Gui, L.B. Cunha, and J.C. Cunha. A numerical two-phase flow model coupling reservoir and multi-segment horizontal well. Presented at SPE Rocky Mountain Oil & Gas Technilogy Symposium, Denver, Colorado, USA, April 2007. SPE 107989.

[57] Hugh B. Hales. An improved method for simulating reservoir pressures through the incorporation of analytical well functions. Fifth Latin American and Carribean Petroleum Engineering Conference and Exhibition, Rio de Janerio, Brazil, 30 August - 3 September 1997. SPE 39065.

[58] Hassan Hassanzadeh and Mehran Pooladi-Darvish. Comparison of different numerical Laplace inversion methods for engineering applications. *Applied Mathematics and Computation*, 189:1966–1981, 2007.

[59] W.D. Henshaw and D.W. Schwendeman. An adaptive numercial scheme for high-speed reactive flow on overlapping grids. *Journal of Computational Physics*, 191: 420–227, 2003.

[60] William D. Henshaw. On multigrid for overlapping grids. *SIAM Journal on Scientific Computing*, 26(5):1547–1572, 2005.

[61] Roland N. Horne. *Modern Well Test Analysis: A Computer-Aided Approach.* Petroway Inc., 1995.

[62] W. Hundsdorfer and J.G. Verwer. *Numerical Solutions of Time-Dependent Advection-Diffusion-Reaction Equations.* Springer-Verlag, 2003.

[63] Peter Den Iseger. Numerical transform inversion using Gaussian quadrature. *Probability in the Engineering and Informational Sciences*, 20:1–44, 2006.

[64] J.K. Jasti, V.R. Penmatcha, and D.K. Babu. Use of analytic solutions to improve simulator accuracy. *SPE Journal*, 4(1):47–56, 1999.

[65] S. Krogstad and L.J. Durlofsky. Multiscale mixed-finite-element modeling of coupled wellbore/near-well flow. *SPE Journal*, Volume 14(1):78–87, 2009. SPE 106179-PA.

[66] B. Kurtoglu, F. Medeiros, E. Ozkan, and H. Kazemi. Semianalytical representation of wells and near-well flow convergence in numerical reservoir simulation. In *SPE Annual Technical Conference and Exhibition, Denver Colorado*, September 2008. SPE 116136.

[67] S.H. Lee and W.J. Milliken. The productivity index of an inclined well in finite-difference reservoir simulation. SPE Symposium on Reservoir Simulation, New Orleans, Louisiana, 28 February-3 March 1993.

[68] D. Leykekhman. Pointwise localized error estimates for parabolic finite element equations. *Numerische Mathematik*, 96(3):583–600, 2004.

[69] W. Liu, M.A. Hildebrand, J. Lee, and J. Sheng. High-resolution near-wellbore modeling and its application to formation testing. Presented at the SPE Annual Technical Conference and Exhibition, Houston, Texas, USA, September 2004. SPE 90767.

[70] MATLAB. The MathWorks, Inc, 3 Apple Hill Dr., Natick, MA 01760.

[71] F. Medeiros, E. Ozkan, and H. Kazemi. A semianalytical approach to model pressure transients in heterogeneous reservoirs. *SPE Reservoir Evaluation & Engineering*, 13(2):341–358, 2010.

[72] M. Muskat. *The Flow of Homogeneous Fluids Through Porous Media*. McGraw-Hill Book Co., 1937.

[73] B.O. Ogunsanya, T.P. Oetama, J.F. Lea, L.R. Heinze, and P.S. Adisoemarta. A coupled model for analyzing transient pressure behavior of horizontal drainholes. In *SPE Production Operations Symposium, Oklahoma City, Oklahoma*, 16-19 April 2005.

[74] F. Olsson and N.A. Petersson. Stability of interpolation on overlapping grids. *Computers and Fluids*, 25(6):583–606, 1996.

[75] Liang-Biao Ouyang and Khalid Aziz. A general single-phase wellbore/reservoir coupling model for multilateral wells. *SPE Reservoir Evaluation & Engineering*, pages 327–335, August 2001.

[76] E. Ozkan and R. Raghavan. New solutions for well-test-analysis problems: Part 1 – analytic considerations. *SPE Formation Evaluation*, pages 359–368, September 1991.

[77] E. Ozkan and R. Raghavan. New solutions for well-test-analysis problems: Part 2 – computational considerations and applications. *SPE Formation Evaluation*, pages 369–378, September 1991.

[78] E. Ozkan, R. Raghavan, and Sadanand D. Joshi. Horizontal-well pressure analysis. *SPE Formation Evaluation*, pages 567–575, December 1989.

[79] Erdal Ozkan, Cem Sarica, and Marc Haci. Influence of pressure drop along the wellbore on horizontal-well productivity. *SPE Journal*, 4(3):288–301, 1999.

[80] C.L. Palagi and K. Aziz. Modeling vertical and horizontal wells with Voronoi grid. *SPE Reservoir Engineering*, pages 15–21, February 1994.

[81] S.V. Parter. On the overlapping grid method for elliptic boundary value problems. *SIAM Journal on Numerical Analysis*, 36(3):819–852, 1999.

[82] D.W. Peaceman. Interpretation of well-block pressures in numerical reservoir simulation. *SPE Journal*, pages 183 – 194, June 1978. SPE 6893.

[83] D.W. Peaceman. Interpretation of well-block pressures in numerical reservoir simulation with nonsquare grid blocks and anisotropic permeability. *SPE Journal*, 23(3):531–543, 1983. SPE 10528.

[84] D.W. Peaceman. Interpretation of wellblock pressures in numerical reservoir simulation: Part 3 - off-center and multiple wells within a wellblock. *SPE Reservoir Engineering*, pages 227–232, May 1990.

[85] O.A. Pedrosa and K. Aziz. Use of a hybrid grid in reservoir simulation. *SPE Reservoir Engineering*, 1(6):611–621, November 1986.

[86] V.R. Penmatcha and K. Aziz. Comprehensive reservoir/wellbore model for horizontal wells. *SPE Journal*, 4(3):224–234, September 1999.

[87] A.J. Rosa and R Carvalho. A mathematical model for pressure evaluation in an infinite-conductivity horizontal well. *SPE Formation Evaluation*, 4(4):559–566, 1989.

[88] M.A. Sabet. *Well Test Analysis*. Gulf Publishing Company, 1991.

[89] A. H. Schatz and L. B. Wahlbin. Interior maximum norm estimates for finite element methods. *Mathematics of Computation*, 31(138):414–442, 1977.

[90] A. H. Schatz, V. Thomée, and L. B. Wahlbin. Stability, analyticity, and almost best approximation in maximum norm for parabolic finite element equations. *Communications on Pure and Applied Mathematics*, 51(11-12):1349–1385, 1998.

[91] L. F. Shampine and M. W. Reichelt. The MATLAB ODE Suite. *SIAM Journal on Scientific Computing*, 18(1):1–22, 1997.

[92] L.F. Shampine. Vectorized adaptive quadrature in MATLAB. *Journal of Computational and Applied Mathematics*, 211:131–140, 2008.

[93] Aaron Solo. Sharp estimates for finite element approximations to parabolic problems with Neumann boundary data of low regularity. *BIT Numerical Mathematics*, 48(1):117–137, 2008.

[94] René Sperb. *Maximum principles and their applications*, volume 157 of *Mathematics in Science and Engineering*. Academic Press, 1981.

[95] H. Stehfest. Algorithm 368: Numerical inversion of Laplace transforms. *Communications of the ACM*, 13:47–49, 1970.

[96] T.D. Streltsova. *Well Testing in Heterogeneous Formations*. John Wiley and Sons, 1998. An Exxon Monograph.

[97] Ho-Jeen Su. Modelling off-center wells in reservoir simulation. *SPE Reservoir Engineering*, pages 47–51, 1995. SPE25275.

[98] Koichi Suzuki. Influence of wellbore hydraulics on horizontal well pressure transient behavior. *SPE Formation Evaluation*, 12(3):175–181, 1997.

[99] Vidar Thomée. *Galerkin Finite Element Methods for Parabolic Problems*. Springer-Verlag, 1997.

[100] P.H. Valvante, L.J. Durlofsky, and K.Aziz. Semi-analytical modeling of the performance of intelligent well completions. In *SPE Reservoir Simulation Symposium, Houston, Texas*, 11-14 February 2001.

[101] H.K. van Poollen, E.A. Breitenback, and D.H. Thurnau. Treatment of individual wells and grids in reservoir modeling. *SPE Journal*, 8(4):341 – 346, 1968. SPE2022.

[102] R. Vicente, C. Sarica, and T Ertekin. A numerical model coupling reservoir and horizontal well-flow dynamics: Transient behaviour of single-phase liquid and gas flow. *SPE Journal*, pages 70–77, March 2002.

[103] R. Vicente, C. Sarica, and T. Ertekin. A numerical model coupling reservoir and horizontal well flow dynamics: applications in well completions, and production logging. *Journal of Energy Resources Technology*, 126:169–176, 2004.

[104] J. A. C. Weideman and L. N. Trefethen. Parabolic and hyperbolic contours for computing the Bromwich integral. *Mathematics of Computation*, 76(259):1341–1356, July 2007.

[105] C. Wolfsteiner and L.J. Durlofsky. Near-well radial upscaling for the accurate modelling of nonconventional wells. In *SPE Western Regional/AAPG Pacific Section Joint Meeting, Anchorage, Alaska, USA*, 20-22 May 2002. SPE 76779.

[106] C. Wolfsteiner, L.J. Durlofsky, and K. Aziz. Approximate model for productivity of nonconventional wells in heterogeneous reservoirs. *SPE Journal*, 5(2):218–226, June 2000.

[107] C. Wolfsteiner, L.J. Durlofsky, and K. Aziz. Calculation of well index for nonconventional wells on arbitrary grids. *Computational Geosciences*, 7:61–82, 2003.

[108] C. Wolfsteiner, S.H. Lee, and H.A. Tchelepi. Well modeling in the multiscale finite volume method for subsurface flow simulation. *Multiscale Modeling and Simulation*, 5(3):900–917, 2006.